Changes in the predictability of the North Atlantic ocean under global warming

Dissertation zur Erlangung des Doktorgrades

an der Fakultät für Mathematik, Informatik und

Naturwissenschaften

Fachbereich Geowissenschaften

der Universität Hamburg

vorgelegt von

Matthias Fischer

Hamburg, 2015

Tag der Disputation: 18.12.2015

Folgende Gutachter empfehlen die Annahme der Dissertation:

Prof. Dr. Johanna Baehr

Dr. Wolfgang A. Müller

Abstract

The North Atlantic Ocean plays an important role for the European and the North American climate. Hence, predictions of the North Atlantic climate on seasonal-to-decadal time scales are of growing interest. The North Atlantic Ocean is projected to change with global warming. Projections show an increase of surface temperatures and a reduction in the Atlantic meridional overturning circulation (AMOC) and the Atlantic meridional ocean heat transport (OHT). Yet, whether global warming affects the seasonal cycle and the decadal predictability of the AMOC and the OHT is still unknown. In this thesis I investigate changes in the AMOC and OHT seasonal cycle under global warming. In a second step, I focus on changes in potential predictability of the AMOC and the OHT that might result from potential changes in the seasonal cycle from the present climate state to a future climate state.

First, I investigate the effect of a projected reduction in the AMOC and in the OHT on their seasonal cycles. I analyze climate projection experiments performed with the Max-Planck Institute Earth System Model (MPI-ESM) for the Coupled Model Intercomparison Project phase 5 (CMIP5). My results suggest shifts in the AMOC and OHT seasonal cycles that predominantly result from changes in the wind-driven circulation. Analyzing long-term implications in the RCP8.5 (representative concentration pathway) scenario until the end of the 23rd century, I find a northward shift of 5 degrees and latitude dependent temporal shifts of 1 to 6 months in the seasonal cycle. Similar, but less intense changes are found until the middle of the 21st century in RCP4.5 and RCP8.5, in particular in the subtropical gyre (STG) around 25°N and in the subpolar gyre (SPG) around 50°N.

Second, I analyze changes in the potential predictability of the AMOC and OHT on inter-annual to decadal time scales under global warming. In MPI-ESM, I generate two hindcast ensembles for (i) the current climate state in the CMIP5 historical simulation starting in 1995 and extended with RCP4.5 after 2005 (HIST_{ens}) and (ii) a future climate state in RCP4.5 starting in 2045 (RCP_{ens}). Changes in the potential predictability are assessed by means of the anomaly correlation coefficient (ACC), the reliability and the Brier Skill Score (BSS) of the hindcasts for multiyear means and multiyear seasonal means.

The potential predictability of the AMOC and the OHT changes predominantly at latitudes where considerable changes are found in the seasonal cycle. For the AMOC in HIST_{ens}, the STG reveals longer predictable lead times compared to the SPG resulting predominately from the predictability of the geostrophic transport and the predictability of multiyear summer means. The ACC of the AMOC is reduced from HIST_{ens} to RCP_{ens} in the STG and the SPG, as is the reliability. In RCP_{ens}, the reduction in the predictability of the AMOC results predominately from a reduced predictability of summer means.

For the OHT in HIST_{ens}, the SPG reveals longer predictable lead times compared to the STG. Between HIST_{ens} and RCP_{ens}, the ACC is reduced in the STG and increased in the SPG with longer predictable lead times in the SPG compared to HIST_{ens}. The reliability and the BSS are reduced in the STG and SPG between HIST_{ens} and RCP_{ens}, even though winter and summer show reliable predictions in the SPG. The reduction in the predictability of the OHT results from changes in all seasons.

The results of this thesis further highlight that changes in the seasonal cycle, in connection with an overall decrease in the variance of yearly means, lead to a reduction in the potential predictability under global warming, while an increased variance leads to an increased potential predictability.

Zusammenfassung

Der Nordatlantische Ozean ist für das Klima in Europa und Nordamerika von großer Bedeutung. Daher sind Vorhersagen des nordatlantischen Klimas auf saisonalen bis dekadischen Zeitskalen von besonderem Interesse. Klimaprojektionen zeigen Veränderungen des Nordatlantiks im Zuge der globalen Erwärmung. Diese beinhalten einen Anstieg der Oberflächentemperaturen, eine Abnahme der Atlantischen meridionalen Umwältzzirkulation (AMOC) sowie eine Abnahme des meridionalen ozeanischen Wärmetransportes (OHT). Bisher ist nicht untersucht, ob die globale Erwärmung den Jahresgang und die dekadische Vorhersagbarkeit der AMOC und des OHT beeinflusst. In dieser Arbeit untersuche ich Veränderungen im Jahresgang der AMOC und des OHT unter Einfluss des Klimawandels. In einem weiteren Schritt untersuche ich Veränderungen der potentiellen Vorhersagbarkeit der AMOC und des OHT. Diese können aus potentiellen Veränderungen des Jahresgangs von dem derzeitigen Klimazustand zu einem zukünftigen Klimazustand resultieren.

In einem ersten Schritt analysiere ich Jahresgangsänderungen der AMOC und des OHT unter Einfluss des Klimawandels. Dazu werden Klimaprojektionen herangezogen, die im gekoppelten Max-Planck-Erdsystemmodell (MPI-ESM) im Rahmen des Coupled Model Intercomparisson Project phase 5 (CMIP5) durchgeführt wurden. Meine Ergebnisse zeigen Verschiebungen im Jahresgang der AMOC und des OHT, die in erster Linie aus Änderungen der windgetriebenen Zirkulation resultieren. Änderungen bis Ende des 23. Jahrhunderts im Klimaänderungsszenario RCP8.5 (RCP=representative concentration pathway) zeigen eine Nordwärtsverschiebung um 5° und breitenabhängige zeitliche Verschiebungen von 1 bis 6 Monaten im Jahresgang sowie Änderungen in der Jahreszeitenamplitude. Ähnliche, wenn auch schwächere Änderungen, treten bis zur Mitte des 21. Jahrhunderts in RCP4.5 und RCP8.5 auf. Diese zeigen sich besonders im Subtropenwirbel (STG) um 25°N und im Subpolarwirbel (SPG) um 50°N.

Anschließend werden Veränderungen der potentiellen Vorhersagbarkeit der AMOC und des OHT unter Einfluss der globalen Erwärmung auf interannualen bis dekadischen Zeitskalen untersucht. Dazu werden zwei Ensemble-Vorhersage-Experimente (*Hindcasts*) in MPI-ESM erstellt: zum einen für den derzeitigen Klimazustand im CMIP5 historischen Lauf, der mit dem RCP4.5 Szenario erweitert wird (HIST_{ens}), und zum anderen für einen zukünftigen Klimazustand in RCP4.5 (RCP_{ens}). Veränderungen der Vorhersagbarkeit werden mit Hilfe des Anomaliekorrelationskoeffizienten (ACC), der *reliability* und des Brier Skill Scores (BSS) der Hindcasts für Jahresmittel und saisonale Mittel untersucht.

Die potentielle Vorhersagbarkeit der AMOC und des OHT ändert sich besonders an Breitengraden mit großen Änderungen im Jahresgang. Die AMOC zeigt in HIST_{ens} eine längere Vorhersagbarkeitszeit (*predictable lead times*) im STG als im SPG. Dies ist bedingt durch die Vorhersagbarkeit des geostrophischen Transportes und der Vorhersagbarkeit von Sommermitteln. Vom derzeitigen Zustand in HIST_{ens} zu RCP_{ens} verringert sich der ACC – und gleichzeitig die *reliability* – der AMOC im STG und SPG. Die verringerte Vorhersagbarkeit in RCP_{ens} resultiert hauptsächlich aus der verringerten Vorhersagbarkeit der Sommermittelwerte.

Im OHT zeigt der SPG für den derzeitigen Klimazustand in HIST_{ens} längere Vorhersagbarkeit im Vergleich zum STG. Von HIST_{ens} hinzu RCP_{ens} ist der ACC im STG verringert und im SPG erhöht. Der OHT zeigt längere Vorhersagezeiten im SPG im Vergleich zu HIST_{ens}. Die *reliability* und der BSS sind im STG und SPG verringert von HIST_{ens} zu RCP_{ens}. Sommer- und Wintermittel zeigen jedoch eine gewisse *reliability* der Vorhersagen im SPG. Die generelle Verringerung der Vorhersagbarkeit des OHT resultiert aus Änderungen in allen Jahreszeiten.
Die Ergebnisse dieser Arbeit heben außerdem hervor, dass Änderungen im Jahresgang, zusammen mit einer generellen Verringerung der Varianz von Jahresmitteln, die potentielle Vorhersagbarkeit unter Einfluss der globalen Erwärmung verringern, wobei eine verstärkte Varianz die potentielle Vorhersagbarkeit erhöht.

Contents

1 Introduction

1.1 Motivation

1.1.1 Global warming and the North Atlantic ocean circulation

The North Atlantic Ocean has received increased attention in recent years due to its key role for the regional and the global climate. The North Atlantic Ocean is shown to impact local climate phenomena such as Atlantic hurricanes or Sahel drought (e.g., Knight et al., 2006, Zhang and Delworth, 2006), the North American and European climate (e.g., Sutton and Hodson, 2005, Pohlmann et al., 2006, Sutton and Dong, 2012) or climate phenomena with global impacts, such as the North Atlantic Oscillation (NAO; e.g., Czaja et al., 1999, Czaja and Frankignoul, 2002, Frankignoul et al., 2013, Gastineau and Frankignoul, 2015). Climate model simulations suggest that fluctuations in the Atlantic meridional overturning circulation (AMOC) are linked to decadal climate variability in the North Atlantic sector (e.g. Latif and Keenlyside, 2011, Siedler et al., 2013) with important socio-economic impacts (e.g. Srokosz et al., 2012, Smeed et al., 2013).
Via the Atlantic Multidecadal Oscillation (AMO), a number of these climate phenomena has been linked to the variability of North Atlantic sea surface temperatures (SST; e.g., Delworth and Greatbatch, 2000, Knight et al., 2005, Msadek and Frankignoul, 2009, Zhang and Wang, 2013). In particular the AMOC and the associated Atlantic meridional ocean heat transport (OHT)

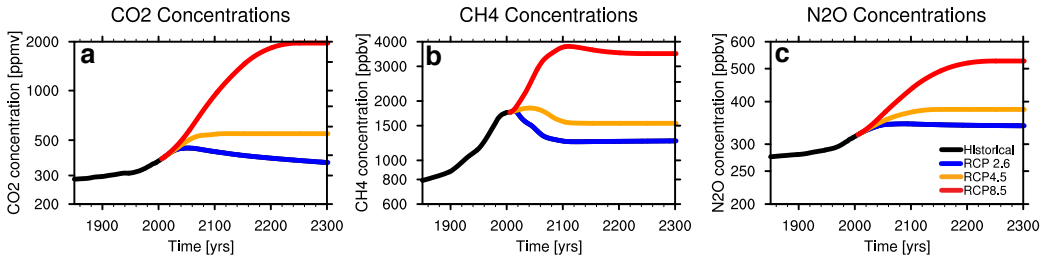

Figure 1.1: Greenhouse gas concentration of CO_2 (**a**), CH_4 (**b**) and N_2O (**c**) for the historical period until 2005 (black) and the RCP scenarios RCP2.6 (blue), RCP4.5 (yellow) and RCP8.5 (red) from 2006 to 2300. The concentrations on the vertical axis are shown with a logarithmic scale.

has been shown to affect the North Atlantic SSTs and the North Atlantic heat content (e.g., Dong and Sutton, 2003, Grist et al., 2010, Muir and Fedorov, 2014) and thus the AMO. However, the distinct role of the North Atlantic Ocean on the climate of the North Atlantic sector is still controversially discussed (e.g., Riser and Lozier, 2013, and references therein) and the influence of the AMOC and OHT on specific seasons has not yet been identified.

Recently, the continuous observations of the AMOC and the OHT at the 26°N Rapid array and at 41°N have indicated long-term variability and a seasonal cycle of the AMOC and the OHT in the North Atlantic (Kanzow et al., 2010, Johns et al., 2011, Willis, 2010, Hobbs and Willis, 2012). Nevertheless, Atlantic-wide continuous observations are still unavailable and most of the present understanding on the seasonal cycle of the AMOC and OHT was gained from model experiments (e.g., Lee and Marotzke, 1998, Jayne and Marotzke, 2001, Cabanes et al., 2008, Munoz et al., 2011). Studies relating the seasonal cycle of the AMOC and the OHT to the atmosphere are still lacking. Therefore, a better understanding of the variability and seasonal cycle of the AMOC and the OHT is important to address the specific role of the AMOC and the OHT for the European climate, as well as for the understanding and predictions of the North Atlantic climate variability.

The strength of the AMOC and the OHT can fluctuate through the natural internal variability of the climate system. Both the AMOC and OHT are expected to decline due to global warming (e.g., IPCC, 2013). Global climate change simulations project a global warming of the climate system driven by

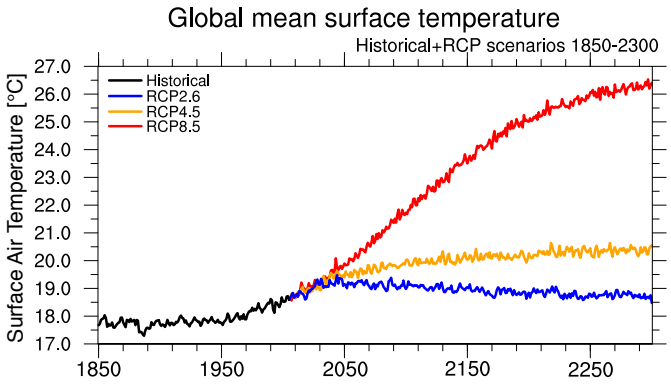

Figure 1.2: Global mean surface air temperatures [°C] in MPI-ESM-LR for the historical period until 2005 (black) and the RCP scenarios RCP2.6 (blue), RCP4.5 (yellow) and RCP8.5 (red) from 2006 to 2300.

an increase of the total concentration of greenhouse gases, as shown in the recently published fifth assessment report (AR5) of the Intergovernmental Panel on Climate Change (IPCC, 2013). Since the preindustrial period, the atmospheric concentration of CO_2 raised from about 280 ppmv to almost 400 ppmv in today's climate state (Fig. 1.1; IPCC, 2013). Associated with the increase in greenhouse gases, global mean temperatures have increased by about 1°C from the 19th century until today (IPCC, 2013).

In context of the Coupled Model Intercomparison Project Phase 5 (CMIP5, Taylor et al., 2012) a coordinated set of global climate projections is performed as part of the IPCC AR5. For the climate projection experiments, a set of climate change scenarios, called representative concentration pathways (RCP), have been developed that imply different adaptation and mitigation strategies to climate change and thus a different evolution of greenhouse gases concentrations (Taylor et al., 2012). The scenarios include a high emission scenario RCP8.5, two intermediate scenarios RCP6 and RCP4.5 and a decay scenario RCP2.6 peaking in the middle of the twenty-first century and extend the historical simulation that represents the climate state of the 19th and 20th century. The CO_2 concentrations for the individual scenarios are shown in Fig.1.1a with a high increase in RCP8.5, an intermediate increase in RCP4.5 and a peaking of CO_2 concentrations in RCP2.6 (Fig.1.1a). Similar to the CO_2 concentrations, the concentrations of other greenhouse gases such as CH_4 and N_2O develop over the next centuries (Fig.1.1b,c).

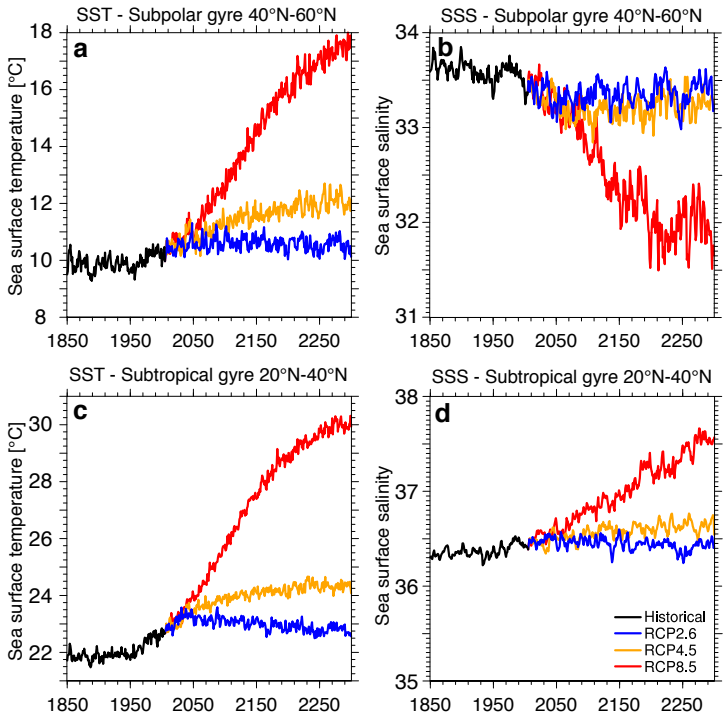

Figure 1.3: Sea surface temperatures (°C, **a**&**c**) and sea surface salinities (g/kg, **b**&**d**) in the subpolar gyre (**a**-**b**) and the subtropical gyre (**c**-**d**) for the historical period until 2005 (black) and the RCP scenarios RCP2.6 (blue), RCP4.5 (yellow) and RCP8.5 (red) from 2006 to 2300.

Following the individual scenarios, global mean surface temperatures are projected to increase between about 1°C and about 4°C from the present climate state until the year 2100 in the CMIP5 multimodel ensemble (IPCC, 2013), as shown for the Max-Planck-Institute Earth System Model (MPI-ESM, Fig.1.2). MPI-ESM simulations project a warming between about 1.5°C in RCP2.6 and about 4°C in RCP8.5 until 2100, and between 1°C in RCP2.6 and about 8°C in RCP8.5 until 2300.

In concert with the projected increase of global surface temperatures, the CMIP5 multi-model ensemble and similarly MPI-ESM project an increase of sea surface temperatures over the North Atlantic in both the subtropical and subpolar gyre (Fig.1.3; IPCC, 2013). The increase in the SSTs is approximately in the range of the increase in the global mean surface temperatures in RCP2.6 to RCP8.5 in MPI-ESM (Fig.1.3). In contrast to the SSTs, sea surface salinities are projected to increase in the tropical and subtropi-

cal North Atlantic, but to decrease in the subpolar North Atlantic (Fig.1.3; IPCC, 2013). The freshening and warming of the subpolar North Atlantic increase the buoyancy forcing and result in a reduction of convection and deep water formation in the North Atlantic that is found to weaken the AMOC (e.g., Gregory et al., 2005, Gregory and Tailleux, 2011, Weaver et al., 2012) and accordingly to reduce the OHT.
Together with global warming, changes in the amplitude and phase of the seasonal cycle of surface air temperatures (Dwyer et al., 2012) and accordingly sea surface temperatures and sea surface salinities in the Arctic ocean (Carton et al., 2015) are identified in climate projections. However, changes in the seasonal cycle of the AMOC and the OHT due to global warming which might impact the North Atlantic climate have not been investigated to my knowledge.

1.1.2 Decadal predictability

The fundamental role of the AMOC and OHT for the North Atlantic climate and its variability (e.g., Sutton and Hodson, 2005, Knight et al., 2005, Pohlmann et al., 2006) motivates to advance the understanding of the North Atlantic climate predictability.
Decadal predictions are still in an early stage (Goddard et al., 2013), even though a lot of progress and success was achieved in context of the recent coordinated effort of CMIP5 (Taylor et al., 2012, Meehl et al., 2014). In CMIP5, decadal climate predictions have been investigated in a multi-model framework based on retrospective ensemble forecast experiments, so-called ensemble hindcast experiments (Meehl et al., 2009). Studies in the context of CMIP5 mostly focussed on the analysis of the predictability under historical climate conditions that represent the climate state of the last half century from 1960 to 2005. But studies invoking the impact of future climate change on decadal predictability – in particular of the AMOC and the OHT – do not exist to my knowledge apart from Boer (2009) who finds that the potential (decadal) predictability of surface temperatures and precipitation is potentially decreased under global warming and Tietsche et al. (2013) who find a

a reduction in skill of Arctic sea ice predictions in the 21st century.

Following the work of Edward N. Lorenz, climate predictions can be classified into short-term (seasonal to inter-annual) forecasts and into long-term climate projections over a few centuries (Lorenz, 1975). The former rely on the knowledge of initial conditions which is never perfect. By errors in the initial conditions, the forecast diverges from the true state of the system with increasing lead time (initial value problem). The latter rely on the knowledge of the external forcing, as for climate projections, and the exact initial conditions become of second order (boundary value problem). Decadal climate predictions range in between short-term forecasts and long-term climate projections with timescale of some years to several decades. Therefore, decadal predictions rely on both, a good knowledge of the initial conditions for lead times of a few years and the good knowledge of the external forcing for lead times in the order of one decade or more and thus can be seen as a joint initial and boundary value problem (e.g., Collins and Allen, 2002, Collins, 2002, Collins et al., 2006, Goddard et al., 2012). In contrast to numerical weather prediction that aims to forecast most precisely individual weather events, decadal climate prediction aims to provide information about the future evolution of the statistics of mostly regional climate (e.g., Meehl et al., 2014).

In the early stage of decadal predictions, studies were performed in so-called "perfect model" experiments that compare the model hindcast against a control simulation in that model. Since continuous observations in the ocean, especially of integrated quantities like the AMOC and the OHT, are sparse, the validation of the prediction against a control simulation plays a crucial role for the understanding of decadal predictability. These early studies found predictability especially over the North Atlantic Ocean (Griffies and Bryan, 1997, Pohlmann et al., 2004, Collins et al., 2006). Accordingly, more recent predictability studies found the North Atlantic Ocean as a key region for decadal predictions with distinct skill in predicting air and sea surface temperatures (Pohlmann et al., 2009, van Oldenborgh et al., 2012, Matei et al., 2012b, Pohlmann et al., 2013a), the North Atlantic heat content (Yeager

et al., 2012, Kröger et al., 2012), the North Atlantic subpolar gyre (Matei et al., 2012b, Yeager et al., 2012, Robson et al., 2012) or the Atlantic meridional overturning circulation (Collins et al., 2006, Msadek et al., 2010, Matei et al., 2012a, Pohlmann et al., 2013b).

Predictability is commonly estimated either from prognostic (classical) predictability or from potential (diagnostic) predictability (Latif et al., 2006). Prognostic predictability is usually assessed from ensemble experiments by perturbing the initial state and is often compared to the "perfect model" (e.g., Griffies and Bryan, 1997, Collins, 2002, Pohlmann et al., 2006). Prognostic predictability provides an upper limit of predictability in the model. Diagnostic predictability is commonly estimated from the variance of the long-term variability against internally generated variability which is not predictable (e.g., Boer, 2004). The decadal predictability is usually estimated from one or more of the following measures: The anomaly correlation coefficent (ACC; e.g., Collins, 2002) between the ensemble mean and the control simulation, the prognostic potential predictability (e.g., Collins and Allen, 2002) that compares the ensemble spread to the variance of the control simulation or the root-mean-square error (e.g., Collins, 2002) showing deviations of the ensemble hindcast from the control simulation. Recently, decadal predictability has been estimated from reliability diagrams and the Brier Skill Score that is routinely used in weather prediction and seasonal prediction (Corti et al., 2012).

Studies on predictability of the AMOC have mostly focussed on one single latitude. Recent studies analyzing the latitude-dependent predictability showed, that the AMOC is potentially predictable with longer lead times in the subtropical gyre than in the subpolar gyre (Tiedje et al., 2012, Bellucci et al., 2013), while the predictability of the OHT tends to be longer in the subpolar North Atlantic (Tiedje et al., 2012). Studies linking the predictability of the AMOC and OHT are sparse (Tiedje and Baehr, 2014). The majority of studies focussed on yearly means for the analysis of the predictability. Nevertheless, the predictability might vary between different seasons, as the parameters as well as the underlying mechanisms change

seasonally in space and time. Müller et al. (2012) analyzed the predictive skill of surface air temperature and found skill for winter means over northern Europe, and skill of summer to autumn means over central and south-eastern Europe. MacLeod et al. (2012) showed that the skill of yearly means is higher than the skill of seasonal means over the North Atlantic. However, the skill of multiyear seasonal means has not been examined for the AMOC and the OHT. Further, potential changes in the variability and the seasonal cycle of the AMOC and the OHT might influence the predictability of the AMOC and OHT for yearly means and multiyear seasonal means.

1.2 Objectives of the thesis

This study aims to investigate the effect of potential changes in the global climate system on the North Atlantic ocean circulation and on the potential predictability for multiyear means and multiyear seasonal means of the AMOC and the OHT from the present climate state to a projected future climate state. To my knowledge, no study exists that investigates whether the predictability of the AMOC and OHT is influenced by global warming in a future climate state.

As a first step, changes in the North Atlantic ocean circulation are analyzed in MPI-ESM CMIP5 climate projections. I focus in particular on changes in the AMOC and the OHT and their seasonal cycles between a present climate state in the CMIP5 historical simulation and a future climate state in RCP4.5 and RCP8.5. Specifically, I analyze the following questions:

- What changes do emerge in the mean state of the North Atlantic ocean circulation, the AMOC and the OHT due to global warming in the MPI-ESM climate projections?

- Do projected changes in the mean state of the North Atlantic ocean circulation imply changes in the seasonal cycle of the OHT until the end of the 23rd century in the MPI-ESM climate projections?
- Are changes in the seasonal cycle already noticeable in the near future in the middle of the 21st century?

In a second step, I investigate the influence of climate change on potential predictability of the AMOC and the OHT. The predictability is investigated in two comparable retrospective ensemble (hindcast) experiments in MPI-ESM based on the CMIP5 historical simulation and RCP4.5. The hindcast experiments are referenced against the CMIP5 historical simulation and RCP4.5, respectively, so that the analysis is limited to the "perfect model world". In the predictability analysis I focus on the following questions:

- Does the potential predictability of the AMOC and the OHT change between the present climate state and a projected future climate state?
- If so, is there an impact of changes in the seasonal cycle on the potential predictability of the AMOC and OHT and do specific latitudes show more prominent changes than others?
- Do changes in the seasonal cycle project onto the potential predictability of multiyear seasonal means of the AMOC and the OHT?

1.3 Outline of the thesis

This thesis investigates changes in the mean state and seasonal cycle of the AMOC and the OHT and subsequently changes in the potential predictability of the AMOC and OHT under global warming.

Chapter 2 analyses mean changes in the North Atlantic ocean circulation and changes in the seasonal cycle of the OHT under global warming with a focus

on the RCP8.5 scenario in MPI-ESM for long-term changes until the end of the 23rd century. Section 2.1 is written in paper form and is submitted to Journal of Climate.[1] This chapter focusses on the mechanisms that drive changes in the OHT and its seasonal cycle in the climate projection. Section 2.2 provides an analysis of the OHT seasonal cycle based on a heat function in potential temperature coordinates.

Chapter 3 investigates changes in the AMOC and OHT seasonal cycle until the middle of the 21st century. As a prerequisite for the potential predictability analysis, I identify latitudes with considerable changes in the seasonal cycle that might imply considerable changes in the potential predictability of AMOC and the OHT.

Chapter 4 investigates whether global climate change impacts the potential predictability of the AMOC and the OHT from a present climate state represented by the CMIP5 historical simulation to a future climate state in RCP4.5 in the middle of the 21st century.

Chapter 5 gives an overall summary of the results and conclusions of the thesis.

[1] This section is submitted to Journal of Climate as *Fischer et al. (2015): The Atlantic meridional heat transport seasonal cycle in a MPI-ESM climate projection.*

2 Long-term changes in the Atlantic meridional heat transport and its seasonal cycle

2.1 The Atlantic meridional heat transport seasonal cycle in a MPI-ESM climate projection[1]

Abstract

We investigate the effect of a projected reduction in the Atlantic Ocean meridional heat transport (OHT) on changes in its seasonal cycle. We analyze a climate projection experiment with the Max-Planck Institute Earth System Model (MPI-ESM) performed for the Coupled Model Intercomparison Project phase 5 (CMIP5). In the RCP8.5 climate change scenario, the oceanic OHT declines in MPI-ESM in the North Atlantic by 30-50% by the end of the 23rd century. The decline in the OHT is accompanied by a change in the seasonal cycle of the total OHT and its components. We decompose the OHT into overturning and gyre component, and analyze changes in the vertical structure

[1]This section is submitted to Journal of Climate as *Fischer et al. (2015): The Atlantic meridional heat transport seasonal cycle in a MPI-ESM climate projection.*

of the OHT seasonal cycle in individual water masses. For the total OHT seasonal cycle, we find a northward shift of 5 degrees and latitude dependent temporal shifts of 1 to 6 months that are mainly associated with changes in the meridional velocity field. We find that the shift in the OHT seasonal cycle predominantly results from changes in the wind-driven surface and intermediate circulation which project onto the overturning component of the OHT in the tropical and subtropical North Atlantic. This leads to latitude dependent shifts of 1 to 6 months in the overturning component. In the subpolar North Atlantic, we find that the reduction of the North Atlantic Deep Water formation in RCP8.5 results in a strongly weakened seasonal cycle in North Atlantic Deep Water with an almost absent seasonal amplitude by the end of the 23rd century.

2.1.1 Introduction

Global surface temperatures are projected to warm - depending on the considered climate change scenario - intensively over the next centuries (IPCC, 2013) accompanied by a projected shift in the amplitude and phase of the seasonal cycle of surface air temperatures (Dwyer et al., 2012). In concert, the Atlantic meridional overturning circulation (AMOC) is projected to slow down (Weaver et al., 2012, IPCC, 2013) and thus the associated Atlantic Ocean meridional heat transport (OHT) due to their direct linear relation found in observations and model studies (Johns et al., 2011, Msadek et al., 2013). However, it is unclear how climate change along with a projected shift in the seasonal cycle of surface temperatures affects the seasonal cycle of the ocean circulation, and especially of the OHT. Here, we investigate projected changes in the OHT seasonal cycle in a Coupled Model Intercomparison Project phase 5 (CMIP5) climate projection (Taylor et al., 2012) performed in the global coupled Max-Planck Institute Earth System Model (MPI-ESM) .

In the CMIP5 Representative Concentration Pathway (RCP) RCP8.5, surface air temperatures are expected to increase by about 8 degrees in the global

mean until the year 2300 in the CMIP5 multi-model ensemble (IPCC, 2013). The warming manifests itself over the continents and in particular in polar regions where an increase in surface temperatures of more than 20°C arises in climate projections until 2300 (e.g., IPCC, 2013, Bintanja and Van der Linden, 2013). Due to the strong warming in polar latitudes the meridional temperature gradient from the equator to the poles is also strongly reduced in the Northern Hemisphere. The atmospheric circulation patterns are projected to move poleward in concert with the warming of surface temperature, leading to a poleward expansion of the tropical cell and a poleward shift of the jet stream and storm track (Chang et al., 2012, Hu et al., 2013, IPCC, 2013). In contrast to the general warming, the surface air temperatures show a prominent area of reduced warming over the North Atlantic subpolar gyre (SPG) in the set of CMIP5 climate projections associated with an adjustment of the Atlantic meridional overturning circulation (AMOC) (Drijfhout et al., 2012) or a reduction of the OHT into the SPG (Rahmstorf et al., 2015). These changes in the surface temperature patterns thus suggest considerable changes in the North Atlantic ocean circulation, the AMOC and the associated OHT.

The implications of the Atlantic ocean circulation and the OHT for the North Atlantic sector and the European climate have been widely discussed. The AMOC and OHT in the North Atlantic has been shown to affect the North Atlantic heat content and the North Atlantic sea surface temperatures (SST; e.g., Dong and Sutton, 2003, Grist et al., 2010, Sonnewald et al., 2013, Muir and Fedorov, 2014). Changes in the North Atlantic SSTs and the air-sea interaction appear to be important for influencing the atmospheric circulation, the multidecadal variability of the North Atlantic sector an the North American and European climate on inter-annual to multi-decadal time scales (Rodwell et al., 2004, Sutton and Hodson, 2005, Gastineau and Frankignoul, 2015).

Further, a response of the NAO to North Atlantic sea surface temperatures has been found both in observations and model studies (Czaja et al., 1999, Czaja and Frankignoul, 2002, Rodwell and Folland, 2002, Frankignoul et al., 2013, Gastineau et al., 2013, Gastineau and Frankignoul, 2015). Via the Atlantic Multidecadal Oscillation (AMO), which is thought to result from

AMOC and OHT variability (e.g., Delworth and Greatbatch, 2000, Knight et al., 2005, Msadek and Frankignoul, 2009, Zhang and Wang, 2013), the SST variability has been linked to a number of climate phenomena, such as Sahel rainfall, Atlantic hurricane activity and North American and European summer climate (Enfield et al., 2001, Sutton and Hodson, 2005, Knight et al., 2006, Zhang and Delworth, 2006, Sutton and Dong, 2012). However, the specific role and direct importance of the OHT for European climate is still controversially discussed and the exact mechanism not fully understood (Bryden, 1993, Seager et al., 2002, Rhines et al., 2008, Riser and Lozier, 2013).
For the seasonal variability, the coupling between ocean and atmosphere is less understood. Minobe et al. (2010) have shown an atmospheric response to Gulf stream variability with seasonal variations. When considering also the impact of seasonal variations in the total OHT on European climate, the relation becomes even more complex and thus requires a better understanding of the OHT and its coupling to the atmosphere.
Yet, most of the present understanding stems from model analysis, due to a lack of continuous observations. Most traditional observations of the OHT are based on hydrographic snapshots (e.g., Bryan, 1962, Hall and Bryden, 1982, Lavin et al., 1998, Lumpkin and Speer, 2007) or inverse methods (e.g., Macdonald and Wunsch, 1996, Ganachaud and Wunsch, 2000, 2003) and give estimates of the time mean OHT of about 1 PW, but do not describe the OHT variability. Further, single hydrographic snapshots may be affected by a seasonal bias due to the predominance of field work during summer. Recently, the two time series of the 26°N Rapid array and observations at 41°N have indicated long-term variability and a clear seasonal cycle of the OHT in the North Atlantic (Johns et al., 2011, Hobbs and Willis, 2012).
A better understanding of the dynamics of the seasonal cycle of the OHT has been gained from a number of model studies. The pioneering study by Bryan (1982b) used a global ocean circulation model forced with observed winds. Bryan pointed out the importance of the wind-driven Ekman mass transport and of the associated Ekman heat transport for driving the seasonal variability of the OHT, which was also found in subsequent studies (Sarmiento, 1986, Lee and Marotzke, 1998, Jayne and Marotzke, 2001, Böning et al., 2001, Cabanes et al., 2008, Balan Sarojini et al., 2011, Munoz et al., 2011).

Bryan argued that changes in the zonally integrated wind stress, leading to changes in the Ekman mass transport, are balanced by a barotropic return flow. Jayne and Marotzke (2001) provided the theoretical and dynamical justification for Bryan's argumentation, stressing again the important role of the Ekman transport for the seasonal cycle of the OHT.

Traditionally, the OHT is decomposed into a vertical overturning component, which is commonly linked to the large scale overturning, and a horizontal gyre component giving correlations of the zonal deviations of the velocity and temperature field (Bryan, 1962, 1982a, Bryden and Imawaki, 2001, Siedler et al., 2013). The gyre component is commonly linked to the horizontal gyre circulation and contributions from the eddy field. Previous studies have shown that the overturning component dominates the time mean, as well as the interdecadal variability of the OHT in the tropical and subtropical North Atlantic, whereas the overturning and gyre component contribute about equally to the OHT and its interdecadal variability in the subpolar North Atlantic (e.g., Eden and Jung, 2001). But this decomposition does not reveal the vertical structure of the OHT and contributions from individual water masses. Hence, recent studies have attempted to determine the vertical pathways of the OHT in observations and model studies. Talley (2003) has analyzed the vertical pathways of the OHT in observations. She found that 60% of the mean OHT at 24°N in the North Atlantic results from the intermediate and deep overturning, while the remaining 40% are carried northward in a shallow overturning layer, in contrast to the traditional view, where about 90% of the heat transport are ascribed to the deep overturning circulation (e.g. Bryden and Imawaki, 2001).

Boccaletti et al. (2005) and Ferrari and Ferreira (2011) analyzed the vertical structure of the heat transport based on a heat function in depth and temperature coordinates. Boccaletti et al. (2005) touched the problem of recirculation cells that complicate the calculation of the heat function in depth coordinates. Ferrari and Ferreira (2011) circumvented the problem of recirculation cells by calculating the heat function in temperature coordinates. They showed that the OHT is surface intensified and follows from a combined circulation of cold and warm water masses, so that most of the heat transport cannot be assigned to shallow or deep circulations only. However,

the impact of changes in the vertical structure of the OHT on its seasonal cycle is still unclear.

With this study, we aim to understand how the Atlantic Ocean meridional heat transport seasonal cycle is affected by global warming and what determines potential changes in the OHT seasonal cycle. For our analysis, we use a CMIP5 climate change projection performed in MPI-ESM, with a focus on the climate change scenario RCP8.5 with the strongest climate change forcing involved. We aim to identify changes in the seasonal cycle of Atlantic meridional heat transport and its sources including changes in the circulation of the surface and upper ocean and changes in the deep circulation. Second, to analyze different physical mechanisms that contribute to the changes in the seasonal cycle, we look at the individual contributions to the total OHT on seasonal time scales. Therefore, we first decompose the OHT into gyre- and overturning component, related to the horizontal gyre circulation and to the overturning circulation in the North Atlantic and consider changes in the wind-driven Ekman heat transport. To analyze the vertical structure of the OHT and the relative contributions of various depths to the seasonal cycle, we investigate the vertical structure of OHT in density coordinates.

This study is structured as follows: first, we describe the analyzed CMIP5 experiments performed in the coupled climate model MPI-ESM and the Atlantic meridional heat transport and its decomposition (section 2.1.2). Section 2.1.3 presents mean changes in the AMOC and of the OHT in the climate projection under global warming and the main characteristics of the OHT and its components in MPI-ESM. In section 2.1.4 we analyze the changes in the seasonal cycle of the OHT and its components in the MPI-ESM climate projections for long-term changes by the end of the 23rd century. A discussion and conclusions are given in sections 2.1.5 and 2.1.6.

2.1.2 Model and Methods

2.1.2.1 The CMIP5 climate change scenario RCP8.5 in MPI-ESM

We analyze one member of the CMIP5 ensemble (Taylor et al., 2012) performed in the coupled Max-Planck-Institute Earth System model in low resolution configuration (MPI-ESM-LR) that is integrated from 1850 to 2300. In the ocean component MPIOM (Marsland et al., 2003, Jungclaus et al., 2013), the horizontal resolution is 1.5 degree on average with 40 unevenly spaced vertical levels. The atmospheric component ECHAM6 (Stevens et al., 2013) has a horizontal resolution of T63 and includes 47 vertical levels.
We focus on one member the CMIP5 ensemble in the historical simulation (1850-2005) and extend the historical simulation with the Representative Concentration Pathway (RCP) RCP8.5 from 2006 to 2300. In RCP8.5, a rising radiative forcing following "business as usual" is applied, which rises to $8.5 W/m^2$ in the year 2100, and further increases after that (van Vuuren et al., 2011). We focus on longterm changes in RCP8.5, comparing the period 1850-1950 for the historical simulation (HIST_{mean}) to the period 2200-2300 for the RCP8.5 scenario (RCP_{mean}), where we expect the strongest changes in the North Atlantic ocean circulation and in the seasonal cycle of the OHT.

Projected changes in the North Atlantic sea surface temperatures
In concert with the projected warming of surface air temperatures, the sea surface temperatures (SST) are projected to warm globally and also in the North Atlantic sector in RCP8.5 (Fig.2.1). A similar "warming hole" signature as found for surface air temperatures (c.f., Drijfhout et al., 2012) is present in the North Atlantic SSTs (Fig.2.1) with a stronger warming in polar regions and an area of reduced warming in the SPG (Fig.2.1c). Pronounced regional variations of the SST change suggest important changes in the North Atlantic ocean circulation and its dynamics. The SST front along the Gulf Stream path shifts northward and weakens which might also impact the North Atlantic storm track as already shown for the current climate state (e.g. Minobe et al., 2008, 2010, Hand et al., 2014).

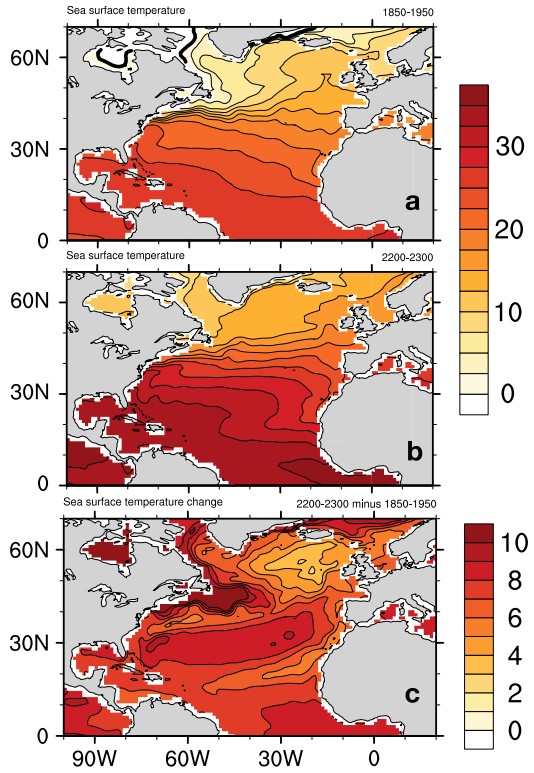

Figure 2.1: Sea surface temperature (°C) in **(a)** the historical simulation (1850-1950), **(b)** RCP8.5 (2200-2300) for the time mean and **(c)** difference between RCP8.5 and the historical simulation. Contour interval: $2.5°C$ in (a) and (b), $1°C$ in (c).

Projected changes in the North Atlantic horizontal gyre circulation and zonal-mean zonal wind

The area of reduced warming in the eastern SPG indicates changes in the North Atlantic ocean dynamics and in the gyre circulation (Drijfhout et al., 2012). The North Atlantic barotropic stream function shows substantial changes in the annual mean pattern (Fig.2.2). The barotropic stream function weakens in the subtropical gyre and intensifies in the SPG in RCP8.5. We observe a northward shift of the subtropical gyre and a northward shift of the boundary between subtropical and SPG by about 5 degrees between the HIST_{mean} (Fig.2.2a) and RCP_{mean} (Fig.2.2b) associated with the northward shift of the atmospheric wind field (Fig.2.2c).

The zonal-mean zonal wind across the Atlantic indicates considerable changes in the annual mean surface wind field in RCP8.5 (Fig.2.2c,2.3). Since this change is mostly a barotropic response of the zonal wind occurring similarly at upper levels (Fig.2.3), this suggests changes in the atmospheric Hadley

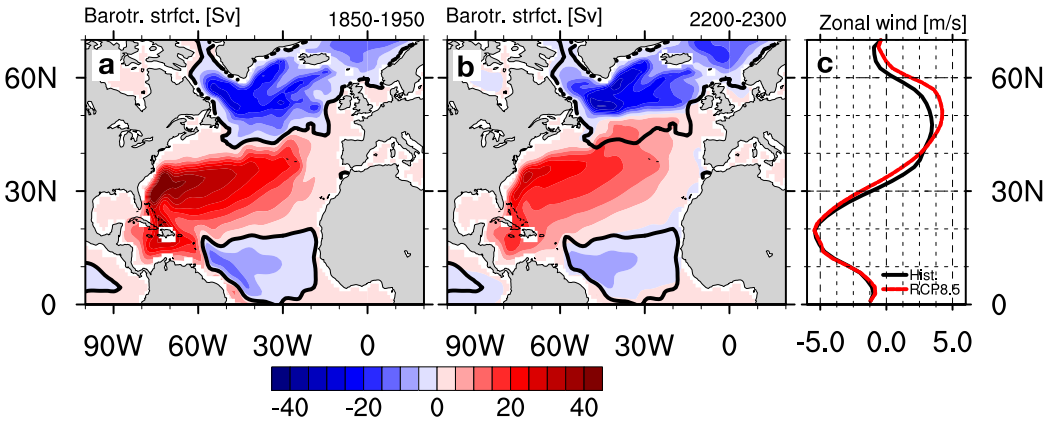

Figure 2.2: The barotropic streamfunction ($Sv = 10^6 m^3 s^{-1}$) in **(a)** the historical simulation (1850-1950) and **(b)** RCP8.5 (2200-2300) for the time mean over the respective period. The thick black line shows the zero contour in the historical simulation. Contour interval: 5 Sv. **(c)** Zonal mean zonal wind (at 1000 hPa) averaged over the North Atlantic region (90°W to 10°E) for the historical simulation (black) and RCP8.5 (red) indicating the northward shift of the westerlies.

circulation. As compared to the HIST$_{mean}$, the northern Hadley cell expands poleward and equatorward in RCP$_{mean}$ in MPI-ESM (Fig.2.3a) as in most CMIP5 models (e.g., Hu et al., 2013). A number of mechanisms has been proposed for the shift of the Hadley circulation and the westerlies (Lu et al., 2014, and references therein). As a consequence, the westerlies between 30°N and 60°N are shifted poleward in RCP8.5 by about 5 degrees (Fig.2.3b,c). This shift corresponds to a trend towards a more positive NAO phase, which yields an acceleration of the westerlies over large areas of the SPG (Fig.2.3b,c), along with a deceleration of the westerlies between 30°N - 40°N and a slight intensification of the trade winds south of 30°N. The shift leads to a deceleration of the westerlies between 30°N and 40°N, to a slight intensification of the trade winds south of 30°N and to an additional intensification of the westerlies over the SPG.

In concert with this intensification of the surface wind field the circulation of the SPG strengthens with an increase of the average transport by about 2 Sv, which might be related to changes in heat fluxes in the SPG (e.g. Eden and Willebrand, 2001, Eden and Jung, 2001, Barrier et al., 2014). Considering the flat-bottom Sverdrup transport in the subpolar gyre indicates only a weak increase of about 0.5 Sv in the gyre strength from HIST$_{mean}$ to RCP$_{mean}$ (not shown), suggesting that processes such as changes in surface heat fluxes

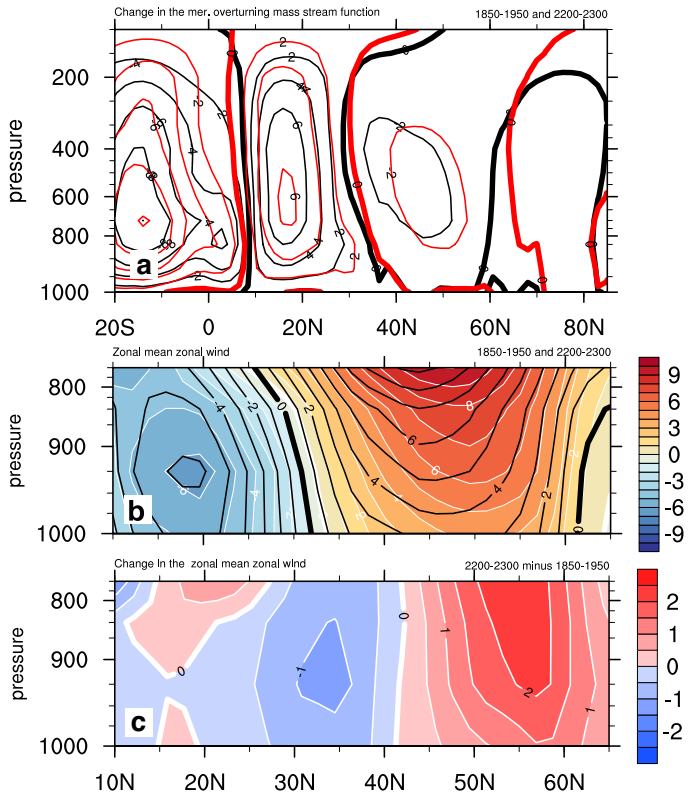

Figure 2.3: **(a)** The (global) meridional overturning mass stream function (in $10^{10}kg/s$ for the historical simulation (1850-1950, black contours) and RCP8.5 (2200-2300, red contours) between 20°S and 80°N. **(b)** Vertical profile of the zonal-mean zonal wind (ms^{-1}) over the North Atlantic averaged from 10°E to 90°W in the historical simulation (1850-1950, black contours) and RCP8.5 (2200-2300, colors) for the time-mean over the respective periods. **(c)** The difference of the zonal-mean zonal wind between RCP8.5 and the historical simulation. Contour interval: $2 \times 10^{10}kg/s$ in (a), $1m/s$ in (v), $0.5m/s$ in (c).

might be at work. The subtropical gyre shows a weakening in the barotropic streamfunction by about 20 Sv at its maximum at about 30°N indicating important changes in the dynamics of the subtropical gyre (Fig.2.2). In concert with the northward shift of the ocean circulation in RCP8.5 the Gulf Stream separates from the US coast further north in RCP8.5. This leads to the simulated changes in the SST front (Fig.2.1) along the path of the Gulf Stream.

2.1.2.2 The Atlantic meridional heat transport and its decomposition

Traditionally, the meridional heat transport **H** is diagnosed from the zonal and vertical integral of the heat flux across an east-west section through the Atlantic (e.g., Hall and Bryden, 1982):

$$\mathbf{H}(y) = \rho_0 c_p \int_{x_W}^{x_E} \int_{-H(x,y)}^{0} v(x,y,z)\theta(x,y,z)\ dz\ dx, \tag{2.1}$$

with ρ_0 a reference density, c_p the specific heat capacity of sea water, H the water depth, x_E and x_W the eastern and western boundaries of the transect, v the meridional velocity and θ the potential temperature in °C.

Impact of the variability of the temperature and velocity field on the OHT

In order to assess the impact of temporal variations in the velocity field and in the potential temperature field, we separate their seasonal variability. In a first step we calculate the OHT with an annual mean velocity field ($[v]$, Eq. 2.2), and in a second step with a time mean of the temperature field ($[\theta]$, Eq. 2.3) over the analyzed periods HIST_{mean} and RCP_{mean}. We consider the time mean of the v- (θ-) field but consider the full spatial variations of the respective field together with the full spatial and temporal variability of the θ- (v-) field, such that the two contributions can be calculated from

$$\mathbf{H}_{[v]}(y) = \rho_0\ c_p \int_{x_W}^{x_E} \int_{-H(x,y,z)}^{0} [v(x,y,z)]\,\theta(x,y,z)\ dz\ dx \tag{2.2}$$

$$\mathbf{H}_{[\theta]}(y) = \rho_0\ c_p \int_{x_W}^{x_E} \int_{-H(x,y,z)}^{0} v(x,y,z)\,[\theta(x,y,z)]\ dz\ dx \tag{2.3}$$

with v the meridional velocity, θ the temperature and $[v]$ and $[\theta]$ the time mean of the velocity and temperature (°C) field over the analyzed periods HIST_{mean} and RCP_{mean}. The two cases correspond to the time mean velocity field advecting the time-dependent temperature field and the time-dependent velocity field acting on the time mean temperature field.

Overturning and gyre component of the OHT

Well-established is the decomposition of the OHT into contributions from the zonal mean vertical circulation and the horizontal circulation by considering the zonal mean $(\overline{v}, \overline{\theta})$ and deviations from the zonal mean (v', θ') of the meridional velocity and temperature field respectively: $v = \overline{v} + v'$ and $\theta = \overline{\theta} + \theta'$ (e.g., Bryan, 1962, 1982a, Bryden and Imawaki, 2001). This yields for the OHT

$$\begin{aligned} \mathbf{H}(y) = & \underbrace{\rho_0 c_p \int_{x_W}^{x_E} \int_{-H(x,y)}^{0} \overline{v}(x,y,z)\overline{\theta}(x,y,z)\, dz\, dx}_{\mathbf{H}^{ov} = \text{overturning component}} \\ + & \underbrace{\rho_0 c_p \int_{x_W}^{x_E} \int_{-H(x,y)}^{0} v'(x,y,z)\theta'(x,y,z)\, dz\, dx}_{\mathbf{H}^{gyre} = \text{gyre component}} \\ + & \text{mixed terms} \end{aligned} \tag{2.4}$$

giving an overturning component $\mathbf{H}^{ov}$, a gyre component $\mathbf{H}^{gyre}$ from the horizontal gyre circulation and mixed terms which are small and which we thus neglect here. Traditionally, the overturning component is related to the zonally averaged vertical-meridional (overturning) circulation and the gyre component is related to the horizontal transport by the large-scale gyres and small-scale eddies.

Further, an Ekman heat transport contribution to the overturning heat transport can be calculated from

$$\mathbf{H}^{ov}_{ek}(y) = -c_p \int_{x_W}^{x_E} \frac{\tau_x(x,y)}{f(y)} \left(\theta_{ek}(x,y) - \langle[\theta(x,y,z)]\rangle\right) dx, \tag{2.5}$$

with τ_x the zonal wind stress, f the Coriolis parameter, $\langle[\theta]\rangle$ the section averaged temperature field and θ_{ek} the temperature of the Ekman layer following Böning and Hermann (1994). Here, the Ekman heat transport at the surface is assumed to be compensated by a deep return flow. We also assume θ_{ek} to be close to the surface temperature, which yields only small uncertainties (Johns et al., 2011). Jayne and Marotzke (2001) showed the computation of the Ekman heat transport to be valid for seasonal-to-interannual fluctuations, but not necessarily for the time mean heat transport, so that we apply

the Ekman transport calculation only to the OHT seasonal variability.

2.1.2.3 The vertical structure of the Atlantic meridional heat transport

To investigate the vertical structure of the OHT, we calculate the OHT in potential density classes, similar to the analysis of Talley (2003). We subdivide the water masses into surface, intermediate, North Atlantic Deep Water (NADW) and abyssal waters from the Antarctic Bottom Water (AABW). For this purpose, we define individual water masses relative to 26°N in the model based on a regression analysis of potential temperature θ and salinity S at 26°N on the AMOC at 26°N following Baehr et al. (2007). We perform the regression analysis for eastern boundary fields, western boundary fields and the zonal mean fields of θ and S for HIST$_{mean}$ and RCP$_{mean}$ individually. The regression analysis enables us to identify main water masses based on changes in the vertical profiles of the regression on the AMOC. In contrast

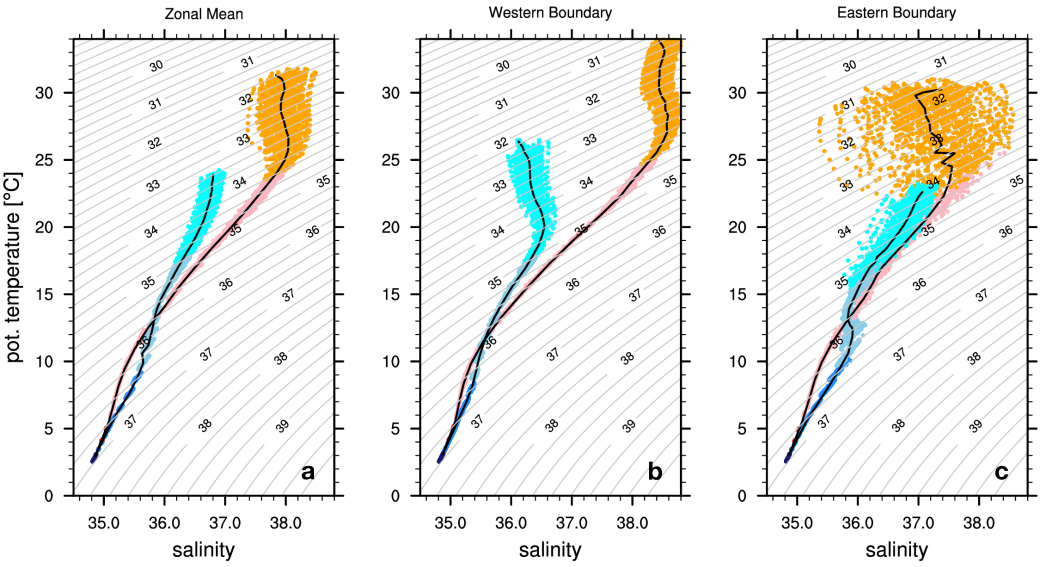

Figure 2.4: Temperature-salinity diagrams at 26°N for the historical simulation (1850-1950 in bluish colors) and RCP8.5 (2200-2300 in reddish colors) for **(a)** zonal mean, **(b)** western boundary and **(c)** eastern boundary temperatures and salinities. Watermasses of Antarctic bottom water (AABW), North Atlantic Deep Water (NADW) and intermediate and thermocline water are shown from dark to light colors. The black lines show the mean of the temperature-salinity diagrams averaged over density layers.

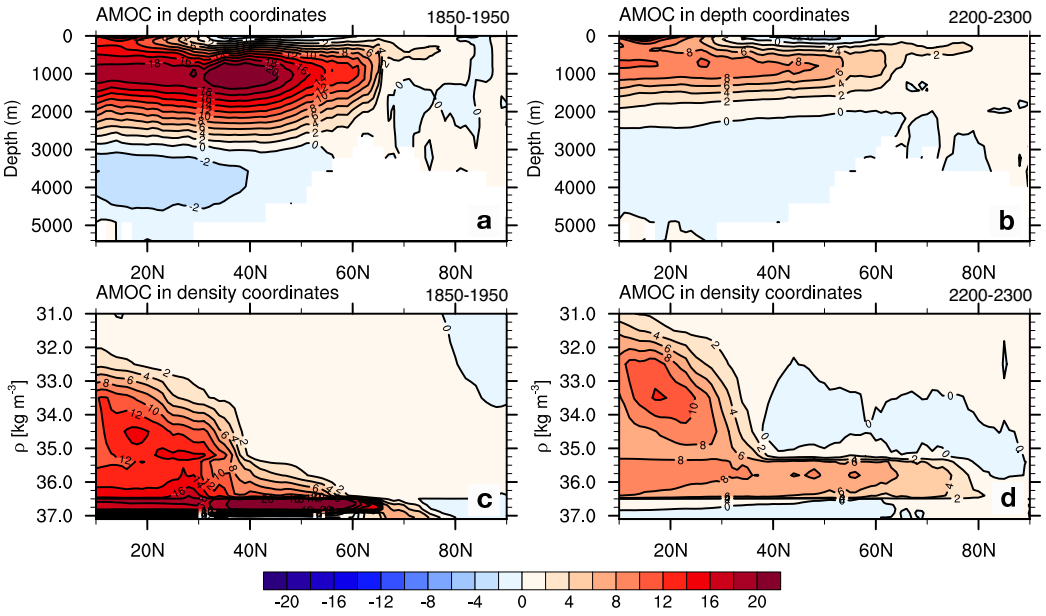

Figure 2.5: **(a)** and **(b)**: AMOC in depth coordinates. **(c)** and **(d)**: AMOC in density coordinates in the North Atlantic. (a) and (c) historical simulation (1850-1950), (b) and (d) RCP8.5 (2200-2300). Contour interval $2Sv$.

to Talley (2003), we use σ_2 (potential density referenced to 2000 dBar) as a definition for the individual water masses in the North Atlantic, which facilitates the analysis in the model. The corresponding temperature-salinity diagrams for HIST$_{mean}$ and RCP$_{mean}$ are shown in Fig.2.4. The temperature-salinity diagrams reveal changes in the water mass properties from HIST$_{mean}$ to RCP$_{mean}$ with warmer and saltier waters for surface and intermediate layers in RCP$_{mean}$ than in HIST$_{mean}$ reaching layers of lighter density in RCP$_{mean}$. Since we find changes in the density classes and the associated water mass characteristics between the historical simulation to RCP$_{mean}$, the water mass definitions differ between the HIST$_{mean}$ and RCP$_{mean}$. The individual water masses are therefore determined separately.

We subdivide the OHT into four layers with fixed potential density ranges: a surface layer, an intermediate layer, a layer comprising the North Atlantic Deep Water (=NADW, including Labrador Sea Water=LSW, Denmark Strait Overflow Water=DSOW and Iceland-Scotland Overflow Water=ISOW) and a bottom layer with the Antarctic Bottom Water (AABW). In HIST$_{mean}$ and RCP$_{mean}$ the surface layer is defined for densities $\sigma_2^{HIST} <= 35.2 kg/m^3$ and $\sigma_2^{RCP} <= 34.5 kg/m^3$, respectively, the intermediate layer is defined for

densities $35.2kg/m^3 < \sigma_2^{HIST} <= 35.8kg/m^3$ and $34.5kg/m^3 < \sigma_2^{RCP} <= 36.61kg/m^3$, respectively, the NADW is defined for densities $35.8kg/m^3 < \sigma_2^{HIST} <= 36.91kg/m^3$ and $36.61kg/m^3 < \sigma_2^{RCP} <= 36.91kg/m^3$, respectively, and the AABW is defined for densities $\sigma_2^{HIST} > 35.8kg/m^3$ and $\sigma_2^{RCP} > 36.91kg/m^3$, respectively. For each density range, we then calculate the heat fluxes and the corresponding seasonal cycles. In RCP8.5, the deep water formation in the North Atlantic is significantly reduced, leading to a change in the water mass distribution. In RCP8.5, it is not convenient anymore to define a traditional North Atlantic Deep Water, which is why the density classes used to define the individual water masses differ between the historical simulation and RCP8.5. A finer separation of individual water masses is not feasible in the model.

2.1.3 Mean changes in the Atlantic meridional overturning circulation and meridional heat transport

2.1.3.1 AMOC

The mean changes seen in the SSTs, the surface wind field and in the North Atlantic ocean and gyre circulation influence the AMOC and the meridional heat transport, which we focus on in the remainder of the study. The AMOC shows significant changes in the time mean from HIST_{mean} to RCP_{mean} (Fig.2.5). The AMOC calculated in depth coordinates shows that the northward overturning cell is reduced and shifted to the surface from the HIST_{mean} to RCP_{mean} (Fig.2.5a,b). The maximum of the stream function ψ given by $\psi(y,z) = \int_{z}^{0} \int_{x_W}^{x_E} v(x,y,z)\ dx\ dz$ commonly used as an index for the AMOC, is substantially reduced by 30 to 50% from HIST_{mean} to RCP_{mean} (Fig.2.5a,b;Fig.2.6a).

Considering the AMOC in density coordinates (Fig.2.5c,d) indicates a similar surfaceward shift of the AMOC cell to layers of lower density from HIST_{mean} to RCP_{mean} (Fig.2.5c,d). We find only a slight decrease of the

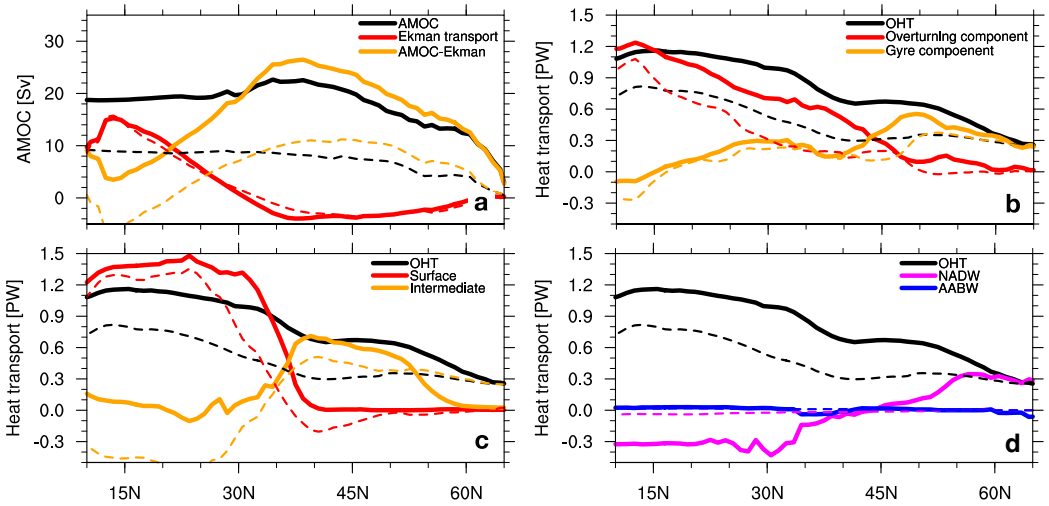

Figure 2.6: Change in **(a)** the time-mean Atlantic meridional overturning circulation, the Ekman transport and the geostrophic volume transport (≈AMOC-Ekman), **(b)** the time-mean Atlantic meridional heat transport (OHT) with overturning component and gyre component (in PW), **(c)** the time-mean OHT with contributions from the surface layer and intermediate layer (in PW) and **(d)** the time-mean OHT with contributions from the North Atlantic Deep Water (NADW) and Antarctic Bottom Water (AABW) (in PW). The historical simulation (1850-1950) is shown by solid lines, RCP8.5 (2200-2300) by dashed lines.

wind-driven surface cell in the tropics by about 2 Sv at the maximum, whereas the deep cell is reduced by more than 50% from a maximum of 24 Sv in HIST$_{mean}$ to about 10 Sv in RCP$_{mean}$. In RCP8.5, the formation of NADW in the Labrador Sea and the Nordic seas is almost absent for the 2200-2300 period. Instead of deep convection mixing surface water down to the bottom in about 3000m depth in the historical simulation, the maximum mixed layer depth is mostly limited to the upper 1000 meters in RCP8.5 (not shown), which thus directly reduces the deep branch of the AMOC. In addition, the AMOC's weakening is associated with a reduction of the geostrophic volume transport (Fig.2.6a). For simplicity, we approximate the geostrophic transport ψ_{geo} by the residual of ψ and the Ekman transport ψ_{ek} given by $\psi_{ek} = -\frac{1}{\rho_0 f}\int_{x_W}^{x_E} \tau_x \, dx$ with τ_x the zonal wind stress at the ocean surface: $\psi_{geo} \approx \psi - \psi_{ek}$. The geostrophic transport is proportional to the zonal cross-basin density gradient which is decreased from HIST$_{mean}$ to RCP$_{mean}$ and thus reduces the AMOC in the North Atlantic (not shown). The Ekman transport indicates only small and local changes from HIST$_{mean}$ to RCP$_{mean}$ that do not contribute significantly to

the weakening of the AMOC (Fig.2.6a).

2.1.3.2 OHT

Similar to the AMOC, the RCP8.5 scenario reveals considerable changes in the associated OHT. For RCP_{mean}, the OHT shows a pronounced weakening by 30-50% from about 1.2 PW to about 0.8 PW between 10°N and 30°N and from about 0.8 PW to about 0.4P W between 40°N and 55°N by the end of the 23rd century (Fig.2.6b). The reduction in the total OHT in the subtropical North Atlantic can be attributed almost entirely to a reduction in the overturning heat transport, while changes in the gyre component are comparably small. Only in the SPG, the gyre component also indicates a substantial weakening, so that both the overturning and the gyre component contribute to the reduction in the total heat transport in the subpolar North Atlantic. The reduction of the overturning heat transport can be attributed to a reduction of the geostrophic contribution to the AMOC (Fig.2.6a) and the associated reduction of the zonally-averaged geostrophic meridional velocity field.
The decomposition of the OHT into overturning and gyre component merely represents the vertical integral and thereby masks out any contribution from different layers and water masses in the North Atlantic. The vertical structure of the OHT shows that the northward heat transport is mostly confined to the surface layer in the tropical and subtropical North Atlantic in $HIST_{mean}$ and RCP_{mean} (Fig.2.6c). The intermediate water OHT increases from the subtropical to the subpolar gyre and dominates the total OHT north of about 40°N in $HIST_{mean}$ and RCP_{mean}. The NADW contributes with a southward (negative) heat transport to the total OHT in the subtropical gyre and thus partially compensates the surface intensified heat transport in $HIST_{mean}$. In the subpolar gyre, the OHT of the NADW changes to northward (positive) heat transports, significantly increases north of 50°N and dominates here the total OHT in $HIST_{mean}$. In RCP_{mean} the OHT of the NADW is significantly reduced in the whole North Atlantic. The OHT of the intermediate water changes to southward heat transports in the subtropical gyre, replaces and

even intensifies the southward OHT of the NADW. North of 50°N, the intermediate waters similarly replace the OHT of the NADW without a noticeable change in the OHT strength in RCP_{mean}.

2.1.4 Changes in the seasonal cycle of the Atlantic meridional heat transport

2.1.4.1 The total OHT

To assess the response of the seasonal cycle of the OHT to a changing climate in RCP8.5, we first analyze the full latitude dependent seasonal cycle of the OHT before focusing on anomalies of the OHT and its components in the North Atlantic. The seasonal cycle of the OHT shows regionally varying patterns with differences between the tropical North Atlantic, the subtropical gyre and the subpolar gyre (Fig.2.7). In the tropical North Atlantic, the seasonal maximum is in winter and the minimum in summer to autumn in $HIST_{mean}$ with peak to peak seasonal amplitude of about 2.4 PW. In the subtropical gyre, the seasonal cycle has a maximum in summer and a minimum in winter to spring with seasonal amplitude of about 0.5 PW. The seasonal cycle declines from the equator to the pole. Further north in the SPG, the seasonal cycle is strongly reduced with a maximum in spring and a minimum in autumn and seasonal amplitude of about 0.2 PW (Fig.2.7a).
The most obvious change in the OHT from the $HIST_{mean}$ to RCP_{mean} is the mean reduction of the heat transport, which appears in almost all months (Fig.2.7b). Since the changed seasonal cycle is superimposed on the strong reduction of the OHT, we consider in the following analysis anomalies of the seasonal cycle relative to the annual mean at every latitude (Fig.2.7c,d).
The seasonal anomalies indicate that changes in space and time occur in the OHT seasonal cycle from the $HIST_{mean}$ to RCP_{mean} (Fig.2.7c,d). First, the OHT seasonal cycle pattern shows a northward shift by about 5 degrees following the general northward shift of the atmospheric jet and the gyre circulation in RCP8.5. We also find a latitude dependent temporal shift of 1

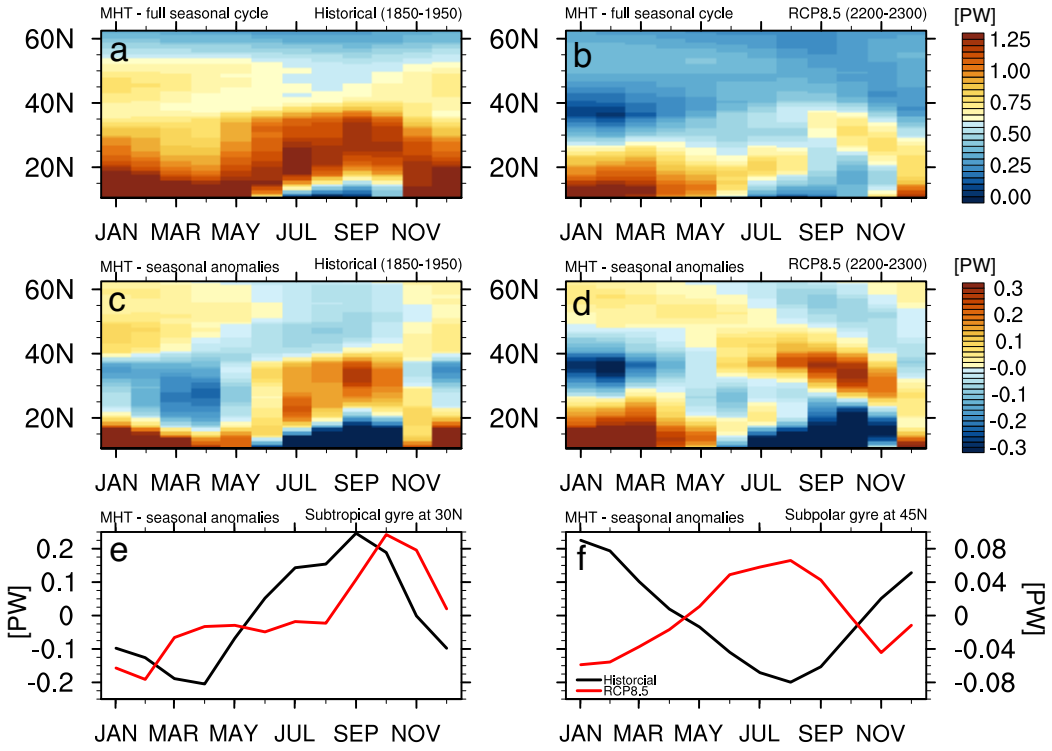

Figure 2.7: The Atlantic meridional heat transport seasonal cycle (in PW) in the historical simulation (1850-1950, **(a)** and **(c)**) to RCP8.5 (2200-2300, **(b)** and **(d)**). The OHT seasonal cycle in the historical simulation (1850-1950, black) and RCP8.5 (2200-2300, red) **(e)** at 30°N in the subtropical gyre and **(f)** at 45°N in the subpolar gyre. (a) and (b) show the full seasonal cyle, (c)-(f) show anomalies relative to the annual mean at every latitude. Colour interval in a-d: $0.02PW$.

to 6 months of the minima and maxima of the seasonal cycle. The temporal shift appears to be different between the tropical, subtropical and subpolar North Atlantic. Especially latitudes along the gyre boundaries between the tropical and subtropical North Atlantic (at about 20°N) and the subtropical and subpolar North Atlantic (at about 40°N) indicate significant phase shifts of 4 to 6 months. As an example for the subtropical and subpolar gyre, the OHT seasonal cycle at 30°N and 45°N from the HIST_{mean} to RCP_{mean} (Fig.2.7e-f) exhibits prominent changes in the amplitude, the phase and the general seasonality of the OHT. At 30°N, we find a relatively small change with a shift of two months for the minimum and of one month for the maximum to later months. In contrast, we find a reversal of the phase with a shift of six months of the maximum at 45°N. In addition, we find changes in the seasonal amplitude in RCP_{mean} which also depend on latitude and are

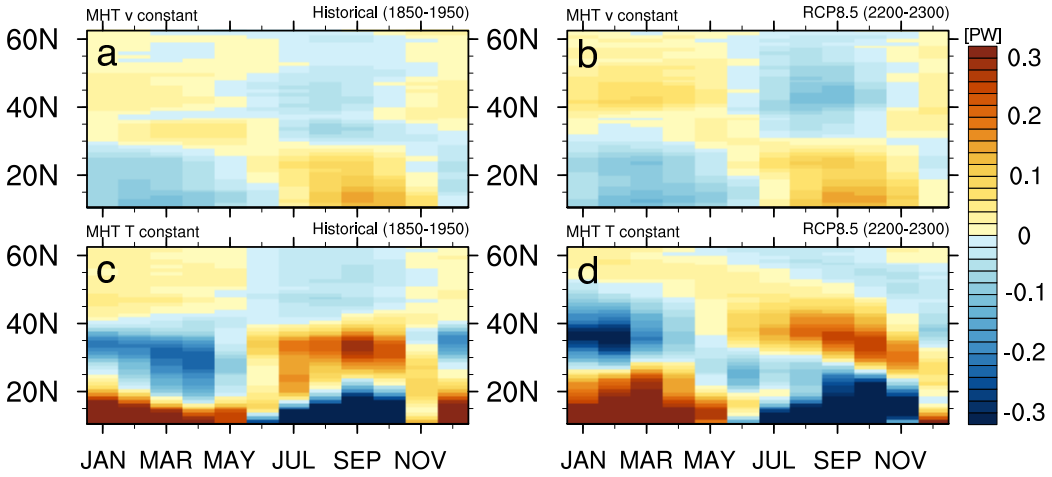

Figure 2.8: The Atlantic meridional heat transport seasonal cycle (in PW) in the historical simulation (1850-1950, **(a)** and **(c)**) and RCP8.5 (2200-2300, **(b)** and **(d)**) related to the variability in the temperature field (upper panels) and to variability in the velocity field (lower panels). Shown are anomalies relative to the annual mean at every latitude. Colour interval: $0.02PW$.

partly influenced by the northward shift. Between 30°N-40°N, the seasonal cycle generally exhibits an intensification, whereas the seasonal cycle between 40°N-50°N is influenced by the northward shift.

2.1.4.2 Vertically integrated meridional heat transport

Contributions from the seasonal variability in the temperature and velocity field

To identify whether changes in the seasonal cycle of the velocity field or in the temperature field dominate the changes seen in the total OHT, we consider the OHT with a time-mean velocity field $[v]$ (Eq.2.2) and a time-mean temperature field $[\theta]$ (Eq.2.3). The OHT based on $[v]$ (Fig.2.8a,b) reveals a reduced seasonality compared to the full OHT seasonal variability, especially in the tropical and subtropical North Atlantic. The changes in the seasonal cycle from HIST_{mean} to RCP_{mean} are rather small. The OHT based on $[\theta]$ (Fig.2.8c,d) reproduces the bulk of the total OHT seasonal cycle and also the changes in the seasonal cycle from HIST_{mean} to RCP_{mean}. This clearly indicates that the strongest changes in the OHT seasonal cycle mostly result from changes in the meridional velocity field, whereas the absolute

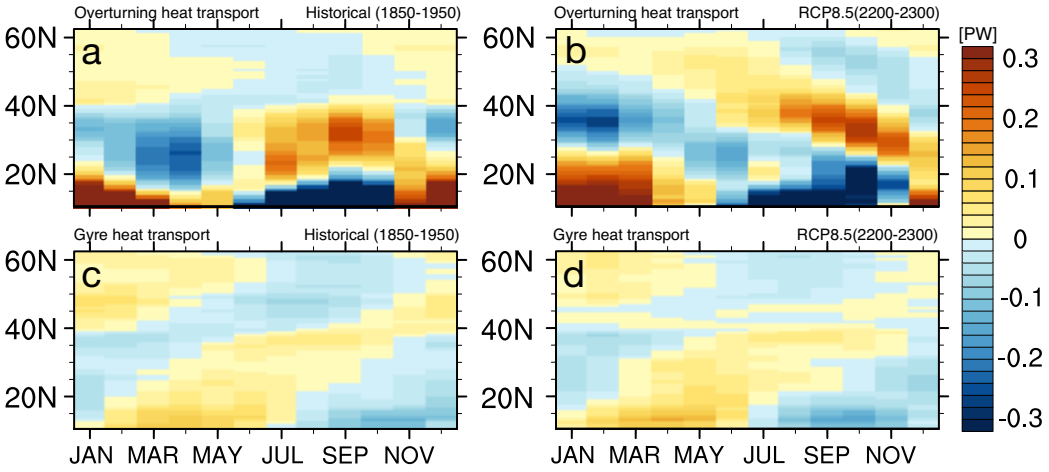

Figure 2.9: Seasonal cycle in the North Atlantic of **(a-b)** the overturning component and **(c-d)** the gyre component seasonal cycle (PW) from the historical simulation (1850-1950, left panel) to RCP8.5 (2200-2300, right panel). Shown are anomalies relative to the annual mean at every latitude. Contour interval: $0.02PW$.

warming of the ocean temperatures plays a less important role in directly changing the OHT seasonal cycle.

Overturning and gyre component

The decomposition of the OHT into overturning component and gyre component shows that the overturning component (Fig.2.9a,b) dominates the total OHT seasonal cycle with similar seasonal minima and maxima in the tropical and subtropical North Atlantic, similar to the time mean and longterm variability of the OHT. In the SPG, the influence of the overturning component on the seasonal cycle is smaller due to its weaker seasonal cycle and the gyre component gains influence on the OHT seasonal cycle similar to the time mean (Fig.2.9c,d). In the tropical and subtropical North Atlantic, the gyre component shows a seasonal maximum occurs between spring and summer, a minimum between autumn and winter, whereas in the SPG a maximum is in winter and a minimum in summer.

Regarding the changes in the seasonal cycle of the overturning component from HIST_{mean} to RCP_{mean}, we find clear similarities to the changes in the seasonal cycle of the total OHT (Fig.2.7) . We find a similar northward shift of the seasonal cycle pattern by about 5 degrees - suggesting a relation to the surface wind field - and comparable changes in the seasonal amplitude with

a 2-4 months shift of the minimum and maximum in the subtropical gyre and up to 6 months shift in the subpolar gyre. This close relation shows that changes in the seasonal cycle of the overturning component drive the changes in the seasonal cycle of the total OHT in both the subtropical and subpolar gyre (Fig.2.9a,b). Similarly, the overturning component determines changes in the seasonal amplitude of the total OHT, with a reduction in the seasonal amplitude in the tropics, an a slight increase of the amplitude between 30°N and 45°N.

In RCP_{mean} (Fig.2.9c,d), the gyre component reveals a slight intensification of the seasonal amplitude in tropical latitudes, while no significant changes in the seasonal amplitude occur in the subtropical and subpolar gyre. Apparently, important changes for the gyre component's seasonal cycle take place at about 40°N where the gyre boundary is situated in the model. We find a northward shift in the seasonal cycle pattern following the northward shift in the barotropic stream function and the zonal-mean zonal wind (Fig.2.2).

Zonal-mean zonal wind

The zonal-mean zonal wind also exhibits a seasonal cycle with the seasonal maximum of the atmospheric westerly jet in winter and meridional shifts of the position of the jet from summer to winter in HIST_{mean} (Fig.2.10a,b; shown is the full zonal-mean zonal velocity field). These seasonal variations undergo changes in amplitude and position of the jet, and temporal changes in the seasonal cycle in RCP8.5 (c.f. Lu et al., 2014). We find an intensification of the surface easterlies between 20°N and 30°N during winter and a reduction of the surface westerlies between 30°N and 40°N over the subtropical North Atlantic accompanied by an intensification of the westerlies over the subpolar North Atlantic (40°N-60°N) from HIST_{mean} to RCP_{mean}. Changes of the zonal wind during summer lead to reduced easterly winds over the subtropical gyre, reduced westerlies between 40°N and 50°N and enhanced westerlies north of 50°N during summer (Fig.2.10a,b). The westerlies (30°N-60°N) show a maximum seasonal amplitude of about 3m/s at the surface, which remains of the same amplitude in RCP8.5. The trade winds towards the equator (south of 30°N) show a seasonal amplitude of almost 6m/s, which decreases

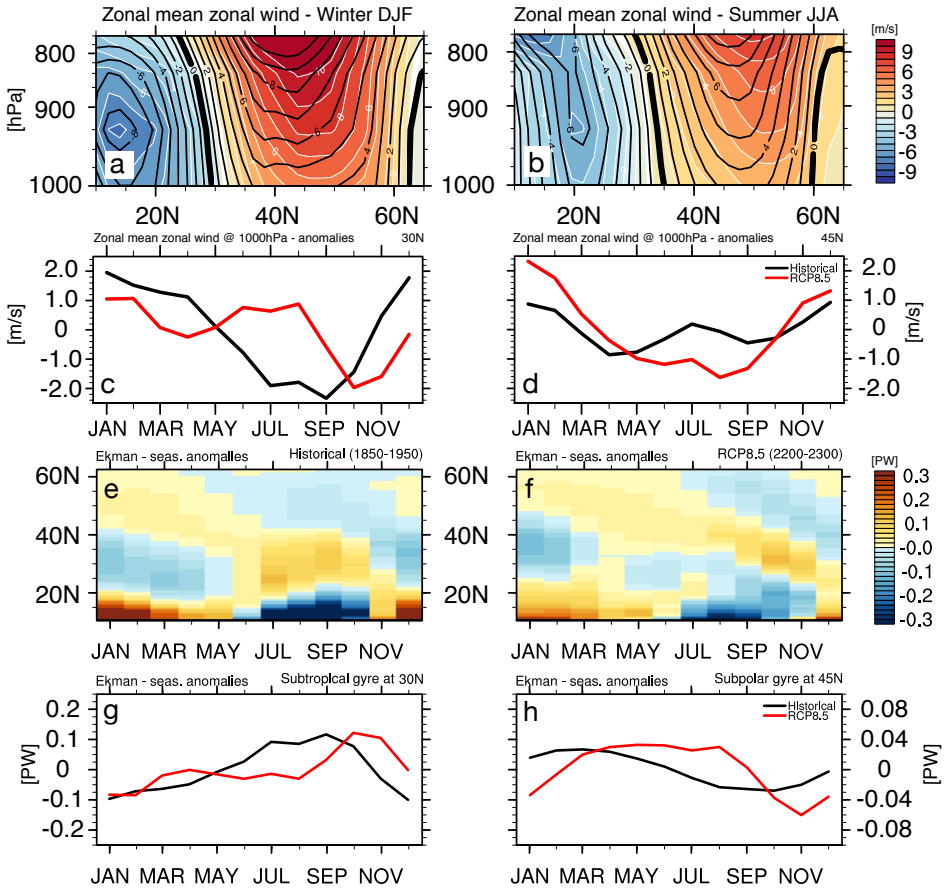

Figure 2.10: The zonal-mean zonal wind (ms^{-1}) over the North Atlantic averaged from 10°E to 90°W and the associated Ekman heat transport seasonal cycle [PW]. **(a-b)** Vertical profile of the zonal wind for historical conditions (1850-1950, black contours) and RCP8.5 (2200-2300). Contour interval: $1m/s$. **(c-d)** Seasonal cycle of the surface wind at 30°N and 45°N for historical conditions (1850-1950, black) and RCP8.5 (2200-2300, red). **(e-f)** Seasonal cycle of the associated Ekman heat transport in the North Atlantic for historical conditions (1850-1950) and RCP8.5 (2200-2300). Contour interval: $0.02PW$. **(g-h)** Seasonal cycle of the Ekman heat transport at 30°N and 45°N for historical conditions (1850-1950, black) and RCP8.5 (2200-2300, red).

to 3m/s in RCP8.5. As an example, the seasonal cycle of the zonal-mean zonal wind at the surface is shown at 30°N and 45°N for HIST_{mean} and RCP_{mean} (Fig.2.10c-d).

During winter, we find a northward expansion of the trade wind regime and of the maximum of the westerlies by about 5 degrees associated with the expansion of the Hadley cell. In contrast to the changes in winter, we find a general broadening of the westerlies during summer in RCP8.5, corresponding to a southward shift of the trade wind regime by about 2 degrees and a poleward shift of the maximum westerlies for RCP_{mean} (Fig.2.10a,b).

Ekman heat transport

The changes in seasonality of the zonal-mean zonal wind over the North Atlantic (Fig.2.10 a-d) directly project on the wind-driven Ekman heat transport (Fig.2.10 e-h). The Ekman heat transport in the tropical North Atlantic is dominated by the strong seasonal cycle of the trade wind regime and decreases northwards in the subtropical and subpolar gyre. In the tropical gyre, the seasonal cycle is strongest with a maximum in winter and a minimum in summer in HIST_{mean}. In the subtropical gyre, the Ekman heat transport has a reduced seasonal cycle with a maximum in summer and a minimum in winter. In the SPG, the seasonal cycle has a maximum in late winter to spring and a minimum in late summer (Fig.2.10e).

In RCP8.5 (Fig.2.10f), the weakening of the seasonal cycle in the zonal surface wind field leads to a weakened seasonal cycle of the Ekman heat transport in the tropical North Atlantic with a decrease in the seasonal amplitude by about 50%. In the subtropical gyre, we find a dominant influence of the northward shifted westerlies on the Ekman heat transport. The shift considerably changes the seasonal cycle of the Ekman heat transport depending on latitude, closely following the seasonal cycle of the surface wind. As an example, the Ekman heat transport seasonal cycle is shown at 45°N (Fig.2.10 g,h) in the subtropical gyre indicating the influence of the northward shifted pattern. A general weakening of the Ekman heat transport seasonal cycle is found over the southern part of the subtropical gyre to about 30°N resulting from a weakening in summer and a strengthening in winter. The Ekman heat transport in the SPG shows – in contrast to the subtropical gyre – relatively small changes in terms of the amplitude resulting in a slight strengthening in summer and a weakening in winter. (Fig.2.10 e-f)

The changes in the seasonal amplitude of the Ekman heat transport come in concert with a temporal shift of the seasonal minima and maxima (Fig.2.10 e-h). The Ekman heat transport in the tropical North Atlantic undergoes a 1-2 months temporal shift to later months for both the minimum and the maximum of the seasonal cycle. In the southern part of the subtropical gyre (about 20°N-30°N), we find the largest temporal shift of the seasonal maximum and minimum of 2-6 months to later months (Fig.2.10 e). In the northern part, the maximum is shifted by 1-2 months, as is the minimum.

The subpolar gyre region shows only small changes in the Ekman heat transport seasonal cycle for the minimum and maximum (1-2 months), while a latitude-dependent larger shift of about 5 months is observed for the maximum at about 40°N due to the northward shift of the pattern. (e.g., Fig.2.10 f).

The comparison of the changes in the OHT, the overturning component (Fig.2.9) and the Ekman heat transport reveals that changes in the Ekman heat transport (Fig.2.10) can explain a large part of the changes in the seasonal cycle of the OHT and overturning component: on the one hand by the Ekman heat transport's seasonal cycle contributing to the overturning component, on the other hand by effects from wind stress variability on the vertical motion (heaving and shoaling) of isopycnals which has been shown in earlier studies (Köhl, 2005, Chidichimo et al., 2010, Kanzow et al., 2010). Thereby, the velocity field is changed due to to changes in the surface wind stress.

2.1.4.3 Seasonal cycle in the vertical pathways of the OHT

In order to further understand whether the changes in the seasonal cycle of the OHT are driven by processes acting at the surface or in the deep ocean, we analyze the OHT seasonal cycle in density coordinates (Fig.2.11). In the surface layer, the OHT in density classes shows a strong seasonal cycle (Fig.2.11 c-d) in both HIST_{mean} and RCP_{mean} with seasonal amplitudes of about 3 PW and 2 PW, respectively. In HIST_{mean}, the tropical Atlantic has a maximum in winter and a minimum in summer. The subtropical gyre indicates a latitude dependent maximum from spring to summer and a minimum in winter. In the subpolar gyre, the seasonal cycle is weak and without a clear signature in HIST_{mean}. In RCP_{mean} the seasonal cycle in the surface layer generally intensifies in the subpolar gyre. In the tropical North Atlantic, the pattern shifts significantly northward and thus alters the seasonal cycle between 20°N to 30°N with temporal shifts of 4 to 6 months in the minimum and maximum. The surface layer seasonal cycle can be assumed to be mostly wind-driven in the tropical North Atlantic and

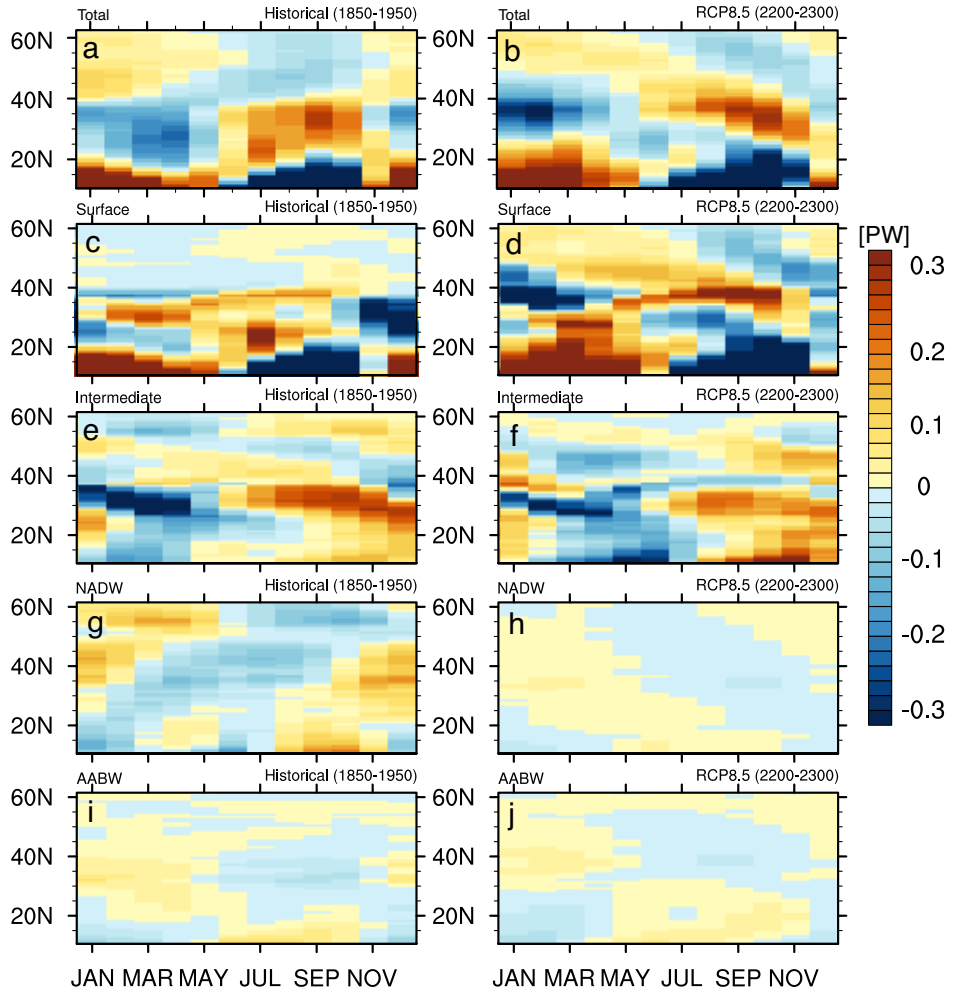

Figure 2.11: Contributions to the total OHT seasonal cycle from individual water masses calculated in potential density classes in the historical simulation (left) and RCP8.5 (right): **(a-b)** total OHT, **(c-d)** surface layer, **(e-f)** intermediate layer, **(g-h)** NADW and **(i-j)** AABW. Shown are anomalies relative to the annual mean at every latitude. Contour interval: $0.02PW$.

the subtropical gyre, so that the seasonal cycle also closely follows the Ekman heat transport seasonal cycle.

The intermediate water also indicates a relevant contribution to the OHT seasonal cycle (Fig.2.11 e-f). In the tropical and subtropical North Atlantic, the seasonal cycle of the intermediate water is mainly opposite to the seasonal cycle of the surface layer in both HIST_{mean} and RCP_{mean} and thus partly compensates the seasonal cycle in the surface layer. In the tropical and subtropical North Atlantic, the intermediate layer seasonal cycle has a minimum in late winter to spring and a maximum in autumn to winter in

$HIST_{mean}$, as well as a minimum in winter to spring and a maximum in autumn to winter in RCP_{mean}. From $HIST_{mean}$ to RCP_{mean}, the pattern shows shifts in the seasonal cycle of about 1 month to later months, but no clear northward shift as in the surface layer. The seasonal cycle in the subpolar gyre indicates general phase shift of up to 6 months from $HIST_{mean}$ to RCP_{mean} with a shift of the maximum from summer to winter between approximately 40°N to 50°N and a shift of the maximum from winter to spring between 50°N and 60°N.

In the NADW (Fig.2.11 g-h), significant changes occur resulting from changes in the water mass formation in the North Atlantic. In the $HIST_{mean}$, the formation of NADW is present and leads to a seasonal cycle in the OHT of the NADW giving an important contribution especially in the subpolar gyre. In the subpolar gyre, the NADW shows a maximum in winter to spring and a minimum in summer to autumn. In the subtropical gyre, the NADW seasonal maximum is in winter, the minimum in spring to summer. In RCP_{mean} the seasonal cycle is almost not existent in the remaining OHT of the NADW with a decrease of the seasonal amplitude from about 0.2 PW to almost 0 PW, thus showing a surface-ward shift of the processes acting on the OHT seasonal cycle.

The AABW seasonal cycle is generally weak and thus does not significantly contribute to the full OHT seasonal cycle (Fig.2.11 i-j). Still, we find a seasonal cycle in $HIST_{mean}$ with a maximum in summer and a minimum in winter in the tropical North Atlantic, and a maximum in winter and a minimum in late summer in the subtropical and subpolar gyre. For RCP_{mean} we find changes in the seasonal cycle with a northward shift of the pattern and also latitude dependent temporal shifts. These changes in the AABW might result from changed dynamics in the Southern Ocean also influencing the global ocean circulation, which we do not focus on in this study and thus need further analysis.

2.1.5 Discussion

The changes in the Atlantic meridional heat transport in future climate projections in MPI-ESM are accompanied by changes in the seasonal cycle of the oceanic OHT. Based on the scenario RCP8.5, we have identified changes in the mean climate state of the North Atlantic and in the associated seasonal cycle of the OHT.

We find a weakening of the mean OHT by 30-50% associated with a weakening of the overturning heat transport in RCP8.5. The weakening of the mean OHT comes in concert with the weakening of the AMOC's geostrophic transport by the end of the 23rd century in MPI-ESM indicating a direct relation between OHT and AMOC's strength. This direct relation has also been found from observations and model studies based on the RAPID array in the North Atlantic (e.g. Johns et al., 2011, Msadek et al., 2013). Recent CMIP5 experiments show an overall reduction of the AMOC in the multi-model ensemble by about 40% for RCP8.5 by the end of the 23rd century (Weaver et al., 2012, Cheng et al., 2013), which can be attributed to a reduction of deep water formation in the North Atlantic, especially in the Labrador Sea and Greenland Sea (Vellinga and Wood, 2002). As shown for the AMOC in density coordinates, the deep overturning cell which is fed by the NADW is strongly weakened in RCP8.5 in accordance with the absence of deep water formation in the Nordic seas and the Labrador Sea.

The general AMOC weakening found in most models of the CMIP5 multi-model ensemble gives reason to expect that a similar weakening of the OHT as found in MPI-ESM might be found in other CMIP5 models. As shown by Drijfhout et al. (2012), various CMIP5 models show the prominent area of reduced warming ("warming hole") in the subpolar North Atlantic surface temperatures for longterm changes, which can already be seen in the historical simulations as well as in recent observations from the Goddard Institute for Space Studies surface temperature analysis dataset (Hansen et al., 2010). This signal might be related to an adjustment of the gyre circulation already taking place in the present climate state that preconditions a decline of the AMOC and of the associated OHT, as well as possible changes in the seasonal

cycle.

Bryan (1982b) and subsequent studies have shown that the Ekman (heat) transport is responsible for a large fraction of the seasonal variability of the overturning heat transport and thus of the total oceanic OHT. We have shown that under climate change the overturning heat transport constitutes the prominent factor for the OHT seasonal cycle on the one hand, and that the overturning heat transport is also the most important term leading to the changes in the OHT seasonal cycle on the other hand. These changes in the overturning heat transport are mostly wind-driven by the Ekman heat transport and by wind-induced changes in the geostrophic velocities from a wind-driven heaving and shoaling of the isopycnal slope, as shown for the AMOC seasonal cycle in observations (Kanzow et al., 2010). Changes in the Ekman transport and the associated vertical Ekman velocities change the isopycnal slope and thus the geostrophic velocity field.

We find that the seasonal cycle of the OHT largely adjusts to a changed seasonality of the atmospheric circulation in RCP8.5. The wind-driven changes are impacted by a seasonally dependent northward shift of the atmospheric jet resulting in changes in the seasonal cycle of the Ekman heat transport and lead to temporal shifts in the OHT seasonal cycle. Changes in the seasonal cycle for extreme climate change scenarios have also been found in atmospheric variables such as surface temperatures and precipitation (Dwyer et al., 2012, Donohoe and Battisti, 2013, Dwyer et al., 2014).

Most prominent among the atmospheric changes with climate change is the poleward expansion of the Hadley cell and the associated northward shift of the mid-latitude westerlies (Lu et al., 2014). A warmer planet has been shown to lead to an expansion of the Hadley cell and a poleward shift of the westerlies in both dynamical core (Butler et al., 2010) and complex climate models (Lu et al., 2008). According to Toggweiler (2009) the northward shift of the westerlies follows a simple mechanism: a systematically warmer Northern Hemisphere leads to a poleward shift of the westerlies. Under global warming, the Northern Hemisphere undergoes a stronger warming than the Southern Hemisphere and the hemispheric temperature asymmetry increases. This leads to an additional northward shift of the ITCZ and the position of the westerlies. But the exact mechanism leading to the shift of the ITCZ and

the westerlies is still not fully understood and under discussion (Seidel et al., 2008), especially in CMIP5 models where the problem of a double ITCZ occurs (Hwang and Frierson, 2013, Christensen et al., 2013).
As shown by Hu et al. (2013) almost all CMIP5 models show a trend of poleward expansion of the Hadley cell in the RCP4.5 and RCP8.5 scenarios for the period 2006 to 2100. This trend of poleward expansion already manifests itself in the CMIP5 historical simulations. Hu et al. also show that the historical simulations underestimate the trend in the poleward expansion of the Hadley cell represented by reanalysis data, although it is unclear whether the trend is anthropogenically forced or whether the models capture the natural variability and extent of the Hadley cell correctly. But changes in the surface winds and wind stress may be model dependent and may differ in detail, i.e. some models do not project a northward shift of the westerlies directly at the surface and in the associated surface wind stress. Thus, the proposed mechanism for changes in the seasonal cycle of the oceanic OHT by the Ekman heat transport and the associated changes in the geostrophic velocity field might differ between individual models used for the CMIP5 multi-model ensemble and might require a similar analysis in other CMIP5 models.
The calculation of the OHT in density coordinates shows – as expected – that the seasonal cycle is mostly confined to the upper layers of the ocean. The surface is mostly wind-driven in the subtropical North Atlantic, in intermediate layers a return flow balances the Ekman transport. The NADW contributes to the OHT only in the historical simulation and dominates over the seasonal cycle of the surface circulation in the subpolar gyre. Due to the absence of deepwater formation in the Labrador Sea and Nordic seas in RCP8.5, the seasonal cycle in a future climate is mostly wind-driven in both the subtropical and subpolar gyre. This is in contrast to the present climate state in the model.
The strong decrease of the mean overturning heat transport leading to the 30-50% decrease in the OHT suggests that either the reduced meridional temperature gradient requires less heat to be transported to the poles or that a compensation mechanism must be at work, bringing additional heat from the equator to the poles to obtain a closed heat budget. In MPI-ESM, the atmosphere compensates the decrease in the meridional ocean heat trans-

port, implying an increased atmospheric heat transport (not shown), as also suggested by Rose and Ferreira (2012). A deeper analysis of the atmospheric compensation and changes in the atmospheric heat transport is needed, but is beyond the scope of our study.

The advection of heat by the ocean determines ocean heat storage rates and is an important factor for air-sea heat exchange (Dong et al., 2007), and thus for carrying heat to the North Atlantic sector and especially towards the European continent. By the changed ocean and heat transport dynamics, the surface air-sea heat fluxes are presumably exposed to changes regarding areas of heat flux divergences and convergences and thus of heat exchange and also shifts in the seasonal cycle of surface heat fluxes, which might affect the climate over Europe.

In agreement with other studies (e.g., Gregory et al., 2005), the cooling associated with the decline of the OHT and the AMOC is smaller than the radiative heating of the atmospheric temperatures due to global warming. This yields an overall increase in surface temperature in the North Atlantic sector. Hence, it is difficult to clearly separate the effect of the reduced ocean heat transport on surface temperatures from the increased radiative heating of surface temperatures. To identify this impact of the reduced OHT and changes in the OHT seasonal cycle, further studies will be required for clarifying the impact of a reduction and a changed seasonal cycle of the OHT on the North Atlantic sector and European climate.

2.1.6 Conclusions

Based on our analysis in the MPI-ESM CMIP5 climate projection RCP8.5, we conclude for the Atlantic Ocean meridional heat transport:

1. Along with a 30 to 50% decline of the time-mean OHT, the seasonal cycle of the OHT is shifted in time (1 to 6 months, depending on latitude and season) and in space (5° northward) in both the subtropical and subpolar gyre in RCP8.5.

2. These changes stem from a latitude-dependent altered seasonal cycle and a northward shift in the zonal-mean zonal wind (about 5° northward) and the resulting changes in the surface wind field that lead to a shift by 1 to 5 months in the seasonal cycle of the Ekman heat transport and the overturning heat transport.

3. The vertical structure of the OHT reveals that in tropical and subtropical North Atlantic, the OHT seasonal cycle is mostly forced and mostly changed in the surface and intermediate layer, where the wind acts as the dominant direct driver of the seasonal variability and leads to temporal shifts from 1 to 6 months.

4. In the subpolar North Atlantic, the process of deep water formation results in a contribution of NADW to the seasonal cycle in the historical simulation (0.2 PW seasonal amplitude), while this contribution is significantly reduced in RCP8.5 (almost 0 PW seasonal amplitude) due to a reduction in the North Atlantic deep water formation.

5. Thus, the changes in the total OHT seasonal cycle in the subtropical gyre result mostly from the wind-driven and surface-intensified part of the overturning heat transport, whereas in the subpolar gyre, the changes in the seasonal cycle are dominated by the reduction in the seasonal cycle of the NADW.

These findings may have important implications for the impact of climate change on the decadal predictability of the AMOC and the OHT.

Acknowledgements

This work was supported by the Cooperative Project RACE - Regional Atlantic Circulation and Global Change funded through the German Federal Ministry for Education and Research (BMBF), 03F0651A (MF, JB), and by the Cluster of Excellence CliSAP (EXC177), Universität Hamburg, funded through the German Research Foundation (DFG) (DD and JB). The work

of WM was supported by the German Federal Ministry for Education and Research (BMBF) project MiKlip (PT01LP1144A). Further, research leading to these results has received funding from the European Unions Seventh Framework Programme (FP7/2007-2013) under grant agreement no. 308378 ENV.2012.6.1-1: Seasonal-to-decadal climate predictions towards climate services [http://www.specs-fp7.eu/]. The climate simulations were performed at the German Climate Computing Centre (DKRZ). We thank Ralf Hand for stimulating discussions and the three anonymous reviewers for their constructive comments on an earlier version of the manuscript.

2.2 The seasonal cycle of the Atlantic meridional heat transport in potential temperature coordinates

2.2.1 Introduction

The Atlantic meridional heat transport (OHT) is traditionally considered as the full zonal and vertical (top to bottom) integral of the meridional temperature flux which ensures a zero net mass flux across a latitude (Bryan, 1962, 1982a, Bryden and Imawaki, 2001, Siedler et al., 2013). The contribution of the vertical meridional overturning circulation, the horizontal gyre circulation and the oceanic eddy field is usually described by a decomposition of the OHT in overturning and gyre heat transport (c.f section 2.1, Eq.2.4). But, the vertical integration of the OHT prevents to understand the vertical structure of the OHT and the relative contributions to the total OHT from individual layers and circulation cells of the meridional overturning circulation.

Recently, various approaches based on either observations or model experiments have shown contributions of individual water masses and layers to the total OHT (Talley, 2003, Boccaletti et al., 2005, Ferrari and Ferreira, 2011). The analysis of Talley (2003), based on observations in the North Atlantic, considered layers of different densities representing the water masses in the Atlantic. She found that 60% of the mean OHT at 24°N in the North Atlantic results from the intermediate and deep overturning, while the remaining 40% are carried northward in a shallow overturning layer, in contrast to the traditional view, where about 90% of the heat transport are ascribed to the deep overturning circulation at 25°N (e.g. Bryden and Imawaki, 2001).

Boccaletti et al. (2005) and Ferrari and Ferreira (2011) analyzed the vertical structure of the heat transport based on a heat function in depth and temperature coordinates. Boccaletti et al. (2005) used numerical model experiments to calculate a heat function in cartesian (depth) coordinates. By the choice

of the coordinate system, Boccaletti et al. were confronted with recirculation cells, that might occur in the calculation in depth coordinates. Following this idea, Ferrari and Ferreira (2011) circumvented the problem of recirculation cells by calculating the heat function in temperature coordinates. By their choice, they could filter out recirculations automatically and thus, simplify the calculation of the vertical pathways of the heat transport. Ferrari and Ferreira (2011) showed that the OHT is surface intensified and follows from a combined circulation of cold and warm water masses, so that most of the heat transport cannot be assigned to shallow or deep circulations only.
As an alternative formulation of the vertical structure of the OHT to chapter 2.1, I analyze here the OHT seasonal cycle based on a heat function in temperature coordinates following Ferrari and Ferreira (2011) with the aim to identity the impact of changes in the heat function and closed circulation cells on the OHT seasonal cycle in MPI-ESM. Specifically, I analyze changes in the meridional overturning circulation in potential temperature coordinates and the associated OHT from the present climate state in the historical simulation (1850-1950, HIST_{mean}) to RCP8.5 (2200-2300, RCP_{mean}) with focus on longterm changes in RCP8.5.

2.2.2 The heat function as a representation of the meridional heat transport

In a simplified two dimensional circulation in a y-z plane, the meridional heat transport can be written as (Ferrari and Ferreira, 2011):

$$H = \rho_0 c_p \int v\theta \; dz = \rho_0 c_p \int \psi \; d\theta \tag{2.6}$$

with ρ_0 a reference density, v the meridional velocity and θ the potential temperature. $H = \rho_0 c_p \int \psi \; d\theta$ shows, that the OHT can be expressed by the integral of the mass transport in temperature layers, as similarly shown by Bryan and Sarmiento (1985), Klinger and Marotzke (2000) and Vallis and Farneti (2009). Vallis and Farneti decomposed the integral in H in two parts, the first from the surface temperature to the temperature separating surface

and deep circulations, the second over the remaining cold temperatures.
Ferrari and Ferreira (2011) extended the approach to involve overlapping circulations in same temperature classes, what they call mixed overturning circulations. By their definition, the heat function in potential temperature coordinates can be derived from the stream function Ψ of the zonally averaged mass flux in temperature coordinates as follows:

$$\Psi(y,\theta) = \overline{\int\int_{\theta' \leq \theta} v dx dz}. \tag{2.7}$$

The overbar denotes a long-time average of the stream function at latitude y and temperature θ. It can be shown, that this stream function describes the residual overturning streamfunction (Andrews, 1983) in θ coordinates, and thus involves contributions from both, the mean flow and from the bolus flow from the eddy field (deviations from the zonal and temporal mean; Nurser and Lee, 2004).
A heat function H in steady state can then be defined as

$$H(y,\theta) \equiv \int_{\theta_B}^{\theta} \rho_0 c_p \Psi(y,\theta)\ d\theta, \tag{2.8}$$

where Ψ is the mass stream function. A more detailed derivation of H is given in Ferrari and Ferreira (2011).
To identify now individual pathways of the OHT in the overturning circulation, we consider a combination of the heat function and the overturning stream function. Based on the overturning stream function, we define closed overturning circulation cells for the OHT for temperature ranges between θ_u and θ_l

$$OHT(y,\theta_u,\theta_l) = \int_{\theta_l}^{\theta_u} \rho_0 c_p (\Psi(y,\theta) - \Psi(y,\theta_l))\ d\theta. \tag{2.9}$$

For circulations enclosed from other flows, the surrounding flow $\rho_0 c_p \Psi(y,\theta_l)(\theta_u - \theta_l)$ must be subtracted:

$$OHT(y,\theta_u,\theta_l) = H(y,\theta_u) - H(y,\theta_l) - \rho_0 c_p \Psi(y,\theta_l)(\theta_u - \theta_l) \tag{2.10}$$

Ultimately, this definition of the OHT only applies to the time mean OHT and not necessarily to the time-varying OHT. Although the model simulations are far from steady state due to increasing GHG forcing and a general slowdown of the AMOC and OHT in RCP8.5, I use the heat function as one further approach to analyze changes in individual branches of the OHT seasonal cycle under climate change in the following, since a theory of the heat function for a non-steady state is still lacking (e.g., Ferrari and Ferreira, 2011). I consider each state in the respective periods HIST_{mean} and RCP_{mean} to be close enough to steady state with only small differences in the mean to be able to compare the two states.

2.2.3 The AMOC, the heat function and the associated meridional heat transport seasonal cycle in MPI-ESM

2.2.3.1 Mean changes in the AMOC and the associated heat function

The MPI-ESM overturning stream function in depth coordinates and potential temperature coordinates is shown in Fig.2.12 a-d for the historical simulation (1850-1950) and RCP8.5 (2200-2300). The overturning cell in depth coordinates shows the common picture with a strong closed circulation cell close to the surface and a weak negative cell close to the bottom. From HIST_{mean} to RCP_{mean}, the overturning stream function shows a significant weakening of the maximum by about 50% and a surface ward shift of the overturning cell (Fig.2.12a-b).

The overturning cell in temperature coordinates (Fig.2.12c-d) shows a similar structure as the overturning cell calculated in isopycnal coordinates (Fig.2.5c-d). To obtain the contributions of individual closed circulations to the total heat transport, I identify closed circulations in HIST_{mean} and RCP_{mean}. Both reveal a warm cell at the surface with a maximum at about 25°N, that can be assumed to be mostly wind-driven, and a cold cell

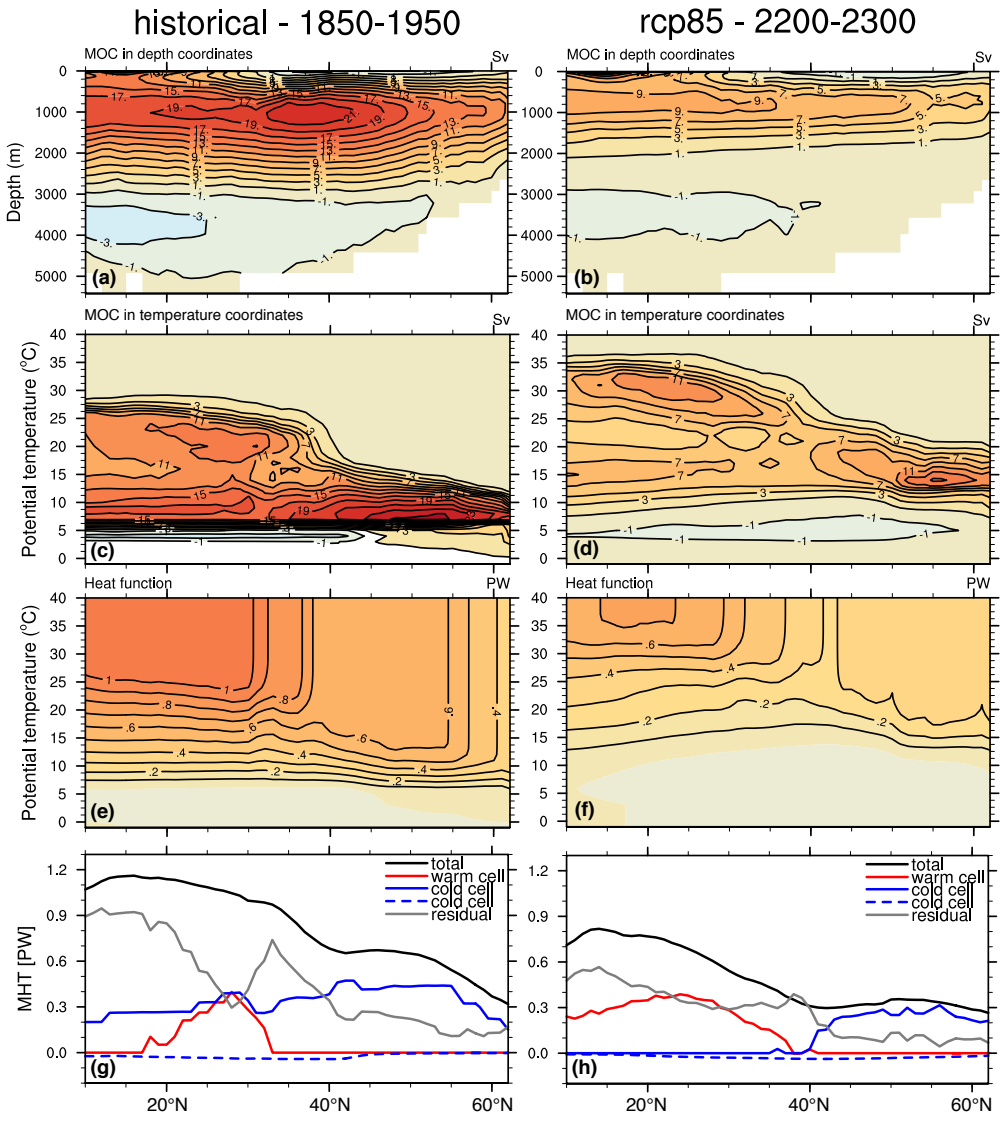

Figure 2.12: (a) AMOC in depth coordinates, (b) AMOC in potential temperature coordinates, (c) heatfunction H and (d) contributions of individual circulations to the total heat transport.

associated with the North Atlantic Intermediate Water (NAIW) and the North Atlantic Deep Water (NADW) in layers of colder temperatures, driven by the deep circulation, with a prominent maximum in the subpolar gyre at about 50°N. Additionally, a further cold cell incorporating cold waters of the Antarctic Bottom Water (AABW) for the lowest temperature layers can be defined. In the HIST$_{mean}$ the cold cells expand through the

whole North Atlantic across the equator into the South Atlantic (not shown). The areas of the overturning circulation that cannot be ascribed to closed circulations driven either by the wind or by the deep circulation are referred to as mixed circulation or residual circulation and provide a significant contribution to the overturning circulation similar to Ferrari and Ferreira (2011).

In RCP_{mean} (Fig.2.12 d) the overturning stream function is – compared to HIST_{mean} – generally shifted towards warmer temperatures following the general warming of ocean temperatures in RCP8.5. The warm cell in the subtropics indicates an "upward" shift of about 20°C and expands to the North and to the South, whereas the cold bottom cell shows and "upward" shift of about 5°C. In contrast to HIST_{mean}, the second cold cell related to the NAIW and NADW is limited to the subpolar North Atlantic in RCP_{mean}. From HIST_{mean} to RCP_{mean}, the stream function also indicates a significant reduction in the maximum by about 50% corresponding to the changes of the AMOC seen in chapter 2.1.

The overturning stream function in temperature coordinates allows now to specifically integrate the stream function over temperature to obtain the heat function H (Fig.2.12 e-f) following Eq.2.8 and then to diagnose contributions of the individual circulations to the total OHT in HIST_{mean} and RCP_{mean}. Due to the restriction to steady state in the heatfunction calculation used here, small differences occur in the mean total OHT (not shown). Since the differences are small, I stick to the definition of the heat function given by Ferrari and Ferreira (2011) in the following. To expand the heatfunction to be valid without restrictions for non-steady state, further work is required and left for future research.

The heat function in the historical simulation reveals a similar structure as in Ferrari and Ferreira (2011). The magnitude of the heat function increases from the cold to the warm layers and decreases from the equator to the north pole. The maximum of the heat function in the warmest layer represents the total Atlantic meridional heat transport. The overall maximum is – as for the total OHT – located in the tropical North Atlantic at about 15°N with maximum heat transports of about 1.2 PW.

From HIST_{mean} to RCP_{mean} the heat function reveals that the shift to

warmer temperature layers and the reduction in the overturning stream function comes along with a similar shift and reduction in the heat function across all latitudes. The maximum cell is shifted by about 10°C "upwards" to warmer temperature layers and is decreased to about 0.7 PW at about 20°N (Fig.2.12 e-f). In a subsequent step, the heat function is used to analyze the changes in the vertical structure of the OHT.

2.2.3.2 Mean changes in the OHT in temperature coordinates

In the historical simulation, total OHT attains a net heat transport of about 1.2 PW at its maximum at about 15°N, that decreases northward and results in a northward OHT of around 0.6 PW in the subpolar North Atlantic (Fig.2.12g-h). The cold NADW cell accomplishes a large amount of the total heat transport in the North Atlantic ranging between about 0.2 to 0.5 PW. The warm surface cell spans from 15°N to 35°N and contributes only locally to the total OHT because of its a maximum that is as strong as the cold cell in the subtropical gyre. In the tropical and subtropical North Atlantic, most of the OHT is accomplished by the residual or mixed circulation which cannot not be clearly ascribed to the wind-driven overturning or the deep circulation. The OHT related to the residual is calculated from the residual of the total OHT, the OHT associated with the warm cell and the two cold cells. The OHT in the subpolar gyre is driven by two-thirds by the cold cell, the mixed circulation contributes about one-third to the total OHT. The cold bottom cell gives only a small negative transport in the whole North Atlantic and thus is of minor relevance for the net transport of heat as well as associated changes in the time-mean OHT (Fig.2.12g).

In RCP_{mean}, the contributions to the OHT change slightly (Fig.2.12h). Due to the reduction in the cold cell, the associated heat transport is confined to the subpolar gyre and its maximum is reduced from about 0.5 PW to 0.3 PW. In contrast, the warm surface cell expands equator-ward and northward, while the maximum remains at about 0.4 PW. Because the total OHT significantly decreases in RCP8.5, the relative contribution of the residual

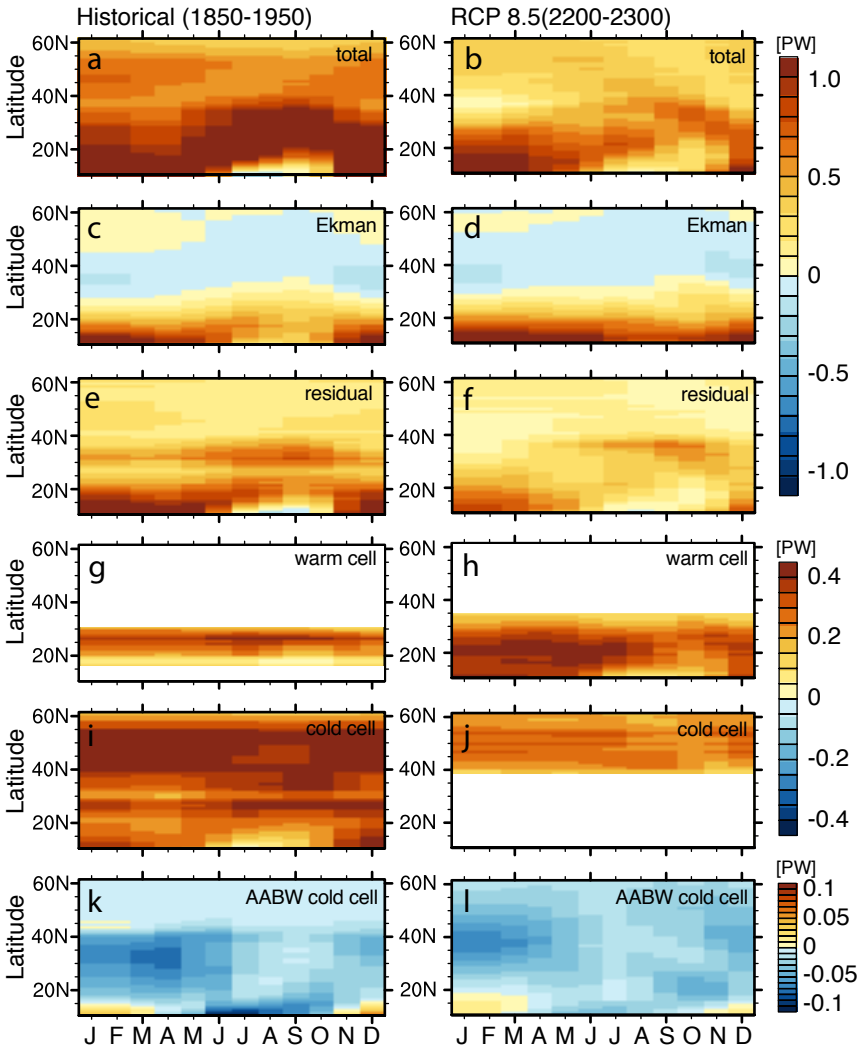

Figure 2.13: Seasonal cycle of the meridional heat transport of the individual circulation cells based on Fig.2.12 in the historical simulation (1850-1950, left column) and RCP 8.5 (2200-2300, right column). (a)-(b) Total meridional heat transport, (c)-(d) Ekman heat transport, (e)-(f) Residual/mixed circulation, (g)-(h) warm surface cell, (i)-(j) cold cell and (k)-(l) bottom cold cell of AABW. Color range in plot (a)-(f) from -1.0 to 1.0 PW with a contour interval of 0.1 PW, in (g)-(j) from -0.4 to 0.4 PW with a contour interval of 0.05 PW, and (k)-(l) from -0.1 to 0.1 PW with a contour interval of 0.01 PW.

circulation is also reduced. In RCP_{mean} the cold cell comprises most of the total OHT in the subpolar gyre (about 80%), while the residual circulation still gives the largest contribution in the tropical Atlantic and in the northern part of subtropical gyre. In the southern part of the subtropical gyre, the warm cell and the mixed circulation contribute equally to the total OHT (Fig.2.12h).

The changes in the meridional overturning circulation, the heat function and the time-mean OHT and its contributions from individual circulations show major changes in the vertical structure of the OHT in potential temperature coordinates. These changes suggest corresponding changes in the seasonal cycle of individual circulation cells that drive the changes in the total OHT seasonal cycle.

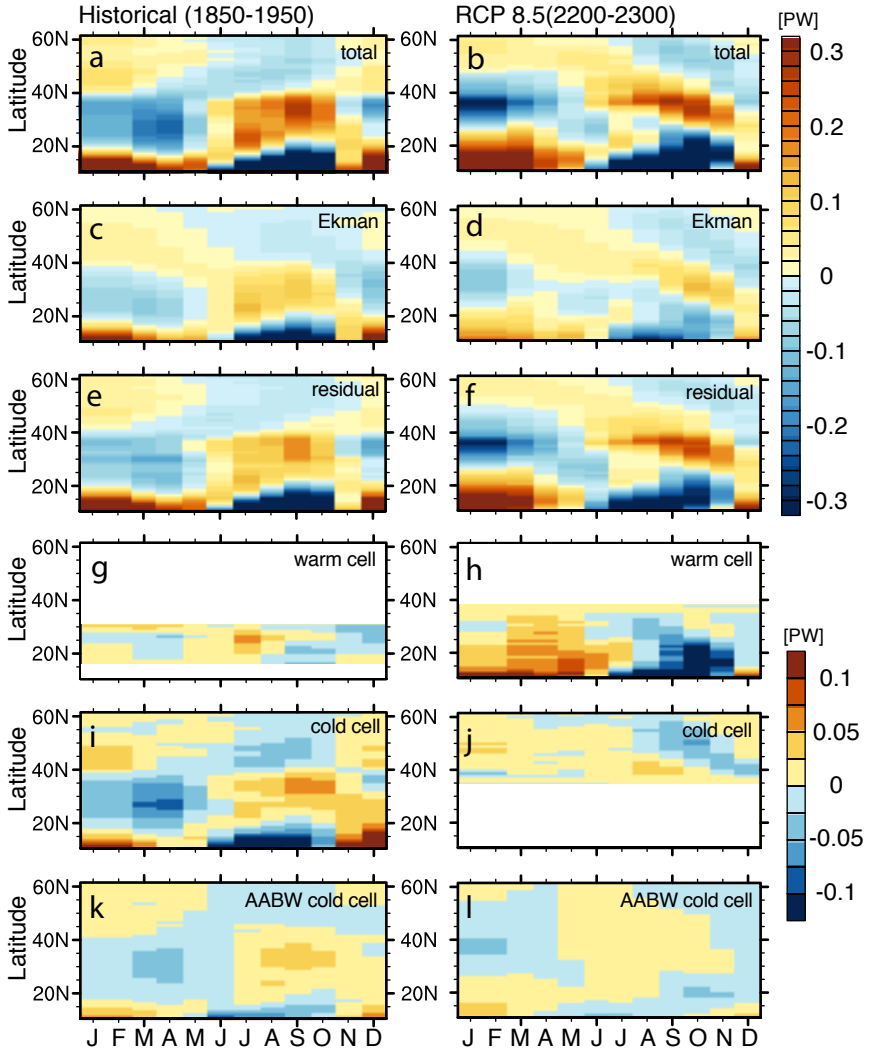

Figure 2.14: Seasonal cycle of the meridional heat transport of the individual circulation cells based on Fig.2.12 in the historical simulation (1850-1950, left column) and RCP 8.5 (2200-2300, right column). Shown are anomalies relative to the time mean heat transport at every latitude. (a)-(b) Total meridional heat transport, (c)-(d) Ekman heat transport, (e)-(f) Residual/mixed circulation, (g)-(h) warm surface cell, (i)-(j) cold cell and (k)-(l) bottom cold cell of AABW. Color range in panels (a)-(f) from -0.3 to 0.3 PW with a contour interval of 0.02 PW, in (g)-(l) from -0.1 to 0.1 PW with a contour interval of 0.025 PW.

2.2.3.3 Seasonal cycle of the individual OHT components

The changes in the vertical pathways of the OHT, in the time mean heat function and especially in the cells of the overturning stream function describe the changes in the individual contributions to the total OHT between the historical climate state and RCP8.5 climate and can describe in turn also the changes in the seasonal cycle of the individual components.
The seasonal cycles of the various circulations contributing to the total OHT are shown in Fig.2.13 for HIST_{mean} and RCP_{mean}. As shown in section 2.1 (Fig.2.5), the changes in the seasonal cycle are concealed by the mean decrease of the OHT amplitude. The OHT seasonal cycle in HIST_{mean} and RCP_{mean} (Fig.2.13a-b) reveals prominent changes that result from all of the considered circulation cells (Fig.2.13e-l), although mostly the cold cell and the residual circulation suggest to force the overall shifts in the seasonal cycle between HIST_{mean} and RCP_{mean} (Fig.2.13e-f, i-j). Obviously, the change in the latitudinal and vertical extent of the closed circulations has a direct impact on the range in the seasonal cycle covered by the individual circulations.
To emphasize the changes in the OHT seasonal cycle which are superimposed by the strong reduction of the OHT, anomalies of the seasonal cycle relative to the annual mean at every latitude are considered again in the following (Fig.2.14). The seasonal cycle of the total OHT and the Ekman heat transport (Fig.2.14a-d) reveal the same changes as shown in section 2.1 with a general northward shift in the pattern of 5 degrees and temporal shifts between one and six months.
The seasonal cycle of the residual circulation (Fig.2.14e-f) reveals a similar seasonal cycle, as well as similar shifts in the seasonal cycle from HIST_{mean} to RCP_{mean} compared to the total OHT. The seasonal cycle in the residual circulation indicates a generally weaker seasonal cycle than in the total OHT. The closed circulations generally indicate a much weaker seasonal cycle with lower seasonal amplitude (Fig.2.14g-l). In HIST_{mean} the warm cell (Fig.2.14g) covers only a small area between 15°N and 30°N and indicates a maximum in summer and a minimum in winter – similar to the

Ekman transport in the subtropical gyre, but with a smaller agreement than the residual circulation and the Ekman heat transport. In RCP_{mean} the expansion of the warm cell (Fig.2.14h) leads to an increased influence of the warm cell seasonal cycle. Following the northward shift of the total OHT and the Ekman transport the warm cell shows a similar seasonal cycle with a maximum in winter to spring and a minimum in autumn in the tropics reaching northward. In contrast to the total OHT and the Ekman heat transport, the seasonal cycle of the warm cell is almost coherent between 15°N and 35°N and significantly intensified in the seasonal amplitude in RCP_{mean}.

In $HIST_{mean}$ the seasonal cycle in the cold cell related to the NADW (Fig.2.14i) is the strongest of the three closed circulations (Fig.2.14g-l). In the tropical and subtropical North Atlantic, the seasonal cycle in the cold cell is in phase with the total OHT and the residual circulation, indicating a barotropic signal of the total heat transport reaching down to the deep cell. In the subpolar North Atlantic, the seasonal cycle of the cold cell that establishes here a significant part of the surface circulation is also in phase with the residual circulation and the total OHT. In RCP_{mean} the seasonal cycle in the NADW cold cell is restricted to the subpolar gyre and is significantly reduced. The seasonal cycle is generally shifted to later months following the phase of the residual circulation and the total OHT, but still has a low amplitude. In the AABW cold cell the seasonal cycle contributes only little to the total OHT seasonal cycle and is reduced in general from $HIST_{mean}$ to RCP_{mean}. The AABW seasonal cycle indicates a similar northward shift and weakening of the seasonal cycle pattern in the tropics and subtropics, but with the lowest seasonal amplitude in the closed circulations.

2.2.4 Summary and Conclusions

The effect of a projected reduction in the Atlantic meridional heat transport (OHT) on the seasonal cycle of the OHT calculated in potential temperature coordinates in a Coupled Model Intercomparison Project phase 5

(CMIP5) climate projection performed in the Max-Planck Institute Earth System Model (MPI-ESM) is investigated with a focus on the CMIP5 historical simulation extended with RCP8.5.

The OHT is decomposed based on a heat function in potential temperature coordinates. We can identify closed circulation cells from the Atlantic meridional overturning circulation (AMOC) in potential temperature coordinates that imply a meridional heat transport and allow a distinct physical interpretation of the processes related to the respective closed circulations of the warm wind-driven surface circulation, two cold circulations related to the North Atlantic Deep Water (NADW) and the Antarctic Bottom Water (AABW). The residual to the total OHT yields a residual/mixed circulation with the influence of both, effects of the wind and of the deep overturning.

The decomposition of the OHT based on the overturning stream function and the heat function in potential temperature coordinates (Ferrari and Ferreira, 2011) allows to understand changes in the vertical structure of the OHT. The overall warming of North Atlantic ocean temperatures leads to a shift of the overturning cell in temperature coordinates to warmer layers of potential temperature. The heat transport is driven by a warm cell in the subtropical gyre that expands in meridional direction in RCP_{mean}, and a cold cell that spans the whole North Atlantic in HIST_{mean}, but weakens and shrinks in RCP_{mean} due to a reduction in the formation of the NADW. The warm cell at the surface is thought to be wind driven, while the deep cold cell is associated with the formation of NADW (Ferrari and Ferreira, 2011). Most of the heat transport is accomplished by the mixed or residual circulation in both HIST_{mean} and RCP_{mean} in agreement with Ferrari and Ferreira (2011). The residual circulation represents the combined effect of the wind-driven circulation and the deep overturning, that cannot be discriminated explicitly. The AABW cold cell contribution can be neglected for the mean OHT.

The analysis of the OHT based on the heat function reveals changes in agreement with those found in section 2.1. A similar distribution of the OHT in terms of the heat functions is found in the seasonal cycle. The OHT reveals a northward shift by about 5° and temporal shifts of 1-6 months in the seasonal cycle in concert with the shift in the Ekman heat transport seasonal cycle.

The warm cell only contributes in the subtropical gyre, where the seasonal cy-

cle reveals an increased seasonal amplitude from HIST_{mean} to RCP_{mean}. The seasonal cycle in the cold cell contributes in HIST_{mean}, but is mostly absent in RCP_{mean} in the subtropical gyre. In agreement with the time mean OHT, the seasonal cycle is predominately driven by the residual circulation. Consequently, the changes seen in the seasonal cycle of the OHT can be related to changes in the wind-driven circulation of the warm cell and to changes in the formation of NADW in the cold cell, but the major changes appear in the residual circulation that does not allow a clear separation of wind-driven effects and effects of changes in the North Atlantic density field. Clear mechanisms cannot be identified due to the mixed character of the residual circulation the is driven by both, shallow the wind driven circulation and the deep overturning. The AABW related cold circulation generally indicates a weak seasonal cycle, but also shifts from the historical simulation to RCP8.5 which might be associated with changes in the dynamics in the Southern Ocean. Thus, a combined effect the wind forcing and the deep overturning mainly leads to the changes seen in the OHT seasonal cycle.

Despite the physical insight obtained from the OHT in potential temperature coordinates, this decomposition is not considered further in the following analysis for practical reasons. The decomposition of the OHT based on the heat function demands for the knowledge and analysis of the full overturning cell. For the analysis of the predictability in chapter 4, the cells of the overturning circulation have to be identified in individual ensemble members of the hindcast experiments together with the control simulations. The structure of the closed overturning cells and the heat function have to be evaluated individually, but might differ for the ensemble members, which leads to additional uncertainties in the prediction. Further, such a decomposition can hardly be obtained from observations so that the use and applicability of the heat function, e.g. in an operational prediction system, might be dubious.

3 Near-term changes in the seasonal cycle of the Atlantic meridional heat transport and the Atlantic meridional overturning circulation

3.1 Introduction

Changes in the seasonal cycle of the Atlantic meridional heat transport in the long term until the end of the 23rd century presented in section 2.1 result from a continous increase of surface temperatures and in concert with a gradual decrease in the AMOC and the OHT starting in the 20th century of the historical simulation. As a prerequisite for the predictability analysis in section 4, I here repeat and extend parts of the analysis of chapter 2.1 for near future changes in the OHT seasonal cycle and for near future changes in the AMOC seasonal cycle in the MPI-ESM CMIP5 climate projections until the middle of the 21st century. I aim to find imprints of global warming on the OHT seasonal cycle in RCP8.5 and additionally in RCP4.5 not only on centennial time scales, but also on shorter decadal time scales in MPI-ESM.

In the middle of 21st century, North Atlantic SSTs are projected to increase between about 0.5°C in RCP2.6 to about 2°C in RCP8.5 until 2100 in the

CMIP5 multimodel ensemble (e.g. IPCC, 2013, Villarini and Vecchi, 2012). Until 2050, the RCP8.5 scenario in MPI-ESM indicates a global mean temperature increase by more than 2°C and a reduction in the AMOC and OHT by 10-20% compared to the historical simulation. Similarly, the RCP4.5 scenario indicates a global temperature increase of almost 2°C and a reduction of the AMOC and OHT by about 10%. Following the CMIP5 specifications, the RCP scenarios do not diverge much in the global response to climate changes until about 2035 (e.g., Meehl et al., 2012) and are still close to each other until the middle of the 21st century. Thus, comparable changes for the OHT and AMOC seasonal cycle can be expected in RCP4.5 and RCP8.5 until the middle of the 21st century.

3.2 Methods

Following section 2.1, the analysis of short term changes in the OHT seasonal cycle is based on the decomposition of the OHT into overturning and gyre component (Eq. 2.4, $\mathbf{H} \approx \mathbf{H}^{ov} + \mathbf{H}^{gyre}$). Additionally, I analyze changes in the seasonal cycle in the AMOC, that is considered here as the maximum of the stream function ψ given by $\psi(y,z) = \int_z^0 \int_{x_W}^{x_E} v(x,y,z)\ dx\ dz$, the Ekman transport ψ_{ek} given by $\psi_{ek} = -\frac{1}{\rho_0 f} \int_{x_W}^{x_E} \tau_x\ dx$ with τ_x the zonal wind stress at the ocean surface, and the geostrophic contribution to the AMOC ψ_{geo} which is approximated here by the AMOC with the Ekman transport removed from it (AMOC-Ekman): $\psi_{geo} \approx \psi - \psi_{ek}$.

For the analysis, I consider anomalies of the seasonal cycle relative to the time-mean AMOC and OHT at every latitude. The seasonal anomalies are considered for the present climate state in the CMIP5 historical simulation (1850-1950, HIST_{mean}) and for the middle of the 21st century in RCP4.5 and RCP8.5 (2045-2075).

Additionally, I look at latitude-dependent changes in the peak-to-peak amplitude of the seasonal cycles of AMOC and OHT over the considered periods.

The peak-to-peak amplitude is defined here by the difference between the maximum and the minimum of the seasonal cycle depending on latitude. Further, latitude-dependent temporal shifts in the minima and maxima in the seasonal cycles of the AMOC and OHT and their components are analyzed, that give the shift in months for the respective minima and maxima at every latitude.

3.3 Changes in the seasonal cycle of the AMOC and the OHT until the middle of the 21st century

The AMOC and the OHT seasonal cycles and its components reveal changes with shifts in space and time until the middle of the 21st century in both the RCP4.5 and the RCP8.5 scenario (Fig.3.1,3.2). Until the middle of the 21st century, the changes in the AMOC seasonal cycle are roughly comparable between RCP4.5 and RCP8.5 (Fig.3.1a-c). Both scenarios indicate on average a slight northward shift of the maximum westerlies at the surface, whereas no significant expansion of the Hadley cell is found in the time mean (not shown). But during summer and winter a noticeable poleward expansion of the Hadley cell by about one to two degrees and a poleward shift of the jet emerges (not shown). The AMOC seasonal cycle indicates a slight northward shift of the pattern which is easily visible in the maximum in winter and the minimum in summer in RCP4.5 and RCP8.5 in the tropical North Atlantic (Fig.3.1a-c). In addition to the northward shift, single latitudes indicate changes in the peak-to-peak amplitude and temporal shifts. The decomposition of the AMOC into geostrophic transport and Ekman transport (Fig. 3.1d-i) reveals that the Ekman transport largely contributes to the changes in the AMOC seasonal cycle.

Similar to the AMOC seasonal cycle, the changes in the total OHT seasonal cycle are comparable between RCP4.5 and RCP8.5 until the middle of the 21st century (Fig.3.2a-c). Following the northward shift in the atmo-

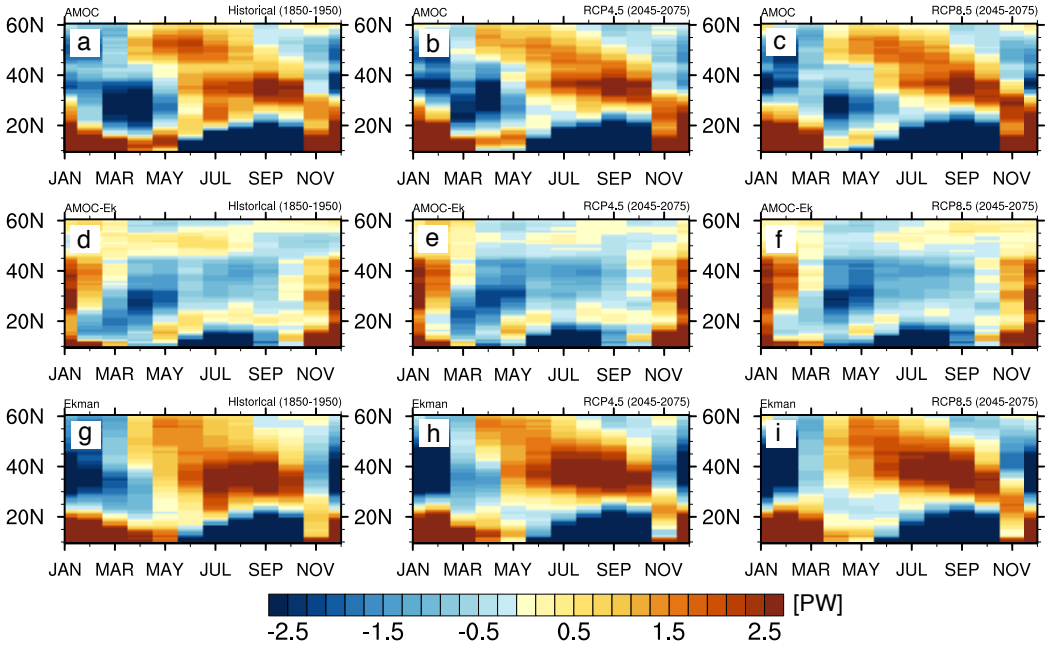

Figure 3.1: Change in the **(a-c)** AMOC, **(d-f)** geostrophic volume transport and **(g-i)** the Ekman transport seasonal cycle from the historical simulation (1850-1950, left panels) to RCP4.5 (2045-2075, middle panels) and RCP8.5 (2045-2075, right panels). Shown are anomalies relative to the annual mean at every latitude. Contour interval: $0.02PW$.

spheric circulation, the Ekman heat transport (not shown) and the associated overturning heat transport (Fig.3.2d-f) indicate a northward shift of the seasonal cycle pattern in RCP4.5 and RCP8.5. The overturning heat transport (Fig.3.2g-i) reveals changes in space and time for both scenarios RCP4.5 and RCP8.5 until the middle of the 21st century, while changes in the gyre heat transport seasonal cycle are rather small (Fig.3.2d-f).

As examples, the seasonal cycle of the total OHT, the overturning heat transport and the gyre heat transport are shown for 26°N, 41°N and 50°N (Fig.3.3). The seasonal cycle at 26°N reveals prominent changes which are comparable for the total OHT and the overturning heat transport in RCP4.5 and RCP8.5. The seasonal cycle in overturning heat transport the OHT seasonal cycle and its changes at 26°N. The seasonal cycle in the gyre heat transport is weak, changes are small and of minor importance to the total OHT seasonal cycle. At 41°N, the OHT seasonal cycle and its changes are similarly driven by the overturning heat transport seasonal cycle with similar changes in RCP4.5 and RCP8.5. The seasonal cycle of the gyre heat transport indicates larger

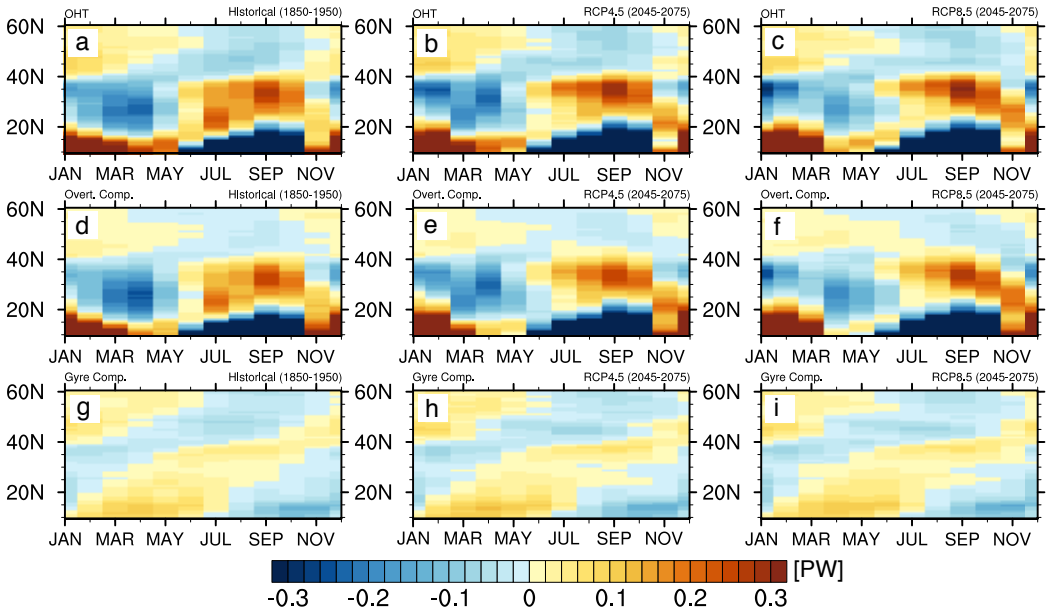

Figure 3.2: Change in the **(a-c)** total meridional heat transport, **(d-f)** overturning heat transport and **(g-i)** gyre heat transport seasonal cycle from the historical simulation (1850-1950, left panels) to RCP4.5 (2045-2075, middle panels) and RCP8.5 (2045-2075, right panels). Shown are anomalies relative to the annual mean at every latitude. Contour interval: $0.02PW$.

changes than those at 26°N, but still, the overturning heat transport dominates the temporal shift in the OHT seasonal cycle.

At 50°N, the OHT seasonal cycle indicates fewer changes from the historical simulation to the RCP scenarios. The influence of the overturning heat transport seasonal cycle on the total OHT seasonal cycle reduces at 50°N, whereas the influence of the gyre heat transport seasonal cycle on the total OHT seasonal cycle increases compared to subtropical latitudes. Changes from the present climate state in HIST_{mean} to RCP4.5 and RCP8.5 are similarly driven by the gyre heat transport.

To further understand the changes in the AMOC and OHT seasonal cycle, the latitude-dependent peak-to-peak amplitude that is the difference between minimum and maximum in the seasonal cycle, as well as the latitude-dependent temporal shift in the seasonal minima and maxima giving the respective temporal shift in months are analyzed (Fig.3.4-3.7).

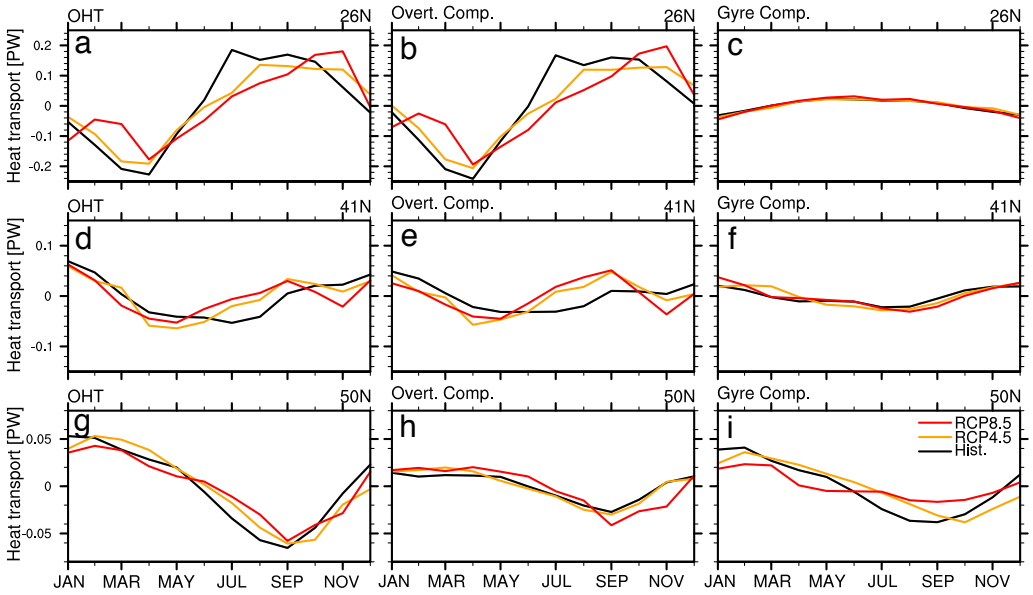

Figure 3.3: Change in the OHT seasonal cycle: **(a-c)** 26°N total OHT, overturning and gyre heat transport. **(d-f)** 41°N total OHT, overturning and gyre heat transport. **(g-i)** 50°N total OHT, overturning and gyre heat transport. For the historical simulation (1850-1950, black), RCP4.5 (2045-2075, yellow) and RCP8.5 (2045-2075, red). Shown are anomalies relative to the annual mean at every latitude.

3.3.1 Seasonal peak-to-peak amplitude

The seasonal peak-to-peak amplitude of the AMOC indicates – as seen in Fig. 3.1 – the strongest seasonal cycle in the tropical North Atlantic with peak-to-peak amplitudes of more than 20 Sv in the historical simulation, RCP4.5 and RCP8.5 (Fig.3.4a). Between the historical simulation and RCP4.5 and RCP8.5, the AMOC seasonal amplitude shows comparable changes in both scenarios: a slight increase in the amplitude in the tropics, a general decrease in the subtropical gyre between 25°N and 35°N, an increase between 20°N and 25°N and between 35°N and 45°N and a general decrease in the subpolar gyre north of 45°N. In particular between 25°N and about 35°N, the AMOC seasonal amplitude is reduced between HIST_{mean}, RCP4.5 and RCP8.5 by about 0.5 Sv and 1 Sv, respectively. At around 20 °N and 42°N, the AMOC seasonal amplitude shows a considerable increase of more than 1.5 Sv in RCP4.5 and RCP8.5. Between 45°N and roughly 60°N, the AMOC indicates a rather spatially uniform weakening in the seasonal amplitude by about 0.5 Sv to 1 Sv in RCP4.5 and RCP8.5.

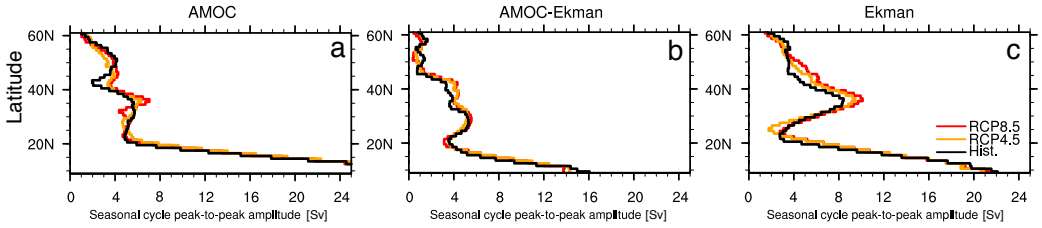

Figure 3.4: Peak-to-peak amplitude [in Sv] of the AMOC seasonal cycle of **(a)** the AMOC, **(b)** the geostrophic volume transport and **(c)** the Ekman transport for the historical simulation (1850-1950, black), RCP4.5 (2045-2075, yellow) and RCP8.5 (2045-2075, red).

The geostrophic transport (≈AMOC-Ekman) also shows a strong seasonal peak-to-peak amplitude in the tropics that decreases northwards in HIST_{mean} (Fig.3.4b). The changes in the seasonal amplitude also indicate similar changes in RCP4.5 and RCP8.5: a general decrease in the southern part of the subtropical gyre (20°N-30°N), an increase in the seasonal amplitude in the northern subtropical gyre and the subpolar gyre north of 30°N to about 50°N, and an overall decrease north of 50°N compared to HIST_{mean}.

The Ekman transport seasonal peak-to-peak amplitude (Fig.3.4c) again shows a similar change from the historical simulation to RCP4.5 and RCP8.5 at all latitudes. The seasonal amplitude is increased between 15°N to about 22°N, decreased between 22°N and 35°N, and increased north of 35°N to about 55°N. Obviously, the seasonal amplitude is strongly reduced around 25°N by about 1 Sv in RCP4.5 and increased by 1-2 Sv between 35°N to 50°N.

The seasonal peak-to-peak amplitude of the OHT indicates, similarly to the AMOC, the strongest seasonal cycle in the tropical North Atlantic that declines poleward. For the OHT, the peak-to-peak amplitude changes comparably to the AMOC in the subtropical gyre. The OHT seasonal amplitude shows a general decrease in the subtropical gyre between 20°N to 30°N and an increase between 30°N and 40°N from HIST_{mean} to RCP4.5 and RCP8.5 (Fig.3.5a,d). The increase seems to be somewhat larger in RCP8.5 than in RCP4.5 and is also present in the tropical North Atlantic. A similar behavior of the peak-to-peak amplitude is found for the overturning heat transport (Fig.3.5b,e). The gyre heat transport indicates

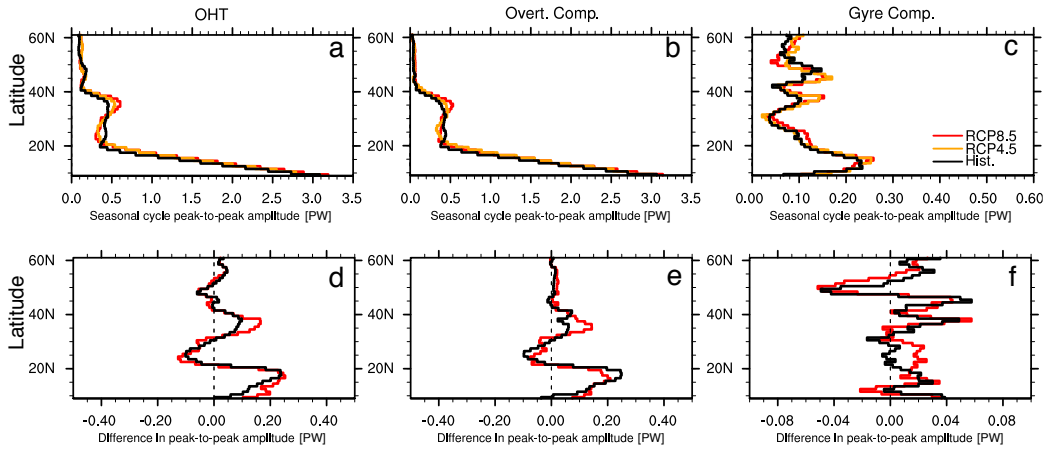

Figure 3.5: Peak-to-peak amplitude [in PW] of the OHT seasonal cycle of **(a)** total OHT, **(b)** overturning heat transport and **(c)** gyre heat transport for the historical simulation (1850-1950, black), RCP4.5 (2045-2075, yellow) and RCP8.5 (2045-2075, red). **(d-f)**: Difference in the peak-to-peak amplitude in RCP4.5 minus the historical simulation (black) and RCP8.5 minus the historical simulation (red) for **(d)** the total OHT, **(e)** overturning heat transport and **(f)** the gyre heat transport.

a weaker seasonal amplitude that is fluctuating around 0.1PW in the subtropical and subpolar gyre for the present and future climate. The changes in the seasonal peak-to-peak amplitude from the historical period to RCP4.5 and RCP8.5 are significantly smaller than in the overturning heat transport, but still show, that in RCP4.5 an increase in the seasonal amplitude is mostly limited to latitudes north of 35°N. At about 50°N, the seasonal amplitude is reduced in the subpolar gyre in RCP4.5 and RCP8.5. Changes in the seasonal peak-to-peak amplitude of the OHT are comparable between to the overturning heat transport in the subtropical gyre and are comparable to the gyre heat transport in the subpolar gyre, suggesting a similar partitioning of changes in the seasonal peak-to-peak amplitude as for the time mean OHT.

The variance of the seasonal cycle (not shown) generally shows changes comparable to the peak-to-peak amplitude in the AMOC and the OHT (Fig.3.4 and 3.5) from the historical simulation to RCP4.5 and RCP8.5. The variance of the AMOC seasonal cycle is decreased between 20°N and 35°N in RCP4.5 and RCP8.5, the variance is increased between 35°N and 50°N in RCP4.5 and RCP8.5, whereas north of 50°N, the variance is again decreased in RCP4.5 and RCP8.5. The variance of the geostrophic transport seasonal

cycle is decreased between 15°N and 25°N in RCP4.5 and RCP8.5, the variance is increased between 25°N and about 50°N in RCP4.5 and RCP8.5, whereas between about 50°N and 55°N, the variance is again decreased in RCP4.5 and RCP8.5. The variance of the Ekman transport seasonal cycle is decreased between about 20°N and 35°N in RCP4.5 and RCP8.5, the variance is increased between 35°N and about 55°N in RCP4.5 and RCP8.5, whereas north of 55°N, the variance is again decreased in RCP4.5 and RCP8.5.
The variance of the OHT seasonal cycle also reveals comparable changes to the peak-to-peak amplitude. The OHT and overturning heat transport show a decrease in the variance between 20°N and 30°N, an increase in the variance between 30°N and 40°N and smaller changes in the subpolar gyre. The gyre heat transport reveals an increase mostly between 35°N and 45°N and north of 50°N, while the variance is decreased between 45°N and 50°N.

3.3.2 Temporal shift in the seasonal minima and maxima

In addition to changes in the peak-to-peak amplitude of the seasonal cycle, the AMOC seasonal cycle reveals changes in the temporal structure reflected by latitude-dependent temporal shifts in the seasonal minima and maxima (Fig.3.6). The AMOC shows relatively little changes in its seasonal maximum from the historical simulation to RCP4.5 and RCP8.5 (Fig.3.6a). Between 25°N and 28°N, a temporal shift of 5 months and 4 months is found in RCP4.5 and RCP8.5, respectively. Further, the seasonal cycle of the AMOC is shifted in the northern subpolar gyre by 2 months in RCP4.5 and by 1 month at single latitudes. The AMOC's seasonal minimum (Fig.3.6b) on the other hand reveals several changes in the subtropical and subpolar gyre. The minimum has a temporal shift of 5 months at about 20°N, about 5 degrees further south than for the maximum, for both RCP4.5 and RCP8.5. In the northern subtropical gyre between about 35°N and 40°N, the minimum is shifted by 1 to 4 months. The subpolar gyre shows a shift of up to 2 months between 40°N and 50°N and up to 1 months between 50°N and 55°N. Between 55°N and 60°N, the minimum is shifted by 6 months in RCP4.5. From Fig.3.1

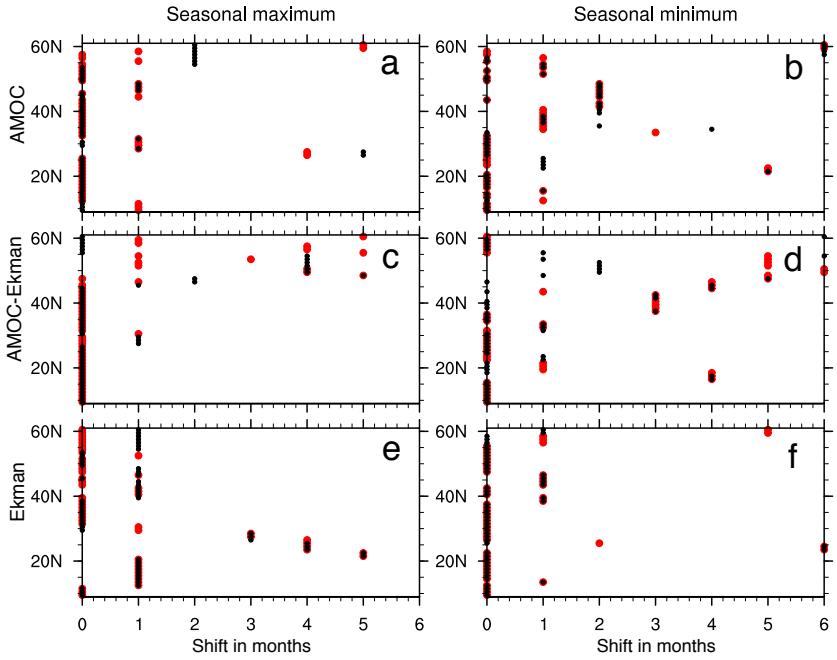

Figure 3.6: Temporal shift of the AMOC seasonal cycle (in months) of **(a-b)**: AMOC for the seasonal maximum (a) and the seasonal minimum (b). **(c-d)**: the geostrophic volume transport for the seasonal maximum (c) and the seasonal minimum (d). **(e-f)**: the Ekman transport for the seasonal maximum (e) and the seasonal minimum (f). The temporal shift in months from the historical simulation (1850-1950) to RCP4.5 (2045-2075) in black and from the historical simulation to RCP8.5 (2045-2075) in red.

follows, that this does not involve a total phase reversal of the seasonal cycle, but rather a shift of the minimum only.

The geostrophic transport (Fig.3.6c) shows a shift of the maximum mainly in the subpolar gyre in RCP4.5 and RCP8.5 between 1 to 5 months between 45°N and 55°N. The minimum (Fig.3.6d) by contrast shows manifold temporal shifts in the subtropical and subpolar gyre. In the southern subtropical gyre, the seasonal cycle minimum is shifted by 1 months at some individual latitudes, whereas in the northern subtropical gyre (30°N-40°N), the minimum is shifted by up to 3 months in RCP4.5 and RCP8.5. The subpolar gyre shows shifts in the minimum of up to 6 months between 40°N and 55°N, while such large shifts occur only at individual latitudes.

The Ekman transport seasonal maximum (Fig.3.6e) is mainly shifted between 20°N and 28°N with shifts between 3 to 5 months. In the subpolar gyre, the maximum is shifted by only 1 month between 40°N to 50°N and about 55°N to 60°N. The Ekman minimum (Fig.3.6f) indicates only little changes, while

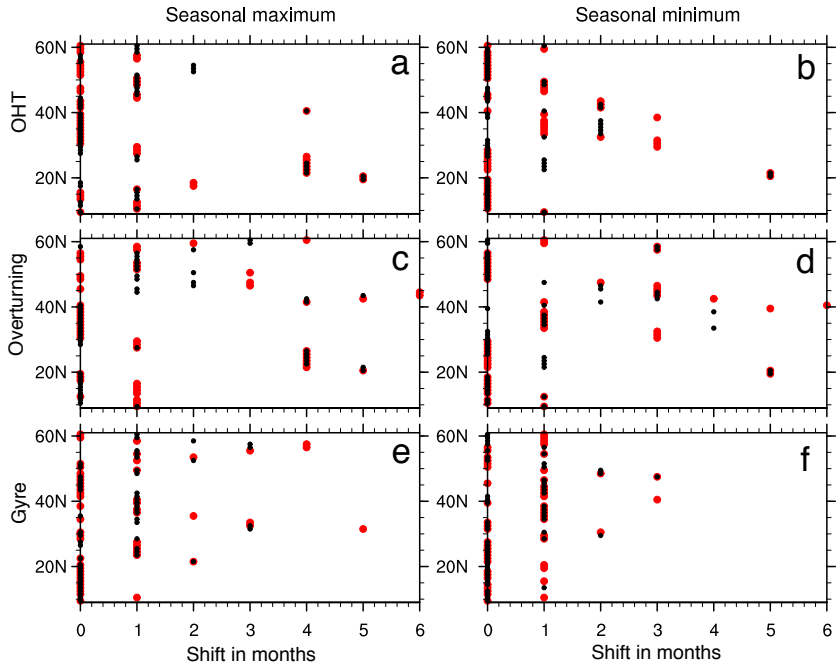

Figure 3.7: Temporal shift of the OHT seasonal cycle (in months) of **(a-b)**: total OHT for the seasonal maximum (a) and the seasonal minimum (b). **(c-d)**: the overturning heat transport for the seasonal maximum (c) and the seasonal minimum (d). **(e-f)**: the gyre heat transport for the seasonal maximum (e) and the seasonal minimum (f). The temporal shift in months from the historical simulation (1850-1950) to RCP4.5 (2045-2075) in black and from the historical simulation to RCP8.5 (2045-2075) in red.

at about 23°N a shift of 6 months is found. The shift of the seasonal maximum and minimum at about 20°N reflects the northward shift of the tropical pattern following the northward shift of the wind stress.

The OHT seasonal cycle minima and maxima show latitude dependent shifts of 1 to 5 months. Intense shifts of 5 months occur only in small latitude bands. At most latitudes, there is either no shift or the shift is in the order of 1 to 2 months. For the OHT the seasonal cycle maximum (Fig.3.7a), the strongest shift of 4 to 5 months is found between 20°N and 30°N. Further, a shift of 4 months occurs at the gyre boundary at about 40°N and a shift of 1 to 2 months occurs in the SPG. The minimum also shows a 5 months shift at 20°N (Fig.3.7b), but smaller shift of 1 to 2 months in the rest of the subtropical gyre. Further, the minimum shows temporal shift of 2 months between 35°N-45°N.

The seasonal cycle of the overturning heat transport indicates a similar shift

in the seasonal maxima in the subtropical North Atlantic with shifts of 4 to 5 months between 20°N-30°N and 1 to 3 months in the subpolar gyre (Fig.3.7c). The minimum is also shifted by 1 to 4 months in the subpolar gyre with prominent changes between 40°N and 45°N (Fig.3.7d). In the subpolar gyre the temporal shift of the minima and maxima is even larger than for the OHT with a shift in the minimum up to 3 months at . The seasonal cycle of the gyre heat transport shows generally smaller temporal shifts limited to 3 months at about 35°N and 55°N for the seasonal maximum and at 50°N for the seasonal minimum. Overall, the OHT seasonal cycle is considerably shifted between 20°N to 25°N and 35°N to 45°N. The overturning heat transport is mainly shifted between 20°N and 30°N and roughly between 40°N and 60°N. The gyre heat transport seasonal cycle reveals the overall smallest shifts.

3.4 Summary

Compared to the longterm changes in RCP8.5 (section 2.1) similar albeit less intense changes in the seasonal cycle pattern of the OHT can already be identified in the middle of the 21st century in RCP4.5 and RCP8.5. Further, the AMOC also reveals latitude-dependent changes its seasonal cycle.
The AMOC shows a general decrease in the seasonal peak-to-peak amplitude in the subtropical gyre and large parts of the subpolar gyre. The large decrease in the seasonal amplitude appears in the subtropical gyre at about 25°-30°N similar to the latitudes where the maximum is strongly shifted. In the subpolar gyre, the geostrophic transport indicates temporal shifts that might be evidence of changes in the AMOC seasonal cycle, especially in the seasonal minimum. The changes in the Ekman transport seasonal cycle are rather small and mainly project on the AMOC seasonal cycle at southern latitudes of the subtropical gyre.
The OHT, the overturning heat transport and the gyre heat transport also reveal changes depending on latitude. The overturning heat transport seasonal cycle shows that changes in the seasonal amplitude are prominent in the subtropical gyre, influencing the OHT seasonal cycle here. Coupled to

this, changes in the variance of the seasonal cycle of the overturning heat transport are pronounced in the subtropical gyre, indicating changes in the seasonal variability. Mostly between 20°N and about 40°N, the overturning heat transport controls the temporal shift in the OHT seasonal cycle. The seasonal minima and maxima show shifts in the STG and SPG. The gyre heat transport influences changes in the OHT seasonal cycle mostly in the subpolar gyre, where the seasonal variability of the gyre heat transport dominates the seasonal amplitude of the OHT and temporal shifts of up to 3 months occur mostly between 50°N-60°N.

Overall, in agreement with the longterm changes in the OHT seasonal cycle, the changes in the amplitude are mostly due to the overturning heat transport seasonal cycle in the subtropical gyre and due to the gyre heat transport in the subpolar gyre. But shifts in the seasonal minima and maxima appear in the overturning heat transport predominantly in the subpolar gyre. This suggests that prominent changes in the dynamics of the seasonal cycle in both the atmospheric contribution and the oceanic contributions are already noticeable in the 21st century and intensify continuously until the end of the 23rd century in the model simulation.

The comparison of changes in the AMOC and OHT seasonal cycles indicates that a direct transfer of changes in the AMOC seasonal cycle on changes in the OHT seasonal cycle is not obvious, although changes in the seasonal amplitude are comparable in the subtropical gyre. Temporal shifts, as well as changes in the seasonal peak-to-peak amplitude differ between the AMOC and the OHT depending on latitude.

3.5 Conclusions

Both, the AMOC and the OHT with all their contributions reveal noticeable changes in the seasonal cycle from the historical simulation to RCP4.5 and to RCP8.5.

- The changes in the seasonal cycle give rise to expect changes in the predictability of the AMOC and the OHT – if these depend on changes

in the variability – especially at latitudes with outstanding temporal shifts and changes in the peak-to-peak amplitude.

- In particular between 25°N and 35°N in the subtropical gyre, at about 40°N and north of 50°N in the subpolar gyre, the changes in the peak-to-peak amplitude and the temporal shifts of the seasonal minima and maxima motivate to expect considerable changes in the predictability of the AMOC in a future climate state.

- Accordingly, around 25°N, 30°N to 40°N in the subtropical gyre and between 40°N and 60°N in the subpolar gyre, the identified changes in the OHT seasonal cycle hint to changes in the predictability of the OHT in a future climate state.

In particular, the predictability could be influenced at latitudes showing a reduction in the peak-to-peak amplitude and the variance of the seasonal cycle what might lead to a reduction in the predictability. But how the predictability changes at these specific latitudes and how a changed seasonal cycle influences the predictability of the AMOC and the OHT for yearly and also for multiyear seasonal means – as winter or summer means – is unclear and will be investigated in the following chapter.

4 Potential predictability of the North Atlantic ocean circulation in the present and future climate

4.1 Introduction

Near-term climate predictions on seasonal to decadal time scales are of growing interest, not only in the scientific community, but also for stakeholders, policy makers and decision makers who depend on reliable climate predictions for appropriate decisions. But the field of decadal climate predictions is still relatively novel and rapidly evolving (e.g., Goddard et al., 2012).
Under global warming, the North Atlantic climate is projected to change with increased surface temperatures and changes in the circulation of the atmosphere and the ocean. Together with global warming, the seasonal cycle of surface temperatures (Dwyer et al., 2012), in the arctic ocean (Carton et al., 2015) and also of the Atlantic meridional overturning circulation (AMOC) and meridional heat transport (OHT) (Chapter 2 and 3) is projected to change. Whether global warming and especially the changes in the seasonal cycle impact the predictability is mostly unknown. Boer (2009) found a decrease in the potential (decadal) predictability of surface temperatures and precipitation and Tietsche et al. (2013) found a reduction in skill

of Arctic sea ice predictions under global warming. However, whether global warming affects the predictability of the AMOC and the OHT has not yet been investigated. Here I investigate changes in the potential predictability of the AMOC and the OHT between a present climate state based on the CMIP5 historical simulation and a future climate state in the middle of the 21st century based on RCP4.5.

The North Atlantic Ocean plays a fundamental role in the North Atlantic climate and its variability and has been shown to impact the European and North American climate (e.g., Sutton and Hodson, 2005, Knight et al., 2005, Pohlmann et al., 2006). Thus, the key role of the North Atlantic motivates to advance the understanding of the North Atlantic climate predictability, even though the specific role of the North Atlantic Ocean is still controversially discussed (e.g., Riser and Lozier, 2013).
In context of the recent coordinated effort of the Coupled Model Intercomparison Project Phase 5 (CMIP5, Taylor et al., 2012) as part of the fifth assessment report of the Intergovernmental Panel on Climate Change (IPCC), decadal climate predictions have been investigated in a multi-model framework based on a large ensemble of coupled climate model simulations. The analysis of predictability relies on retrospective ensemble forecast experiments, so-called ensemble hindcast experiments. Studies in the context of CMIP5 mostly focussed on the analysis of the predictability under historical climate conditions that represent the climate state of the last half century from 1960 to the beginning of the 21st century (Meehl et al., 2009).
Predictability on decadal scales has been found for a number of climate variables, such as air and sea surface temperatures (e.g., Pohlmann et al., 2009, van Oldenborgh et al., 2012), the North Atlantic subpolar gyre (e.g., Matei et al., 2012b, Yeager et al., 2012, Robson et al., 2012), the AMOC (e.g., Collins et al., 2006, Msadek et al., 2010, Matei et al., 2012a, Pohlmann et al., 2013b) and OHT (e.g., Tiedje et al., 2012) and is assessed in either potential predictability or actual forecast skill.
Most predictability studies have focussed on the analysis of multi-year means. However, climate variables as well as the underlying mechanisms change seasonally in space and time and thus, the predictability might vary between

different seasons. Müller et al. (2012) and MacLeod et al. (2012) analyzed the predictive skill of multiyear seasonal means of surface air temperatures and precipitation. MacLeod et al. (2012) found that yearly means yield higher skill than multiyear seasonal means. Yet, the predictability of multiyear seasonal means has not been examined for the AMOC and the OHT and might give valuable insights concerning the impact of changes in the seasonal cycle on the predictability.

Forecast skill in these experiments is usually assessed from metrics like the root-mean-square error (RMSE), anomaly correlation coefficient (ACC) or the ensemble spread and for the skill of initialized prediction experiments compared to uninitialized predictions (Collins, 2002, Collins and Allen, 2002, Collins and Sinha, 2003, Pohlmann et al., 2004, Msadek et al., 2010). By the direct comparison of uninitialized and initialized predictions in terms of skill scores, areas emerge where initialization increases the skill (e.g., Meehl et al., 2014).

Considering the process of decision making, predictions need to be skillful and additionally reliable – meaning that predictions might have a value for the decision making process (Corti et al., 2012). A reliable forecast implies, that the forecast probabilities for one specific event match the observed frequencies for that specific event. In other words, if a prediction is unreliable, the information obtained from the prediction might be misleading and causes inappropriate decisions.

Reliability is traditionally assessed in weather forecasts or seasonal predictions for a specific event that could be the temperature or precipitation above a certain threshold (e.g., Palmer et al., 2008, Weisheimer and Palmer, 2014). Recently, the reliable of decadal predictions was investigated for the first time, showing that for some regions reliable decadal predictions are possible for surface temperatures, even though the reliability is significantly reduced when the trend is removed from the ensemble (Corti et al., 2012).

Decadal predictions are still in an early stage (Goddard et al., 2013), even though a lot of progress and success was achieved from CMIP5 (e.g., Meehl et al., 2014). So far, decadal prediction studies mostly focussed on the historical climate state, but studies invoking the effects of climate change on the decadal predictability do not exist to my knowledge, except of the study of

Boer (2009) and Tietsche et al. (2013). As shown in the previous chapters 2 and 3, global climate change impacts the mean state, the variability and the seasonal cycle of the AMOC and the OHT on long time scales (until the end of the 23rd century) and even on shorter time scales until the middle of the 21st century. Latitude-dependent, significant changes occur until the middle of the 21st century with changes in the seasonal amplitude and in the seasonal variability (chapter 3), which might induce changes in the predictability of the AMOC and OHT from the present to a future climate state. From these changes found in chapter 3, the following questions concerning the predictability of the AMOC and OHT arise:

1. Does the potential predictability of the AMOC and the OHT change between the present climate state and a projected future climate state in the middle of the 21st century?

2. If so, does the decadal predictability of the AMOC and the OHT change predominately at those latitudes where the largest changes are found in the seasonal cycle?

3. How does the decadal predictability change in multiyear seasonal means? Do specific seasons indicate a stronger influence of global warming than others and thus impact the predictability of yearly means?

To answer these issues, I use ensemble prediction experiments with the Max-Planck-Insitute Earth system model and analyze the potential predictability of the AMOC and the OHT for a present and a future climate state. The predictability analysis is based on the CMIP5 historical simulation and the RCP4.5 scenario in MPI-ESM. The ensemble experiment for the present climate state (HIST_{ens}) extends from 1995 to 2023, using 20 start years with 10 ensemble member per start year. For the experiment HIST_{ens}, the historical simulation is extended with the RCP4.5 scenario after 2005. An equivalent ensemble experiment is performed for the future climate state in RCP4.5 (RCP_{ens}), between 2045 and 2073. In these experiments, the potential pre-

dictability of the AMOC and OHT is analyzed for yearly means and for multi-year seasonal means. The analysis is conducted using the anomaly correlation coefficient (ACC) as deterministic predictability measure, and reliability diagrams in combination with the Brier Skill Score (BSS) as a probabilistic predictability measure in HIST_{ens} and RCP_{ens}.

4.2 Methods

4.2.1 Model and ensemble generation

The study is based on two ensemble prediction experiments integrated in the coupled MPI Earth System Model (MPI-ESM; Jungclaus et al., 2013, Stevens et al., 2013). Since decadal climate predictions are known to be sensitive to perturbations in the initial conditions, a number of methodologies have been applied (e.g., Baehr and Piontek, 2013, and references therein). In this study, I initialize the ensemble with breeding of the ocean component of MPI-ESM to generate optimal perturbations.

To analyze the potential predictability in the North Atlantic, I use CMIP5 experiments (Taylor et al., 2012) performed in MPI-ESM at low resolution. The atmospheric model (ECHAM6) is run with a resolution of T63 and 47 vertical levels. The ocean component (MPIOM) is run with an average horizontal resolution of about 1.5° and 40 vertical levels.

The initial conditions for the ensemble members in the hindcast experiments are created based on a method called "breeding of growing modes" (Toth and Kalnay, 1993, 1997) which has its origin in weather forecasting. For the breeding, the control simulation (here the historical simulation and RCP4.5 in MPI-ESM) is run a second time over the hindcast period from perturbed initial conditions starting on the 1st January 1990 and 2040, respectively.

After one rescaling interval (=breeding cycle) – in which the error with respect to the control simulation grows in time – the ocean component of the breeding run is rescaled by bred vectors to the control simulation. Bred vectors are computed from the difference between the control run and the

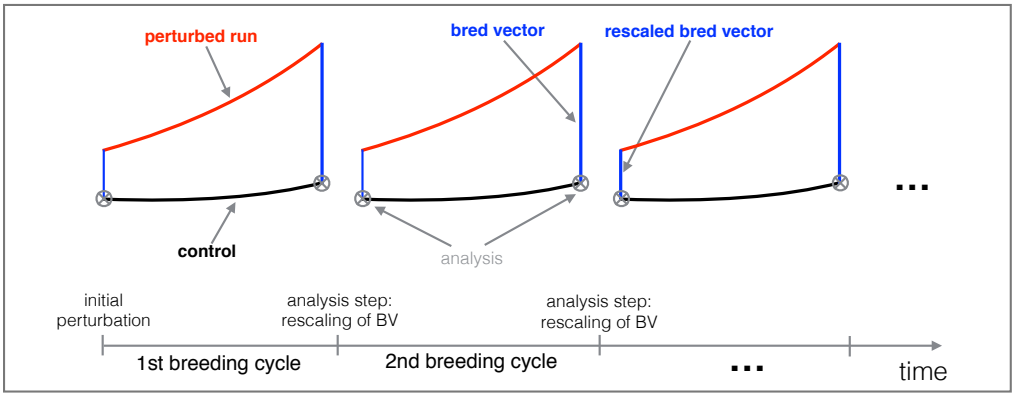

Figure 4.1: Sketch of the breeding method for 3 breeding cycles.

initially perturbed run, which is then rescaled or normalized. Two parameters can be used to tune the breeding in the model: the length of the breeding cycle and the rescaling amplitude (norm). The length of the breeding cycle is set to one year, the (vertically dependent) norm is based on 10% of the standard deviation computed over the Pacific ENSO region (15°N/S). After some breeding cycles – here 5 breeding cycles used for practical reasons – the bred vectors resemble the fastest growing modes of the model and the initial perturbations can no longer be distinguished. The perturbed initial conditions obtained from normalized bred vectors can be used to initialize the hindcasts. The breeding method is sketched in Fig.4.1. The exact implementation in the model is described in Baehr and Piontek (2013).

For the analysis of the potential predictability of the AMOC and meridional heat transport for the current climate state, I use an ensemble hindcast experiment which is initialized from the CMIP5 historical simulation extended with the RCP4.5 scenario after 2005 in MPI-ESM (HIST_{ens}). For HIST_{ens}, 10 ensemble members with yearly start dates are started on the 1st of January of every year between 1995 and 2014. The hindcasts are each integrated for 10 years. The total hindcast experiment HIST_{ens} spans the period 1995 to 2023. Additionally, a second set of hindcasts is run for a future climate state in RCP4.5 (RCP_{ens}). Identically to HIST_{ens}, the hindcast experiment includes 10 members with yearly start dates started on the 1st of January between 2045 and 2064, which are integrated over 10 years. The total hindcast experiment RCP_{ens} spans the period 2045 to 2073. In total, the two

hindcast experiments HIST_{ens} and RCP_{ens} include 200 ensemble members, respectively.

4.2.2 Predictability analysis

Decadal predictions belong to the category of probabilistic forecasts and their predictability is often quantified based on deterministic measures like the correlation coefficient, the mean squared error (MSE) or based on the spread of the ensemble focussing on the accuracy of the prediction. In this study, the potential predictability of the AMOC and OHT is quantified depending on lead time using the anomaly correlation coefficient (ACC) in a first step, and using reliability diagrams and the Brier Skill Score (BSS) in a second step. The analysis is carried out for the present climate state in the historical ensemble experiment (HIST_{ens}, 1995-2023) and a future climate state in ensemble experiment in RCP4.5 (RCP_{ens}, 2045-2073).

Anomaly correlation coefficient

The anomaly correlation coefficient (ACC) depending on latitude and lead time can be calculated from (e.g., Collins, 2002, Pohlmann et al., 2009, Wilks, 2011):

$$ACC(t) = \frac{\sum_{i=1}^{n} \overline{[f_i - c_f]}_{(t)} \overline{[o - c_o]}_{(i+t)}}{\sqrt{\sum_{i=1}^{n} \overline{[f_i - c_f]}^2_{(t)} \sum_{i=1}^{n} \overline{[o - c_o]}^2_{(i+t)}}}, \tag{4.1}$$

where t the lead time in years, f_i is the ith monthly mean model hindcast and o the monthly mean control simulation. The control simulation in HIST_{ens} is the historical simulation extended with RCP4.5 for the period 1995 to 2023, the control simulation in RCP_{ens} is RCP4.5 for the period 2045 to 2073. In contrast to e.g. Pohlmann et al. (2009), anomalies are defined with respect to the climatologies of the forecast and control simulations c_f and c_o which

are first removed from the monthly mean data. Afterwards, the ACC is calculated for yearly means (denoted by the overbar) of the anomalies.
Anomalies of the control simulation in the ACC are defined with respect to the climatology over the respective hindcast period. In particular, in HIST_{ens} anomalies of the control simulation are defined with respect to the 1995-2023 climatology in the historical simulation extended with RCP4.5 after 2005. In RCP_{ens} anomalies of the control simulation are defined with respect to the 2045-2073 climatology in RCP4.5. For the hindcasts, anomalies are defined with respect to the ensemble mean climatology and lead time with a "leave-one-out" cross-validation applied to the data (Gangstø et al., 2013). By applying cross-validation, the considered ensemble member does not contribute to the climatology removed from it. The significance of the ACC is calculated from a bootstrapping procedure with 1000 iterations at the 95% confidence level.
In the following the anomaly correlation coefficient is evaluated for lead years 1 to 10 in HIST_{ens} and RCP_{ens} for both yearly means and multi-annual seasonal means. The anomalies are removed before yearly and seasonal means are calculated for the ACC. A linear trend is further removed before the calculation of the ACC to correct for both the forced trend from greenhouse gas forcing and the unforced model drift in the freely emerging hindcasts.
Both the AMOC and the OHT, as well as their decompositions are analyzed. The AMOC is decomposed into the wind-driven Ekman transport and the geostrophic transport (≈AMOC-Ekman transport). For the predictability analysis, I focus solely on the geostrophic transport, since the Ekman transport is assumed be little skillful (e.g., von Storch and Haak, 2008). The OHT is decomposed into overturning heat transport and gyre heat transport according to Eq.2.4.

Reliability and Brier Skill Score

The limit of deterministic measures is that uncertainties of the prediction are not mirrored in them. Therefore, the reliability and Brier Skill Score (BSS) of the prediction as a probabilistic measure is

used in addition to the ACC. The analysis of the reliability of a prediction can be formulated with reliability (or attributes) diagrams (e.g. Palmer et al., 2008, Corti et al., 2012, Weisheimer and Palmer, 2014) and the Brier score (Brier, 1950) which are used to determine changes in the predictability from the historical climate state in HIST_{ens} to a future climate state in RCP_{ens} in this study.

Reliability diagrams compare the forecast probabilities of a well-defined event against the observed statistical frequency with which these events actually happen. For a perfectly reliable prediction, the forecast probability equals the observed frequency of an event. The plotted pairs of forecast probability and observed frequency (=reliability curve) lie on the diagonal of the reliability diagram (grey line, e.g. in Fig.4.3) and the slope of the reliability curve is 1 (within the uncertainty) if the prediction is perfectly reliable. When the slope of the reliability curve is generally positive, the prediction is thought to have reliability. This means, that with increasing forecast probabilities, the observed frequency increases. If the reliability curve is flatter than the diagonal, the prediction is overconfident. However, if the curve is steeper than the diagonal, the prediction is underconfident. If the reliability curve is flatter than the no-skill line, the forecast probabilities cannot be considered to yield significant skill. If the curve is horizontal, the observed frequency of occurrence does not depend on the forecast probabilities. In general, the reliability is sensitive to small sample sizes.

Further, the resolution of the reliability diagram is considered and displayed in sharpness diagrams. The resolution quantifies how much the forecast probabilities differ from the climatological probability of an event. The higher the resolution, the more the forecast probabilities differ from the climatological probability. In other words, a forecast with a high resolution should be able to differentiate between high and low probabilities of an event.

The sharpness diagram shows a histogram of the relative frequency of the predicted event depending on the bins of the forecast probability. If bins of the forecast probabilities at the upper and lower bound (with forecast probabilities close to 0 and 1) of the sharpness diagram show the highest values, the resolution is high and the prediction is sharp. Ideally,

predictions should be both: sharp (high resolution) and reliable.
In addition to reliability diagrams, the Brier Skill Score (BSS) is considered for the reliability of the prediction experiments. The Brier Skill Score can be calculated from the Brier Score (BS) that is given by (Brier, 1950):

$$BS = \frac{1}{N}\sum_{i=1}^{N}(f_i - o_i)^2, \tag{4.2}$$

with N the number of realizations (pairs of forecast and event), f_i the forecast probability of the ith realization and o_i the outcome of the actual event. o_i is equal to 1 if the event occurred and 0 if not. BS measures the accuracy of a probability forecast in terms of the mean square error. BS ranges between 0 to 1, with $BS = 0$ giving a perfectly reliable forecast where the forecast probability equals the outcome of the event.
The Brier Score can be decomposed into three components of uncertainty, reliability and resolution (Murphy, 1973):

$$BS = \underbrace{\frac{1}{N}\sum_{k=1}^{K} n_k(f_k - \overline{o}_k)^2}_{\text{REL}} - \underbrace{\frac{1}{N}\sum_{k=1}^{K} n_k(\overline{o}_k - \overline{o})^2}_{\text{RES}} + \underbrace{\overline{o}(1-\overline{o})}_{\text{UNC}}, \tag{4.3}$$

with N the sample size, K number of probability classes (bins), f_k and $\overline{o}_k$ the forecast probability and observed frequency of an event in bin k and $\overline{o} = \sum_{i=1}^{N} \frac{o_i}{N}$ the overall sample averaged frequency (sample climatology). The first term (REL) gives the reliability, the second term (RES) the resolution and the third term (UNC) the uncertainty of the forecast (see also Wilks, 2011).
The reliability term measures the forecast probability against the observed relative frequency in the considered bins. The smaller the reliability is, the more reliable the prediction is thought to be. The resolution measures the the observed relative frequency against the overall sample frequency (sample climatology). The larger the resolution is, the more reliable are predictions close the forecast probability of 0 and 1. The uncertainty only depends on the observations and gives the variability of the observations.

Based on the Brier score BS, the Brier Skill Score (BSS) can be defined:

$$BSS = -\frac{BS - BS_{ref}}{BS_{ref}}, \tag{4.4}$$

with BS the Brier Score of the forecast evaluated against the Brier Score of a reference forecast BS_{ref}. Usually, the sample climatology is used for the reference forecast, so that the Brier Score can be shown to simplify to:

$$BSS = \frac{RES - REL}{UNC}. \tag{4.5}$$

Thus, the BSS can be calculated from the reliability REL, the resolution RES and the uncertainty UNC of the prediction.
Following Palmer (2000) and Corti et al. (2012), the BSS using the sample climatology as reference forecast can be decomposed as:

$$BSS = BSS_{rel} + BSS_{res} - 1, \tag{4.6}$$

since for a perfectly reliable prediction $BSS = BSS_{rel} = BSS_{res} = 1$. Here, the reliability and resolution give two contributions to the Brier Skill Score (1) $BSS_{rel} = 1 - \frac{BS_{rel}}{BSclim}$ and (2) $BSS_{res} = \frac{BS_{res}}{BSclim}$, which are used in this thesis in the subsequent reliability analysis.

Both, reliability diagrams and the Brier Skill Score are evaluated for the present climate ensemble HIST_{ens} and the future climate ensemble RCP_{ens} for lead years 1, 2-3 and 4-5 for multiyear yearly means and multiyear seasonal means. The range of lead years used in this study differs to the set of time scales suggested by Goddard et al. (2013). However, these timescales turned out to be a reasonable choice for the analysis of the reliability in this study. Here, the reliability and BSS are analyzed for the ensemble predictions HIST_{ens} and RCP_{ens} against the respective reference that is the historical simulation extended with RCP4.5 between 1995 and 2023 for HIST_{ens} and RCP4.5 between 2045 and 2073 for RCP_{ens}. The reliability diagrams in the following analysis are shown for non-detrended data. Detrending is used to filter out the global warming effect that considerably effects the reliability of the prediction (Corti et al., 2012). In particular, the reliability is

investigated for the subtropical gyre (20°N-40°N) and the subtropical gyre (40°N-60°N) with all available information included in the analysis, because smaller latitude bands yielding a smaller sample size do not allow a sensible reliability analysis. The reliability diagrams and BSS are investigated here for the events of the AMOC and OHT being above the time mean of yearly means and of the multiyear seasonal means over the hindcast period.

4.3 Predictability of the AMOC

This section analyses the ACC in HIST$_{ens}$ and changes in RCP$_{ens}$ for the AMOC and the geostrophic volume transport (≈AMOC-Ekman) together with the reliability of the prediction of the AMOC. The ACC is analyzed for both yearly and multiyear seasonal means, the reliability analysis focusses on yearly means and multiyear summer and winter means.

4.3.1 Yearly mean AMOC

The anomaly correlation coefficient for yearly means of the AMOC is shown in Fig.4.2. The ACC in HIST$_{ens}$ (Fig.4.2a) shows positive ACCs of more than

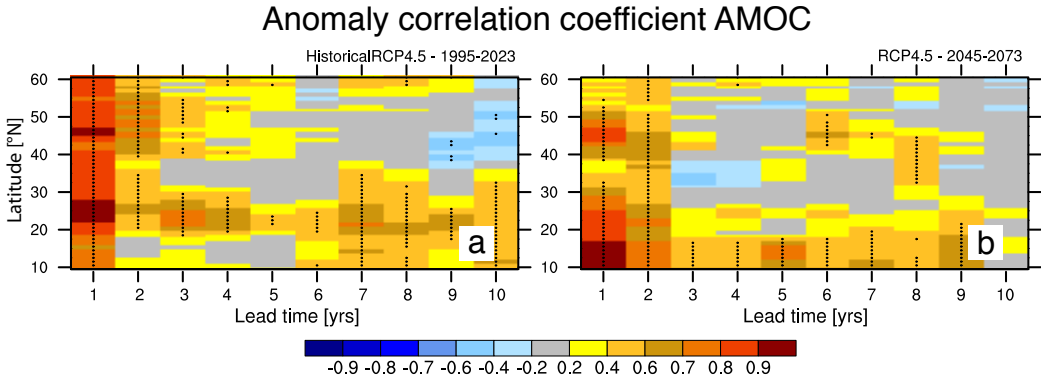

Figure 4.2: Anomaly correlation coefficient (ACC) of the AMOC for yearly means for **(a)** the historical ensemble spanning 1995-2023 and **(b)** the future ensemble in RCP4.5 spanning 2045-2073. The panels show the ACC for lead times of 1 to 10 years plotted against latitude. The stippling indicates correlation coefficients significant at the 95% confidence level.

0.8 in the subtropical and subpolar gyre in the first lead year. For longer lead times, the AMOC shows skill in the subtropical gyre between about 20°N and 30°N with significant predictable lead times mostly limited to about 4 years and in the subpolar gyre with significant predictable lead times of 1-4 years, where predictable lead times of 4 years only show up at some specific latitudes. Bootstrapping gives a significance level of about 0.4. Significant ACCs are shown with stippling in Fig.4.2 and subsequently. Around 25°N, significant predictable lead times of up to 10 years occur. In lead year 7, the ACC of the AMOC shows a re-emergence of skill in the subtropical gyre with significant correlations for lead times up to ten years north of about 25°N and in the tropical Atlantic. But a clear reason of re-emergence of skill in the experiment has not yet been found and would need further analysis.
The ACC in RCP_{ens} (Fig.4.2b) shows prominent changes at the latitudes with predictability in HIST_{ens}. The ACC in the first lead year drops to values of less then 0.4 at some latitudes, which have shown ACCs larger than 0.8 in HIST_{ens}. In both, the subtropical and subpolar gyre, significant predictable lead times are limited to two years in RCP_{ens}. The tropical NA in contrast shows increased significant predictable lead times of up to 9 years with increased ACCs in RCP_{ens}. Overall, the skill of the AMOC in HIST_{ens} is significantly reduced and mostly lost in the subtropical and the subpolar gyre after the second lead year .
However, it is unclear whether the prediction of the AMOC is reliable in the model and how the reliability of the prediction changes in RCP_{ens}, whether the changes in ACC are related to specific seasons and how the AMOC's geostrophic transport contributes to the changes in the ACC. To further shed light on the changes in the predictability of the AMOC, reliability diagrams and the BSS for yearly means, the ACC for seasonal means (winter spring, summer and autumn), reliability diagrams and the BSS for winter and summer means of the AMOC, and the ACC for the geostrophic transport are analyzed in the following.

Reliability diagrams for the AMOC for lead years 1, 2-3 and 4-5 are shown in Fig.4.3 for the subtropical gyre (20°N-40°N) and the subpolar gyre (40°N-60°N). The analysis of reliability for smaller latitude ranges is not feasible for

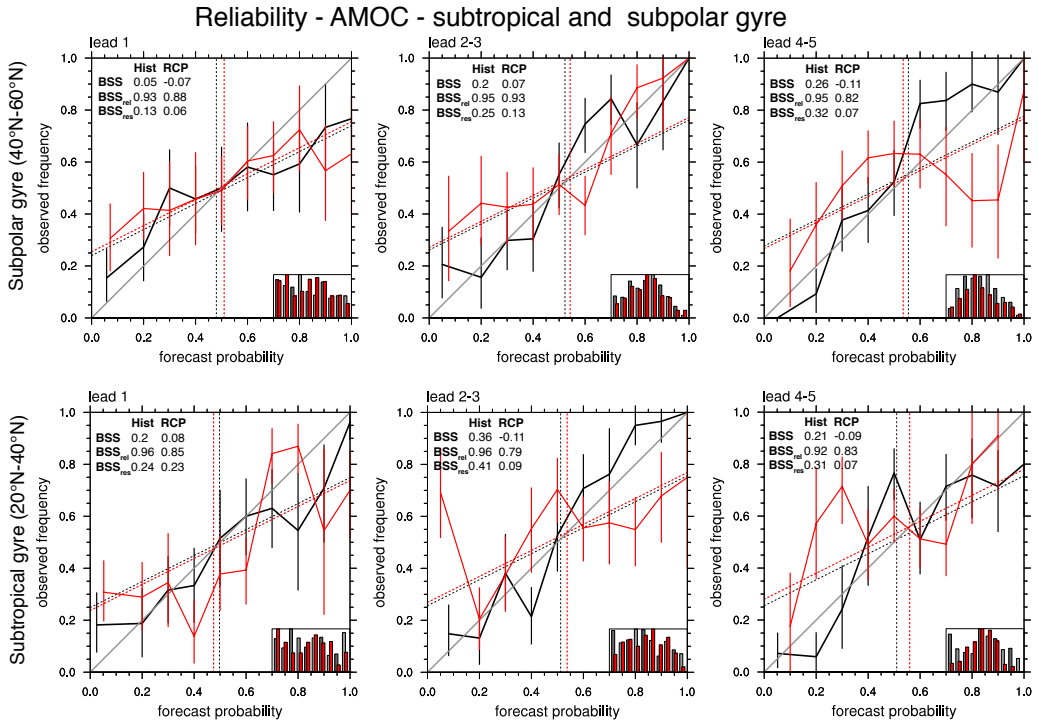

Figure 4.3: Reliability diagrams for yearly means of the AMOC in the subtropical (20°N-40°N) and subpolar (40°N-60°N) North Atlantic for the historical ensemble (black) and the future RCP4.5 ensemble (red) for lead year 1 (left), 2-3 (middle) and 4-5 (right) for the condition "events above the mean". Upper panels: subpolar gyre, lower panels: subtropical gyre. Red and black vertical bars show the uncertainty in the observed frequency estimated at the 95% confidence level with a bootstrap resampling based on 1000 iterations for each probability bin. The dashed black and red lines divide skillful and unskillful areas. Also shown in the bottom right corner are the respective sharpness diagrams for the historical ensemble (grey) and the future RCP4.5 ensemble (red) showing the number of events against the forecast probabilities.

the AMOC and the OHT.

The AMOC in the subtropical gyre shows significant changes in the reliability of the ensembles from HIST$_{ens}$ to RCP$_{ens}$. In HIST$_{ens}$, the prediction exhibits some reliability. The BSS yields 0.2 in HIST$_{ens}$ and 0.08 in RCP$_{ens}$ for lead year 1 (Fig.4.3). In HIST$_{ens}$, the reliability curve fluctuates closely around the diagonal, whereas in RCP4.5 larger differences occur between the reliability curve and the perfect reliability line on the diagonal. In HIST$_{ens}$, the BSS remains 0.36 for lead years 2-3 and 0.21 for lead years 4-5 with a reasonable sharpness and resolution BSS_{res}. In accordance to the reasonable BSS, the reliability remains high with a BSS_{rel} of 0.96 for lead years 2-3 and 0.92 for lead years 4-5 and reliability curves close to the diagonal. In

RCP_{ens} the reliability and the BSS decrease further for lead years 2-3 and 4-5. The reliability curve show significant differences to the diagonal and the prediction is not thought to be reliable. The sharpness and resolution decrease for increasing lead times. For lead years 4-5, the observed frequencies in the sharpness diagram are centered predominantly around the climatological forecast probability of around 0.5. The reliability component BSS_{rel} is generally large in HIST_{ens} and RCP_{ens} but drops in RCP_{ens} to 0.85 for lead year 1, to 0.79 for lead years 2-3 and to 0.83 for lead years 4-5. In HIST_{ens}, BSS_{rel} is highest for lead years 1 and 2-3 (Fig.4.3).
The resolution component BSS_{res} has the largest impact in the BSS and determines the generally low BSS in RCP_{ens}. Whereas BSS_{res} is reasonable for lead year 1, it further decreases with lead time for RCP_{ens} as the BSS does.
The AMOC in the subpolar North Atlantic (Fig.4.3) shows reduced reliability for lead year 1 in HIST_{ens} and RCP_{ens} compared to the subtropical gyre. The reliability curves show little skill, as the BSS. The reliability for lead years 2-3 and 4-5 indicates some skill for HIST_{ens} with a BSS of 0.2 and 0.26, respectively, whereas the reliability is low in RCP_{ens} for all lead years. For lead years 2-3 and 4-5 the sharpness is generally low in both HIST_{ens} and RCP_{ens} with observed frequencies centered around the climatological probability. Even though, the BSS_{rel} indicates a reasonable resolution in HIST_{ens} that leads to a reasonable BSS. Overall, the reliability for the AMOC is higher in the subtropical gyre than in the subpolar gyre in agreement with the ACC. The higher reliability in the subtropical gyre results from both, a higher resolution and a better sharpness, in particular in HIST_{ens}.

4.3.2 Multiyear seasonal means

To understand whether changes in the predictability of specific seasons contribute to the changes in the predictability of yearly means in the AMOC, I analyze the latitude-dependent ACC of winter (January-February-March), spring (March-April-May), summer (June-July-August) and autumn means (September-October-November), and the reliability in the subpolar gyre for

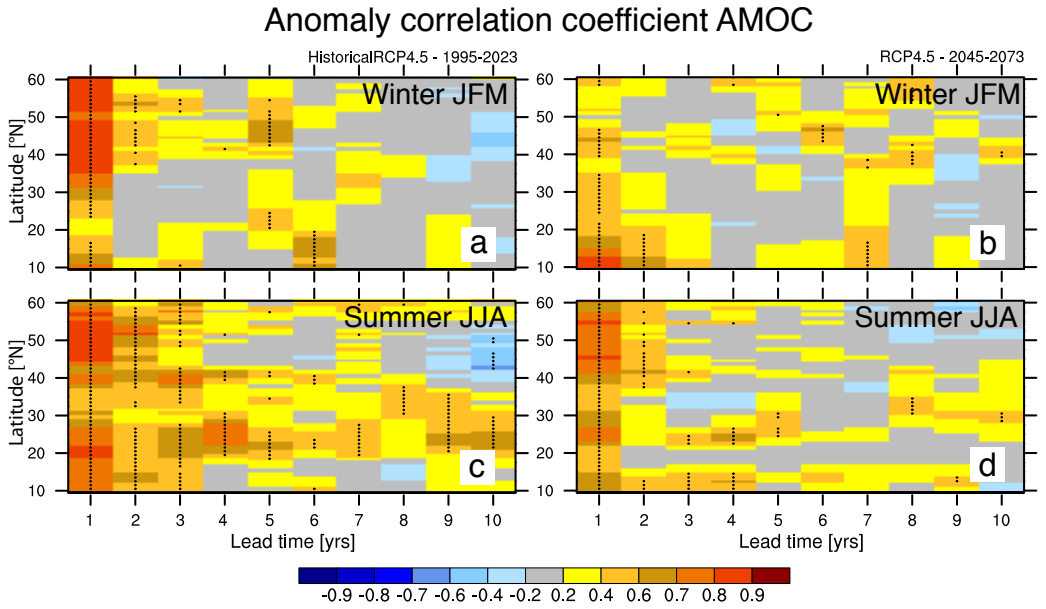

Figure 4.4: Anomaly correlation coefficient (ACC) of the AMOC for winter means (January-February-March, **a,b**) and summer means (June-July-August, **c,d**) for the historical ensemble spanning 1995-2023 **(a,c)** and the future ensemble in RCP4.5 spanning 2045-2073 **(b,d)**. The panels show the ACC for lead times of 1 to 10 years plotted against latitude. The stippling indicates correlation coefficients significant at the 95% confidence level.

winter (January-February-March) and summer (June-July-August) means.

The ACC for winter and summer means of the AMOC (Fig.4.4) shows considerable differences between the seasons in both HIST_{ens} and RCP_{ens}. During winter, the predictive skill in HIST_{ens} (Fig.4.4a) is limited to the northern part of the subtropical North Atlantic beginning north of 25°N and to the subpolar North Atlantic and mostly to the first lead year. Only some discrete latitudes indicate significant predictable lead times of 2 years. In contrast, the summer AMOC (Fig.4.4c) shows higher predictive skill in the subtropical and subpolar North Atlantic in HIST_{ens}. The summer months crucially determine the predictability of yearly means of the AMOC with significant predictable lead times of up to 7 years in the subtropical gyre around 25°N, up to 3 years in the subpolar gyre and up to 6 years at the gyre boundary at about 40°N.

In RCP_{ens}, the ACC of the AMOC is – in agreement with the yearly mean ACC – reduced at all latitudes and for both seasons. In winter (Fig.4.4b),

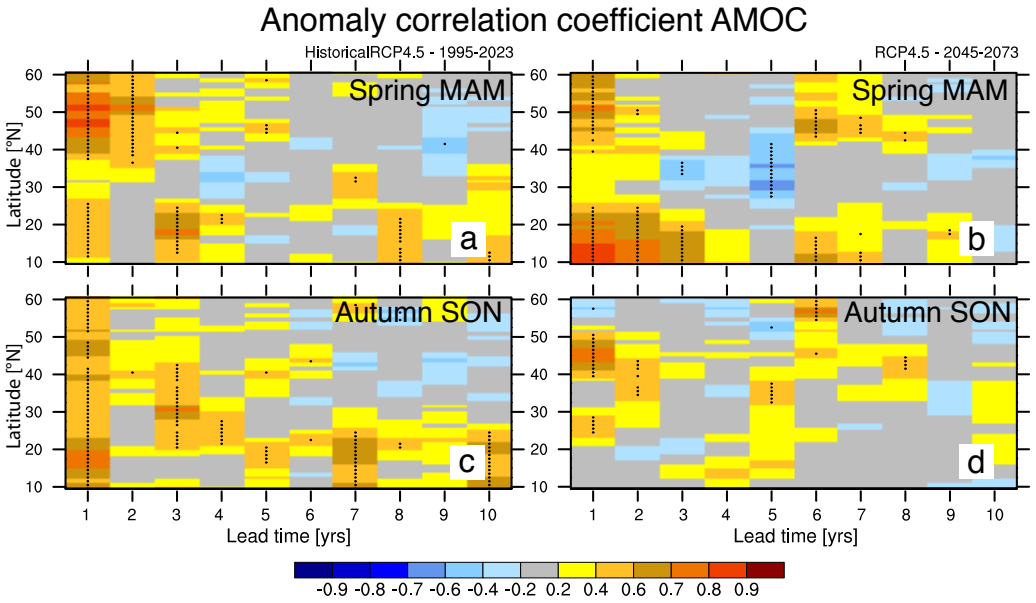

Figure 4.5: Anomaly correlation coefficient (ACC) of the AMOC for spring means (March-April-May, **a,b**) and autumn means (September-October-November, **c,d**) for the historical ensemble spanning 1995-2023 **(a,c)** and the future ensemble in RCP4.5 spanning 2045-2073 **(b,d)**. The panels show the ACC for lead times of 1 to 10 years plotted against latitude. The stippling indicates correlation coefficients significant at the 95% confidence level.

only some specific latitudes show predictability in the first lead year, but overall no predictability is found in the whole North Atlantic. For summer means (Fig.4.4d), there is some predictability in the subtropical gyre for lead year 1, but beyond that no predictability is found in the ACC. In the subpolar gyre, the ACC of the AMOC is slightly higher than in the subtropical gyre and significant predictable lead times extend to 2 years for summer means. Considering the ACC for the spring (March-April-May) and autumn (September-October-November) AMOC (Fig.4.5) shows a similar decrease in the ACC in the subtropical and subpolar North Atlantic from HIST_{ens} to RCP_{ens} and a predictability limited to one to two lead years for both seasons. Obviously, the tropics also indicate an increased predictability for seasonal means in RCP_{ens}, which is also lower than for yearly means.

Overall, all individual seasons show a lower ACC than the yearly mean AMOC, but the ACC of the AMOC summer means represent the latitudinal dependence of the ACC of yearly means of the AMOC to a large degree. The highest skill in the ACC in RCP_{ens} is found for summer means in the subpolar gyre. Therefore, the reliability of the seasonal means is analyzed for

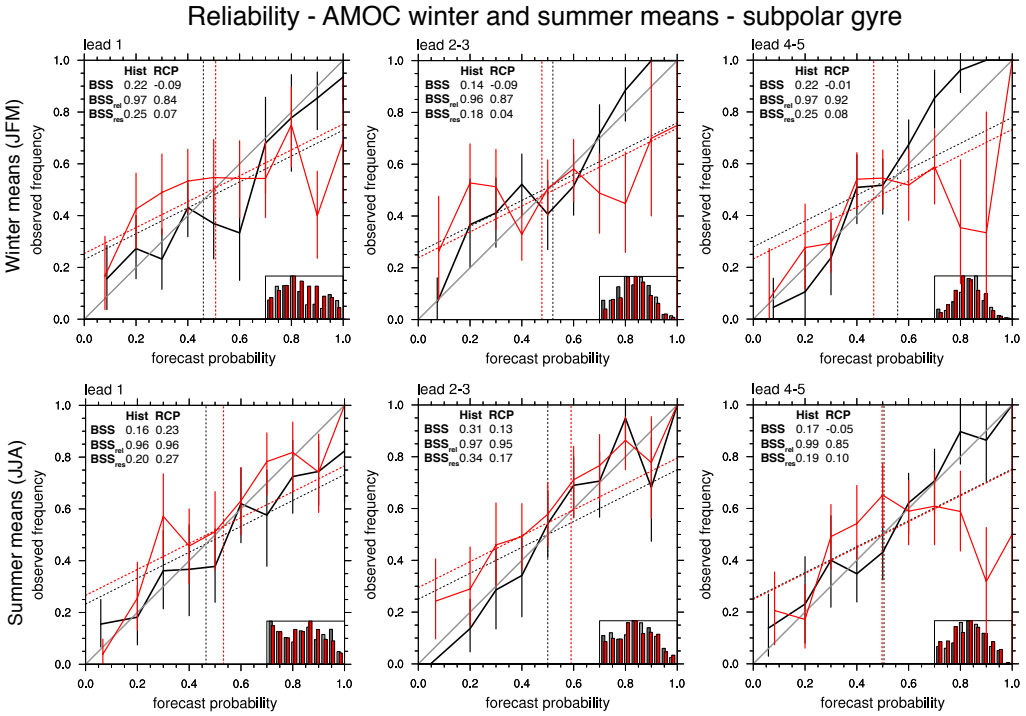

Figure 4.6: Reliability diagrams for winter means (JFM, upper panels) and summer means (JJA, lower panels) of the AMOC in the subpolar North Atlantic (40°N-60°N) for the historical ensemble (black) and the future RCP4.5 ensemble (red) for lead year 1 (left), 2-3 (middle) and 4-5 (right) for the condition "events above the mean". Red and black vertical bars show the uncertainty in the observed frequency estimated at the 95% confidence level with a bootstrap resampling based on 1000 iterations for each probability bin. The dashed black and red lines divide skillful and unskillful areas. Also shown in the bottom right corner are the respective sharpness diagrams for the historical ensemble (grey) and the future RCP4.5 ensemble (red) showing the number of events against the forecast probabilities.

the subpolar gyre in the following.

The overall reliability (BSS) for winter means of the AMOC (Fig.4.6) increases in HIST$_{ens}$ compared to yearly means resulting from a higher resolution BSS_{res} and a higher sharpness for lead year 1. The reliability is still high ($BSS_{rel} = 0.97$), also indicated by the reliability curve relatively close to the diagonal. Lead years 2-3 and 4-5 change slightly in HIST$_{ens}$ in the BSS and BSS_{res}, whereas the resolution and reliability is almost unchanged (BSS_{rel} 0.97). The sharpness drops for lead years 2-3 and 4-5. For RCP$_{ens}$ predictions of the AMOC are not reliable for all lead years indicated by a $BSS < 0$. The resolution BSS_{res} is almost 0 and the sharpness is centered around the climatological probability for all lead years.

For summer means, the reliability and the BSS (Fig.4.6) in lead years 1 and 4-5 are comparable to winter means in HIST$_{ens}$, but the BSS increases for lead-times 2-3. Especially in HIST$_{ens}$, the predictions are reliable for all lead years, where the curve is close to the diagonal and indicated by a high BSS_{rel} and reasonable BSS_{res} larger than about 0.2. RCP$_{ens}$ shows a higher reliability for lead year 1, while HIST$_{ens}$ show a higher reliability than RCP$_{ens}$ for lead years 2-3 and 4-5 where both resolution (BSS_{res}) and reliability (BSS_{rel}) are decreased in RCP$_{ens}$. Compared to winter means, the AMOC prediction is reliable for summer means in RCP$_{ens}$ for lead years 1-3. The sharpness is generally reduced. For lead year 1, HIST$_{ens}$ and RCP$_{ens}$ exhibit some sharpness and reliability and thus yield a generally reliable prediction, that is sharper than for winter means. In the subpolar gyre, the reliability is retained in RCP$_{ens}$ for summer means, while in winter and yearly means the reliability is mostly lost in RCP$_{ens}$.

Overall, especially the summer AMOC contributes positively to the predictability in the ACC of AMOC yearly means, while other seasons indicate generally low predictability in the AMOC. In concert, the summer AMOC's ACC determines the changes from HIST$_{ens}$ to RCP$_{ens}$ to a large degree. In agreement with the dominance of ACC in summer, the reliability shows in particular in RCP$_{ens}$ more reliable predictions for summers means.

4.3.3 Yearly mean geostrophic transport

After considering the effect of individual seasons on the predictability of the AMOC which showed that the summer means of the AMOC yield high predictability and determine the predictability of yearly means to a high degree, the effect on the geostrophic transport (≈AMOC-Ekman transport) is analyzed. The geostrophic transport shows in general a higher skill in HIST$_{ens}$ and RCP$_{ens}$ than the AMOC (Fig.4.7), which is due to the mechanical inertia of the ocean.
In the subtropical gyre at around 25°N, significant ACCs are found for lead times up to ten years showing correlations of more than 0.6 after lead year 7

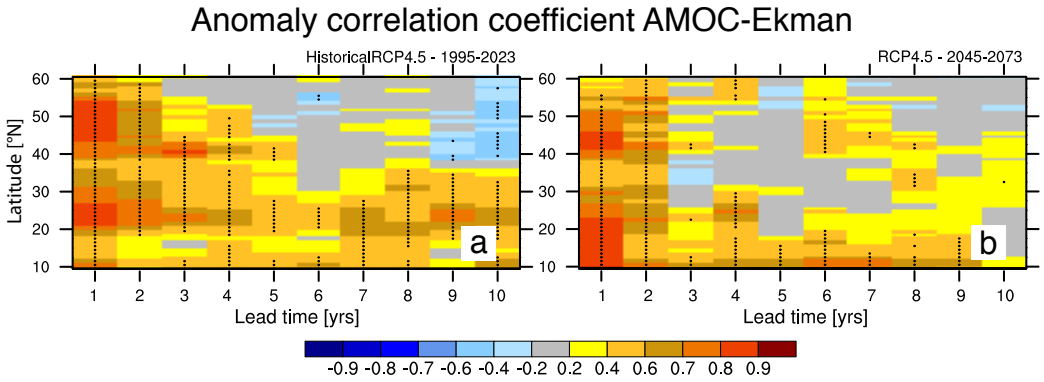

Figure 4.7: Anomaly correlation coefficient (ACC) of the geostrophic transport (AMOC-Ekman) for yearly means for **(a)** the historical ensemble spanning 1995-2023 and **(b)** the future ensemble in RCP4.5 spanning 2045-2073. The panels show the ACC for lead times of 1 to 10 years plotted against latitude. The stippling indicates correlation coefficients significant at the 95% confidence level.

for HIST_{ens} (Fig.4.7a). Between 30°N and 40°N, significant ACCs are found for lead years 1-4. At the gyre boundary (about 40°N), significant ACCs are found for lead years 1-5. In the subpolar gyre, the skill is mostly limited to lead year 2 (Fig.4.7a). At the gyre boundary at about 40°N, predictable lead times of 5 years occur.

In RCP_{ens} (Fig.4.7b) the significant predictable lead times are considerably reduced in the subtropical and at the gyre boundary and limited to 2 years in both the subtropical and subpolar gyre. The first lead year indicates a higher skill for the geostrophic transport compared to the full AMOC in RCP_{ens}. ACCs for longer lead times are generally not predictable. Thus, the most prominent changes from HIST_{ens} to RCP_{ens} in the ACC of the geostrophic transport occur in the subtropical gyre at around 25°N with a decrease in predictable lead times from 7 years to 2 years.

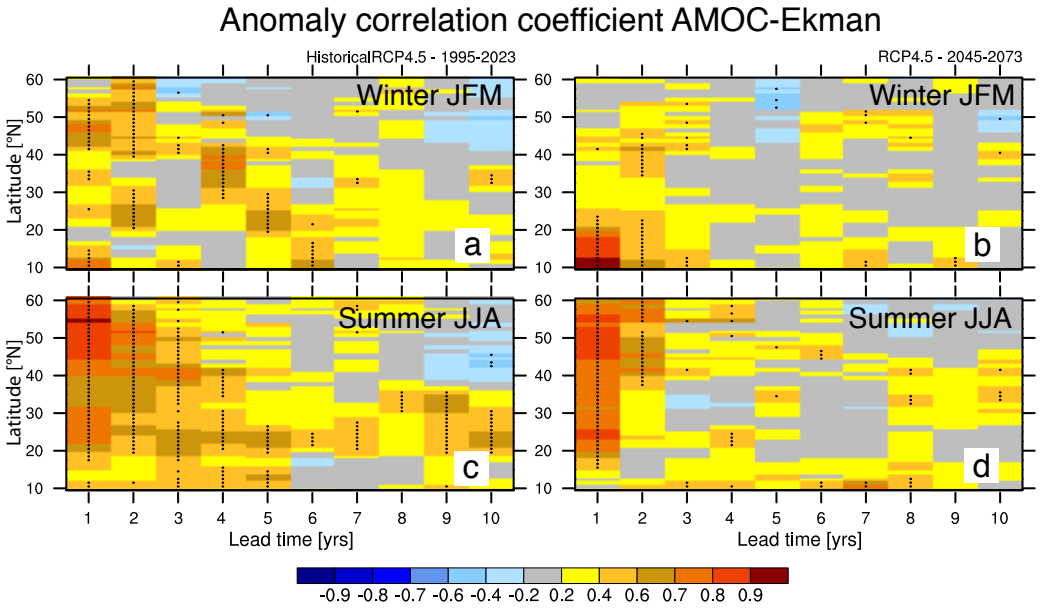

Figure 4.8: Anomaly correlation coefficient (ACC) of the geostrophic transport (AMOC-Ekman) for winter means (January-February-March, **a,b**) and summer means (June-July-August, **c,d**) for the historical ensemble spanning 1995-2023 **(a,c)** and the future ensemble in RCP4.5 spanning 2045-2073 **(b,d)**. The panels show the ACC for lead times of 1 to 10 years plotted against latitude. The stippling indicates correlation coefficients significant at the 95% confidence level.

4.3.4 Multiyear seasonal means of the geostrophic transport

Similar to the AMOC, the predictability of the geostrophic transport based on yearly means is determined by the high predictability of the summer months (Fig.4.8,4.9). In winter, the ACC in HIST_{ens} is limited to the subpolar gyre and to lead years 1-2 (Fig.4.8). In contrast, the ACC of summer means indicates skill in the subtropical and subpolar gyre with significant predictable lead times up to 7 years at about 25°N, up to 4 years between 30°N and 40°N and 2-3 years in the subpolar gyre.

In RCP_{ens} the predictability is reduced compared to HIST_{mean} (Fig.4.8). While the ACC in winter exhibits no skill in the subtropical and subpolar gyre, the ACC in summer shows predictable lead times of 2 years in the subpolar gyre and 1 year in the subtropical gyre, but no skill beyond.

The spring and autumn ACC of the geostrophic transport reveals (Fig.4.9) that especially the spring also contributes considerably to the ACC of the

yearly mean geostrophic transport. For spring means (Fig.4.9), significant predictable lead times appear in the subtropical gyre at specific latitudes up to 9 years, but predictable lead times are generally limited to 3-4 years. In the subpolar gyre, the ACC of spring means also shows significant predictable lead times of up to 3 years.

In the subtropical gyre, significant ACCs of spring means cover 1-2 lead years in RCP$_{ens}$. In the subpolar gyre, predictable lead time up to 4 years occur that represent the longest predictable lead times found for the geostrophic transport in RCP$_{ens}$. In autumn, skillfull ACCs are mostly found in the first lead year for both HIST$_{ens}$ and RCP$_{ens}$. Around 25°N, predictability is found for lead years 1 and 3-10 in HIST$_{ens}$, whereas lead year 2 shows a drop in the ACC. Correspondingly, predictability is found in RCP$_{ens}$ around 25°N, whereas the ACC is limited to a narrower latitude band and to lead times of 1-4 years, but still reveals some predictability around 25°N.

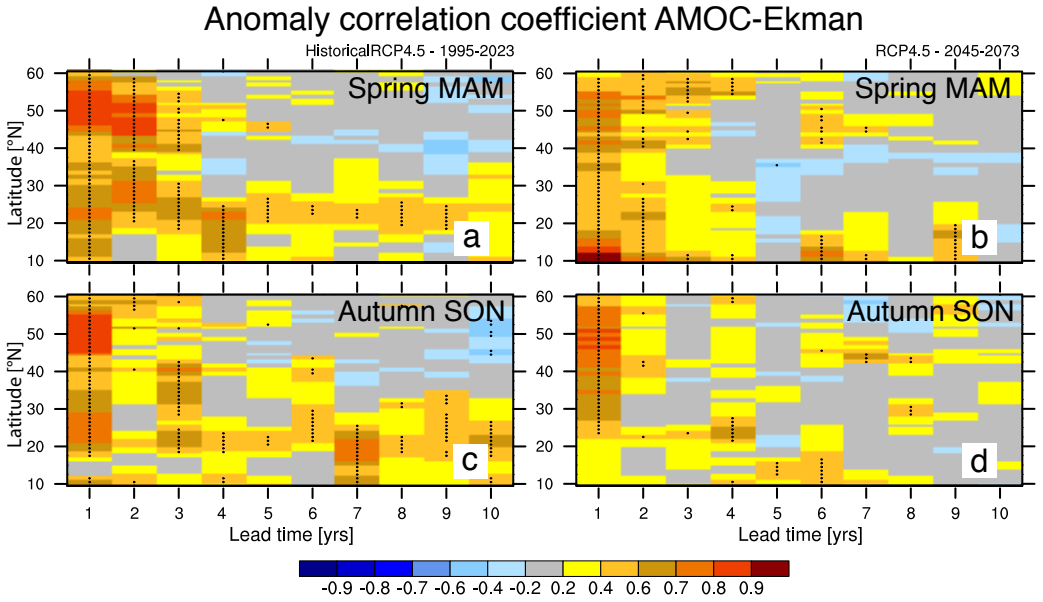

Figure 4.9: Anomaly correlation coefficient (ACC) of the geostrophic transport (AMOC-Ekman) for spring means (March-April-May, **a,b**) and autumn means (September-October-November, **c,d**) for the historical ensemble spanning 1995-2023 **(a,c)** and the future ensemble in RCP4.5 spanning 2045-2073 **(b,d)**. The panels show the ACC for lead times of 1 to 10 years plotted against latitude. The stippling indicates correlation coefficients significant at the 95% confidence level.

4.4 Predictability of the OHT

This section analyses the ACC for the OHT, the overturning heat transport and the gyre heat transport together with the reliability of the OHT. The ACC is analyzed for both yearly and multiyear seasonal means, the reliability analysis focusses on yearly means and multiyear summer and winter means.

4.4.1 Yearly means of the OHT

As shown before, the variability of the OHT is connected to the variability of the AMOC mainly through the variability in the velocity field. Nevertheless, the variability is not exchangeable with the AMOC as is the predictability (e.g. Tiedje and Baehr, 2014). To analyze the predictability of the OHT the ACC, reliability diagrams and the Brier Skill Score are used as before.
The total OHT reveals potential predictability in the subtropical and subpolar North Atlantic (Fig.4.10). In the subtropical North Atlantic significant ACCs are found between 20°N to 25°N for lead years 1-4, while other latitudes in the tropical and subtropical North Atlantic indicate only skill in the first lead year in HIST_{ens} (Fig.4.10a). In the subpolar gyre, significant ACCs are found between 40°N to 60°N for lead years 1-2 in HIST_{ens}. Between 40°N to 50°N, significant correlations re-emerge around lead years 5-6, even if the ACC can be considered to yield robust predictability mostly for lead years 1-2 (Fig.4.10a).
The predictability in the OHT changes in RCP_{ens} (Fig.4.10b). While in the subtropical gyre, most latitudes north of 25°N significant predictable lead times limited to 2 years, the subpolar gyre shows increased ACCs and longer significant predictable lead times of up to 4 years. Only between 20°N and 25°N the lead times are shortened in RCP_{ens} compared to HIST_{ens}. Overall, the OHT reveals an increase in its predictability in the ACC from HIST_{ens} to RCP_{ens}, except of 25°N, where predictable lead times are shortened. The highest ACCs occur in the subpolar gyre in both ensemble experiments.

The reliability diagram reveals similar changes in the predictability of the

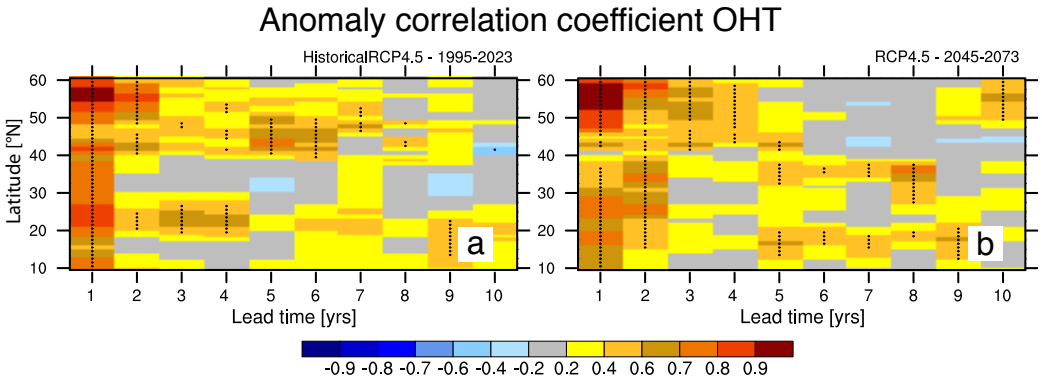

Figure 4.10: Anomaly correlation coefficient (ACC) of the OHT for yearly means for **(a)** the historical ensemble spanning 1995-2023 and **(b)** the future ensemble in RCP4.5 spanning 2045-2073. The panels show the ACC for lead times of 1 to 10 years plotted against latitude. The stippling indicates correlation coefficients significant at the 95% confidence level.

OHT in the subtropical gyre (Fig.4.11). In HIST_{ens} the predictions exhibit reliability in the OHT with a $BSS = 0.2$ in the subtropical gyre for lead year 1 and $BSS = 0.15$ for lead year 2-3 (Fig.4.11). In concert with the ACC around 25°N, the reliability diagram for the OHT shows a reduction in skill for lead years 1 and 2-3 in concert with a decrease in BSS, BSS_{rel} and BSS_{res} between HIST_{ens} and RCP_{ens} (Fig.4.11). For lead year 4-5 neither HIST_{ens} nor RCP_{ens} provide reliable predictions. For lead year 1, both ensemble experiments exhibit sharpness, for lead years 2-3 and 4-5 the sharpness is reduced with increasing lead time. For lead years 4-5, the sharpness is centered mostly around the climatological probability.

In the subpolar gyre (Fig.4.11), HIST_{ens} exhibits reliability for all lead years with a reasonable BSS of about 0.3. For lead year 1, the reliability BSS_{rel} and the resolution BSS_{res} are considerably reduced in RCP_{ens}, even though the relative frequencies still exhibit sharpness. Only for lead years 2-3, RCP_{ens} exhibits some reliability indicated by a reliability curve closer to the diagonal and a BSS of 0.13. Lead years 2-3 also exhibit sharpness, for lead years 4-5 the sharpness is reduced. Overall, the subpolar gyre reveals the highest reliability in the OHT, that persists for lead years 2-3 in HIST_{ens} and RCP_{ens} and even for lead years 4-5 in HIST_{ens}. For the OHT, reliability diagrams reveal higher skill in the subpolar gyre than in the subtropical gyre in concert with higher ACCs found in the subpolar than in the subtropical

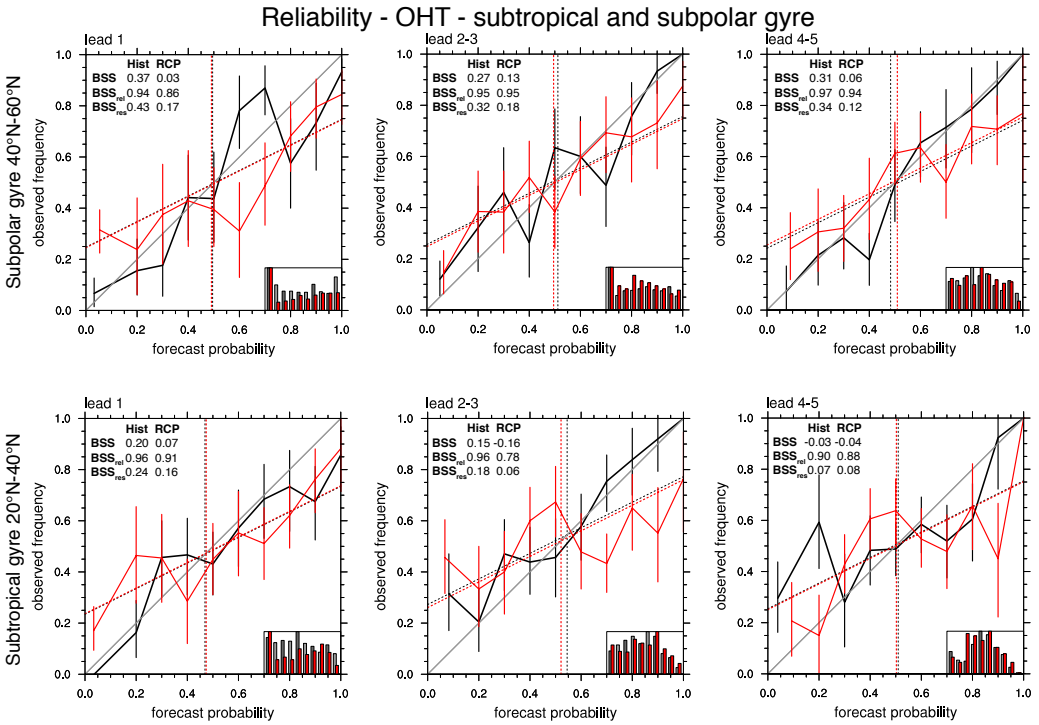

Figure 4.11: Reliability diagrams for yearly means of the OHT in the subpolar North Atlantic (40°N-60°N, upper panels) and in the subtropical North Atlantic (20°N-40°N, lower panels) for the historical ensemble (black) and the future RCP4.5 ensemble (red) for lead year 1 (left), 2-3 (middle) and 4-5 (right) for the condition "events above the mean". Upper panels: subpolar gyre, lower panels: subtropical gyre. Red and black vertical bars show the uncertainty in the observed frequency estimated at the 95% confidence level with a bootstrap resampling based on 1000 iterations for each probability bin. The dashed black and red lines divide skillful and unskillful areas. Also shown in the bottom right corner are the respective sharpness diagrams for the historical ensemble (grey) and the future RCP4.5 ensemble (red) showing the number of events against the forecast probabilities.

gyre.

4.4.2 Multiyear seasonal means of the OHT

To investigate whether summer or winter means of the OHT control the predictability of the yearly mean OHT, the ACC of seasonal means and the reliability of winter and summer means are investigated in the following.

The ACC of the OHT reveals changes between individual seasons (Fig.4.12,4.13). In the subtropical North Atlantic, the ACC shows little skill with significant predictable lead times of 1 year in HIST_{ens} and RCP_{ens} for

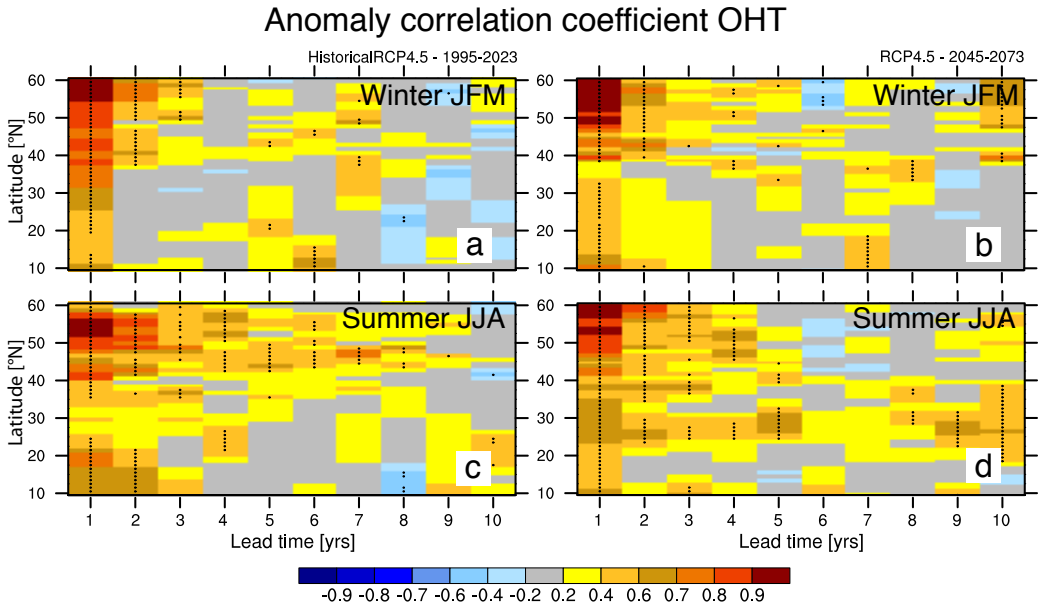

Figure 4.12: Anomaly correlation coefficient (ACC) of the OHT for winter means (January-February-March, **a,b**) and summer means (June-July-August, **c,d**) for the historical ensemble spanning 1995-2023 **(a,c)** and the future ensemble in RCP4.5 spanning 2045-2073 **(b,d)**. The panels show the ACC for lead times of 1 to 10 years plotted against latitude. The stippling indicates correlation coefficients significant at the 95% confidence level.

winter means (Fig.4.12a,b). In the subpolar gyre, the ACC in lead year 1 exceeds the ACC in the subtropical gyre and shows significant predictable lead times of up to 3 years in HIST_{ens} (Fig.4.12a) and up to 2 years – but higher correlations in the first lead year – in RCP_{ens} for winter means (Fig.4.12b). Beyond that, no skill is found in winter, similar to the AMOC. In contrast, for summer means significant ACCs are found up to 7 years between 40°N and 50°N and up to 4 years between 50°N and 60°N in the subpolar gyre in HIST_{ens} (Fig.4.12c) that partly re-emerge at specific latitudes as found in the yearly mean ACC (Fig.4.10). In the subtropical gyre, limited predictability is found between 25°N and 35°N in HIST_{ens} for lead year 1. In-between the ACC is not significant. In RCP_{ens}, the ACC for summer means is not considerably changed compared to HIST_{ens} in the subpolar gyre (50°N-60°N) with significant predictable lead times of still 4 years. Between 40°N and 50°N, predictable lead times are shortened to 4 years in RCP_{ens}. Sharply south of 40°N the significant ACCs extend over lead years 1-3, which also hinted at in HIST_{ens} but less clear. At around 25°N, the strip of predictable lead times in the ACC of up to 4 years that is

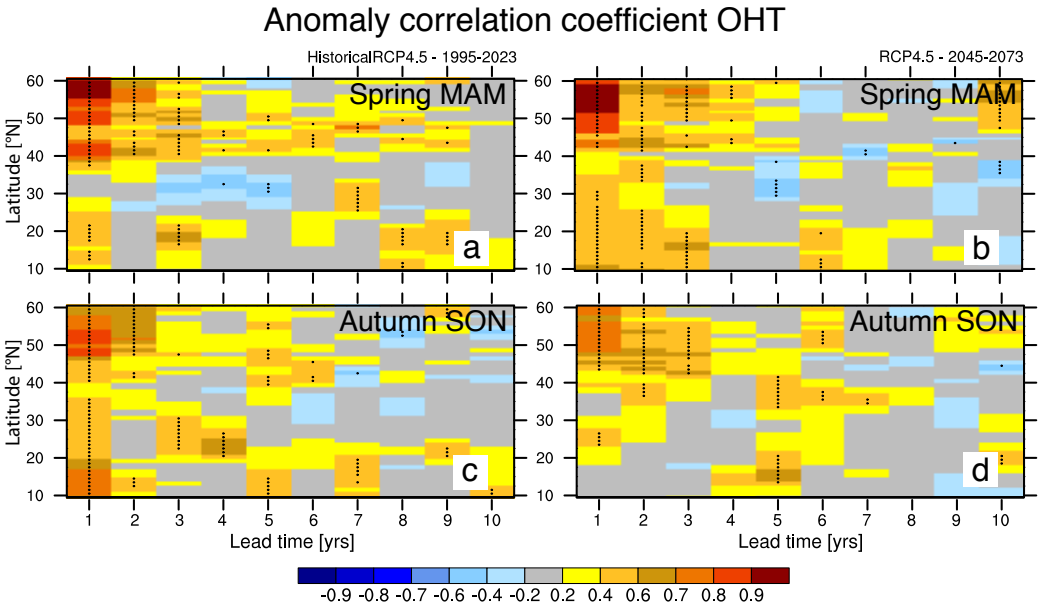

Figure 4.13: Anomaly correlation coefficient (ACC) of the OHT for spring means (March-April-May, **a,b**) and autumn means (September-October-November, **c,d**) for the historical ensemble spanning 1995-2023 **(a,c)** and the future ensemble in RCP4.5 spanning 2045-2073 **(b,d)**. The panels show the ACC for lead times of 1 to 10 years plotted against latitude. The stippling indicates correlation coefficients significant at the 95% confidence level.

visible in the yearly mean OHT's ACC in HIST_{ens} reappears in RCP_{ens} for the ACC of summer means showing that there is still predictability at around 25°N. Thus, the predictability at 25°N is either limited to summer months or covered by the influence of other seasons in the yearly mean ACCs.

Spring and autumn ACCs (Fig.4.13) show that both seasons contribute mostly in the subpolar gyre to the OHT predictability, while the ACC in the subtropical gyre is generally small and not significant in HIST_{ens} and RCP_{ens}. Further, the spring ACCs in RCP_{ens} show skill in the tropical and (southern) subtropical North Atlantic with predictable lead times up to 3 years. Similar to the AMOC, the highest skill appears in the OHT ACCs for summer means, that project on the yearly means of the OHT.

Since the highest skill in the OHT multiyear seasonal means is found in the subpolar North Atlantic, I focus in the following on the reliability of the OHT summer and winter means between 40°N to 60°N. According to the ACC, HIST_{ens} and RCP_{ens} exhibit reliable predictions for lead year 1 and 2-3 for

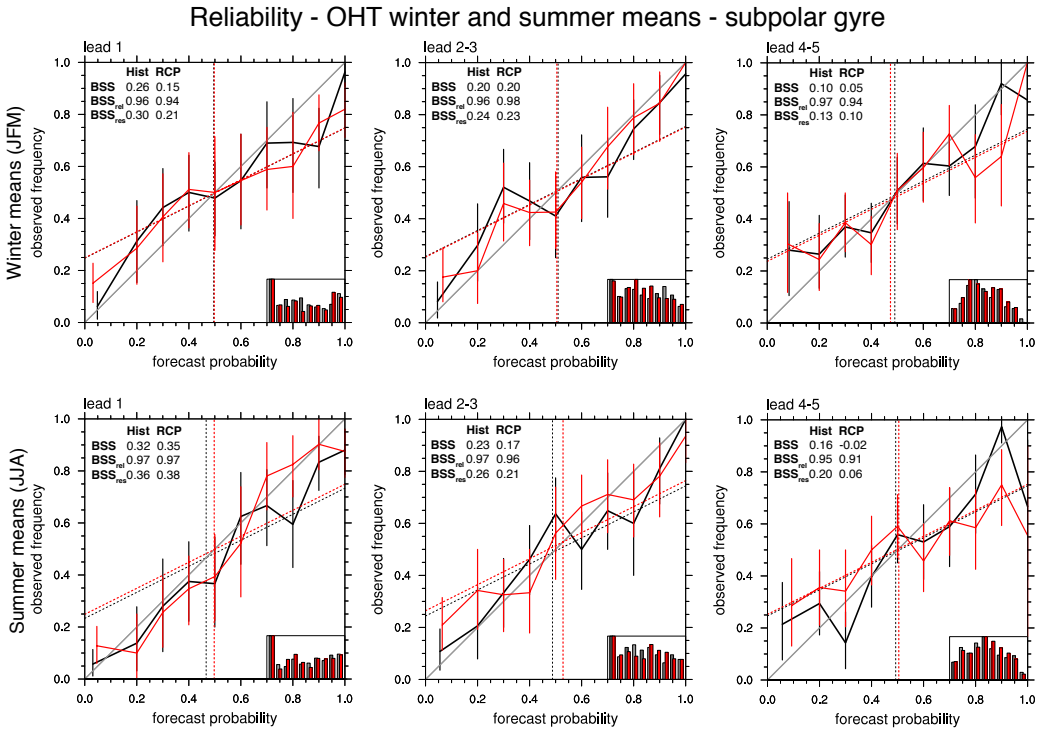

Figure 4.14: Reliability diagrams for winter means (JFM) of the OHT in the subpolar North Atlantic (40°N-60°N) for the historical ensemble (black) and the future RCP4.5 ensemble (red) for lead year 1 (left), 2-3 (middle) and 4-5 (right) for the condition "events above the mean". Red and black vertical bars show the uncertainty in the observed frequency estimated at the 95% confidence level with a bootstrap resampling based on 1000 iterations for each probability bin. The dashed black and red lines divide skillful and unskillful areas. Also shown in the bottom right corner are the respective sharpness diagrams for the historical ensemble (grey) and the future RCP4.5 ensemble (red) showing the number of events against the forecast probabilities.

winter means and summer means (Fig.4.14). Lead years 4-5 of winter means in HIST_{ens} and RCP_{ens} show a drop in the BSS and the reliability curve that deviates more from the diagonal due to a reduced resolution (BSS_{res}). The sharpness is also considerably reduced for lead years 4-5. Lead years 4-5 of summer means reveal a more reliable prediction in HIST_{ens} with $BSS = 0.16$ than in RCP_{ens} with $BSS = -0.02$. This drop results from a decrease in the resolution (BSS_{res}). In concert, the sharpness is lost and the relative frequencies center around the climatological probability. In summary, the reliability is higher for seasonal means than for yearly means in HIST_{ens} and RCP_{ens} with summer means being more reliable than winter means. Reliability diagrams also show a decrease in skill for all seasons between HIST_{ens} and RCP_{ens}.

4.4.3 Yearly means of the overturning and gyre heat transport

The ACC of the overturning heat transport in the tropical and subtropical North Atlantic is limited to the first lead year in HIST_{ens} (Fig.4.15a). In the subpolar gyre, the overturning heat transport in HIST_{ens} reveals predictable lead times of 1-5 years, where latitudes between 40°N to 50°N exhibit a higher predictability than 50°N to 60°N. Around 20°N, significant correlation re-emerge for lead years 3-4. In RCP_{ens} (Fig.4.15e), significant ACCs extend over lead years 1-2 in the subtropical gyre. Between 30°N and 40°N, the ACC yields non-significant correlations for lead year 1. In the subpolar gyre, significant ACCs are found up to lead year 3 between 40°N and 50°N.

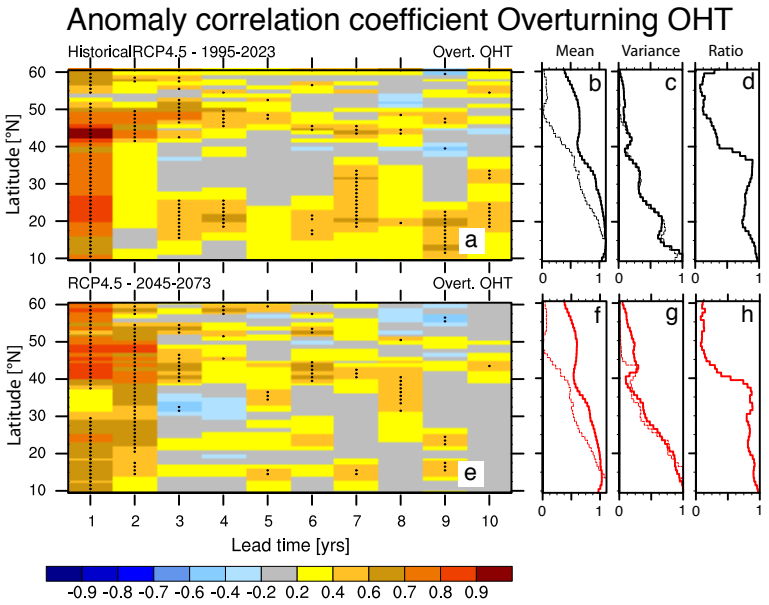

Figure 4.15: Anomaly correlation coefficient (ACC) of the overturning heat transport for yearly means for **(a)** the historical ensemble spanning 1995-2023 and **(e)** the future ensemble in RCP4.5 spanning 2045-2073. The panels show the ACC for lead times of 1 to 10 years plotted against latitude. The stippling indicates correlation coefficients significant at the 95% confidence level. **(b-d)** Historical simulation (reference run): **(b)** mean and **(c)** variance (scaled by the maximum of the total OHT variance between 10°N-60°N) of the total OHT (solid line) and the overturning heat transport (thin-dashed) and **(d)**the ratio of the overturning to the total OHT variance $(Var(H^{ov})/[Var(H^{total} - Cov(H^{gyre}, H^{ov})])$. **(f-h)** RCP4.5 (reference run): **(f)** mean and **(g)** variance (scaled by the maximum of the total OHT variance between 10°N-60°N) of the total OHT (solid line) and the overturning heat transport (thin-dashed) and **(h)** the ratio of the overturning to the total OHT variance.

The ACC of the gyre heat transport in HIST$_{ens}$ (Fig.4.15) reveals a high skill the with a maximum in the subtropical gyre (correlations larger than 0.9). Between 15°N and about 30°N, predictable lead times up to ten years occur. In the northern part of the subtropical gyre, predictable lead times are limited to 3-5 years. In the subpolar gyre, the ACC indicates lower skill with predictable lead times up to 8 years at specific latitudes between 40°N to 50°N and about 2 years north of 50°N. In RCP$_{ens}$ the overall ACC of the gyre heat transport (Fig.4.15e) is lower in the subtropical gyre, significant predictable lead times are mostly limited to 8 years between 30°N and 40°N. In the subpolar gyre, the ACC is increased and shows longer predictable lead times up to 4 years north of 50°N between HIST$_{ens}$ and RCP$_{ens}$ (Fig.4.15e), while south of 50°N the predictable lead times are limited to about 6 years in RCP$_{ens}$.

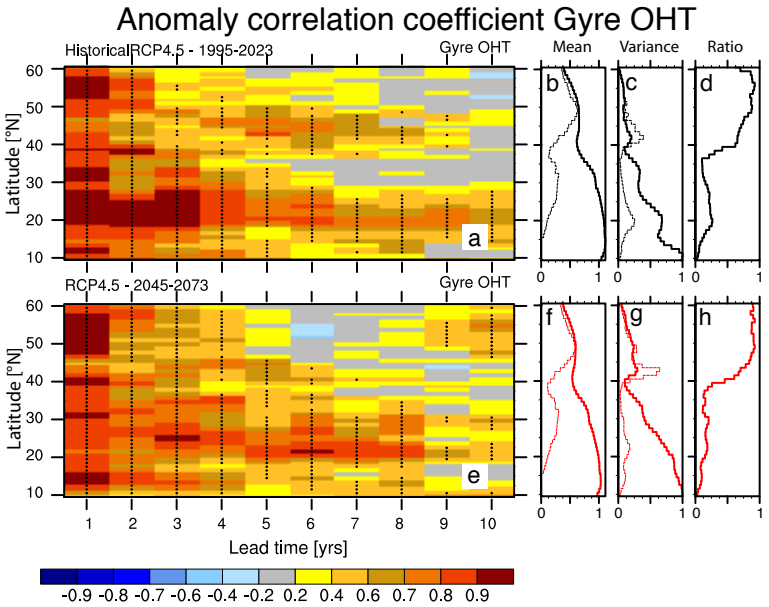

Figure 4.16: Anomaly correlation coefficient (ACC) of the gyre heat transport for yearly means for **(a)** the historical ensemble spanning 1995-2023 and **(e)** the future ensemble in RCP4.5 spanning 2045-2073. The panels show the ACC for lead times of 1 to 10 years plotted against latitude. The stippling indicates correlation coefficients significant at the 95% confidence level. **(b-d)** Historical simulation (reference run): **(b)** mean and **(c)** variance (scaled by the maximum of the total OHT variance between 10°N-60°N) of the total OHT (solid line) and the gyre heat transport (thin-dashed) and **(d)**the ratio of the gyre to the total OHT variance ($Var(H^{ov})/[Var(H^{total} - Cov(H^{gyre}, H^{ov})]$). **(f-h)** RCP4.5 (reference run): **(f)** mean and **(g)** variance (scaled by the maximum of the total OHT variance between 10°N-60°N) of the total OHT (solid line) and the gyre heat transport (thin-dashed) and **(h)** the ratio of the gyre to the total OHT variance.

4.4.4 Contribution of the overturning and gyre heat transport to the predictability of the OHT

The high predictability in the ACC of the gyre heat transport compared to the ACC of the overturning heat transport – especially in the subtropical North Atlantic – initiates to consider the relative importance of the predictability of the gyre and overturning heat transport to the predictability of the OHT. The overturning heat transport dominates the mean of the OHT in the tropical and subtropical North Atlantic (Fig.4.15b, shown for the reference run), as also shown in earlier model studies (Jayne and Marotzke, 2001, Dong and Sutton, 2002). Similarly the variance in the tropical and subtropical North Atlantic is dominated by the overturning heat transport (Fig.4.15c,d, Fig.4.16c,d). In Fig.4.15d, the ratio of the variance of the overturning heat transport to the variance of the total OHT minus the covariance of gyre and overturning heat transport ($Var^{ov}/[Var^{OHT} - Cov(gyre, ov)]$) is shown. Because the gyre and overturning heat transport are not independent, the covariance needs to be considered for the sum of the total variance: $Var^{OHT} = Var^{gyre} + Var^{ov} + Cov(gyre, ov)$.

From the high variance of the overturning heat transport compared to the gyre heat transport in the subtropical gyre, we can expect that the predictability of the overturning component also has a higher impact on the predictability of the total OHT. The impact of the variance can be theoretically understood for instance from the prognostic potential predictability (PPP; e.g. Pohlmann et al., 2004) which gives an upper limit of potential predictability and is in a simplified form given by:

$$PPP = 1 - \frac{\text{ensemble spread}}{\text{variance of reference run}}. \tag{4.7}$$

With the decomposition of the variance Var^{OHT} as above, the PPP forms to

$$PPP = 1 - \frac{\text{ensemble spread}}{Var^{gyre} + Var^{ov} + Cov(gyre, ov)}. \tag{4.8}$$

with the variance of the gyre heat transport Var^{gyre}, the variance of the overturning heat transport Var^{ov} and the covariance of gyre and overturning

heat transport $Cov(gyre, ov)$.
For latitudes with a low variance in the overturning heat transport (as in the subpolar gyre) where the variance of the gyre heat transport dominates the total variance (e.g. Fig.4.16c-d,g-h), the PPP yields approximately

$$PPP^{subpolar} \approx 1 - \frac{\text{ensemble spread}}{Var^{gyre} + Cov(gyre, ov)}. \tag{4.9}$$

and the PPP of the OHT is determined mostly by variance of the gyre heat transport (assuming a low covariance).
In contrast in the subtropical gyre, where the variance of the overturning heat transport dominates the OHT variance (e.g. Fig.4.15c-d,g-h) and is large compared to the variance of the gyre heat transport, the PPP yields approximately

$$PPP^{subtropical} \approx 1 - \frac{\text{ensemble spread}}{Var^{ov} + Cov(gyre, ov)}. \tag{4.10}$$

and the PPP of the OHT is determined mostly by variance of the overturning heat transport.
This suggests, that the potential predictability from the overturning heat transport in the subtropical gyre projects directly on the potential predictability of the total OHT. Although PPP and ACC cannot be used fully interchangeably, the variance suggests a similar partitioning of impact of the ACC in the overturning and gyre heat transport on the total OHT's ACC. Especially in the subtropical gyre in HIST_{ens}, where the variance of the overturning heat transport does not fully determine the variance of the OHT (e.g. around 20°N, Fig.4.15d), there might be a reasonable contribution of the gyre heat transport's ACC to the OHT's ACC. This contribution might explain the missing skill in the ACC of the overturning heat transport for lead years beyond one year compared to the ACC of the full OHT. In RCP_{ens}, the overturning heat transport shows a slight decrease in its time mean in concert with the OHT compared to HIST_{ens} (see also chapters 2 and 3). In contrast, the variances of the OHT and the overturning heat transport show a general increase in the tropical and subtropical North Atlantic. At the same time, the ratio of the variance in

the overturning heat transport to the variance of the OHT increases in the subtropical gyre, indicating a rise in the importance of the overturning heat transport to the predictability of the OHT. In contrast, the variance of the gyre heat transport dominates the variance of the OHT in the subpolar gyre.

Following also from the PPP and assuming for simplicity a constant ensemble spread (which is not investigated in the study), an increase in the variance of the reference simulation would imply an increased PPP. The increase in the variance from HIST_{ens} to RCP_{ens} in OHT in the subpolar gyre similarly hints to an increased potential predictability. This is found accordingly in the ACC of the OHT and the overturning heat transport in the subtropical gyre. Both, the OHT and the overturning OHT exhibit a more robust predictability in the subpolar gyre, with longer predictable lead times in the OHT in RCP_{ens}. Further, an increase in predictable lead times by one year occurs in the subtropical gyre in RCP_{ens} corresponding to an increase in the variance in the subtropical gyre.

4.4.5 Multiyear seasonal means of the overturning and gyre heat transport

To determine the role of seasonal means for the predictability of the overturning and gyre heat transport, I analyze the respective ACC for winter, spring, summer and autumn means in the following.

The overturning heat transport reveals a similar skill in the ACC of winter means as the ACC of yearly means in HIST_{ens} (Fig.4.17a). In the subtropical gyre, significant ACCs are limited to the first lead year, while in the subpolar gyre ACCs extend to lead year 5 between 40°N and 50°N. The variance (Fig.4.17c,d) shows that the overturning heat transport strongly dominates the total variance with a ratio of almost 1 in the subtropical gyre. In RCP_{ens} the predictability is almost lost for the ACC in the subtropical gyre (Fig.4.17e). The subpolar gyre does not indicate considerable changes in the ACC between HIST_{ens} to RCP_{ens} with predictable lead times of up to 4 years between 40°N and 50°N.

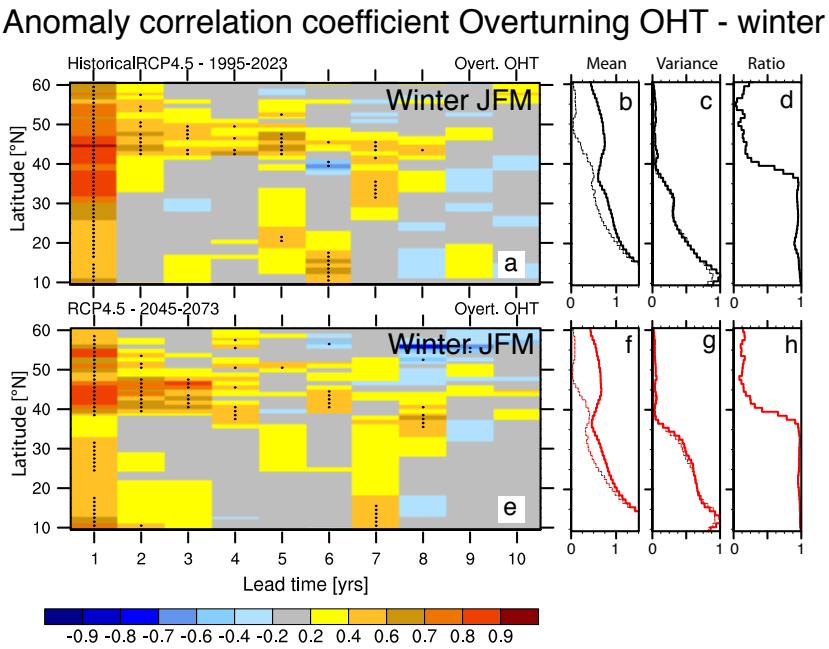

Figure 4.17: Anomaly correlation coefficient (ACC) of the overturning heat transport for winter means (JFM) for **(a)** the historical ensemble spanning 1995-2023 and **(e)** the future ensemble in RCP4.5 spanning 2045-2073. The panels show the ACC for lead times of 1 to 10 years plotted against latitude. The stippling indicates correlation coefficients significant at the 95% confidence level. **(b-d)** Historical simulation (reference run): **(b)** mean and **(c)** variance (scaled by the maximum of the total OHT variance between 10°N-60°N) of the total OHT (solid line) and the overturning heat transport (thin-dashed) and **(d)**the ratio of the overturning to the total OHT variance ($Var(H^{ov})/[Var(H^{total} - Cov(H^{gyre}, H^{ov})]$). **(f-h)** RCP4.5 (reference run): **(f)** mean and **(g)** variance (scaled by the maximum of the total OHT variance between 10°N-60°N) of the total OHT (solid line) and the overturning heat transport (thin-dashed) and **(h)** the ratio of the overturning to the total OHT variance.

For summer months, the overturning heat transport generally indicates low ACCs in the subtropical gyre similar to yearly means, and thus low predictability (Fig.4.18a-d). In the subtropical gyre, the predictability in HIST_{ens} is limited to the first lead year between 20°N to 30°N and 35°N to 40°N, but yields only correlations of about 0.5. Between 10°N to 30°N, significant correlations higher than 0.7 are found for lead year 1. Between 20°N-30°N significant ACCs larger than 0.5 occur up to lead year 5 in HIST_{ens} and up to lead lear 6 in RCP_{ens}, that might contribute to the re-emergence of skill in the yearly means of the overturning heat transport. In the subpolar gyre, the ACC is higher and reveals predictability up to lead year 3 at about 50°N.

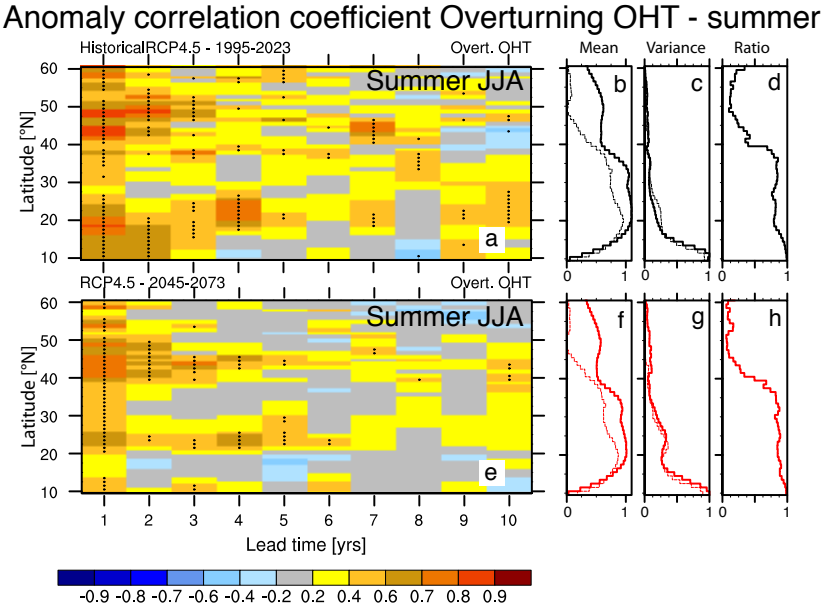

Figure 4.18: Anomaly correlation coefficient (ACC) of the overturning heat transport for summer means (JJA) for **(a)** the historical ensemble spanning 1995-2023 and **(e)** the future ensemble in RCP4.5 spanning 2045-2073. The panels show the ACC for lead times of 1 to 10 years plotted against latitude. The stippling indicates correlation coefficients significant at the 95% confidence level. **(b-d)** Historical simulation (reference run): **(b)** mean and **(c)** variance (scaled by the maximum of the total OHT variance between 10°N-60°N) of the total OHT (solid line) and the overturning heat transport (thin-dashed) and **(d)**the ratio of the overturning to the total OHT variance ($Var(H^{ov})/[Var(H^{total} - Cov(H^{gyre}, H^{ov})]$). **(f-h)** RCP4.5 (reference run): **(f)** mean and **(g)** variance (scaled by the maximum of the total OHT variance between 10°N-60°N) of the total OHT (solid line) and the overturning heat transport (thin-dashed) and **(h)** the ratio of the overturning to the total OHT variance.

In RCP_{ens} (Fig.4.18e-h), the ACC in the subtropical gyre is reduced, but at about 25°N predicable lead times up to 6 years emerge, similarly to the total OHT and in concert with an increase in the variance in the seasonal cycle. In the subpolar gyre, ACCs are mostly reduced. The predictability at 50°N is limited to 1-2 lead years, but in contrast longer predictable lead times up to 5 years emerge at about 45°N. The ACC in spring means also shows some skill in the subpolar gyre in HIST_{ens} and RCP_{ens}, while the ACC for autumn means shows little in HIST_{ens} and some predictability with correlations between 0.6 and 0.7 for lead years 1-2 between 40°N to 50°N in RCP_{ens} (Fig.4.21).

The gyre heat transport generally indicates little dependence on the season in both HIST_{ens} and RCP_{ens} (Fig.4.19-4.21). The gyre heat transport

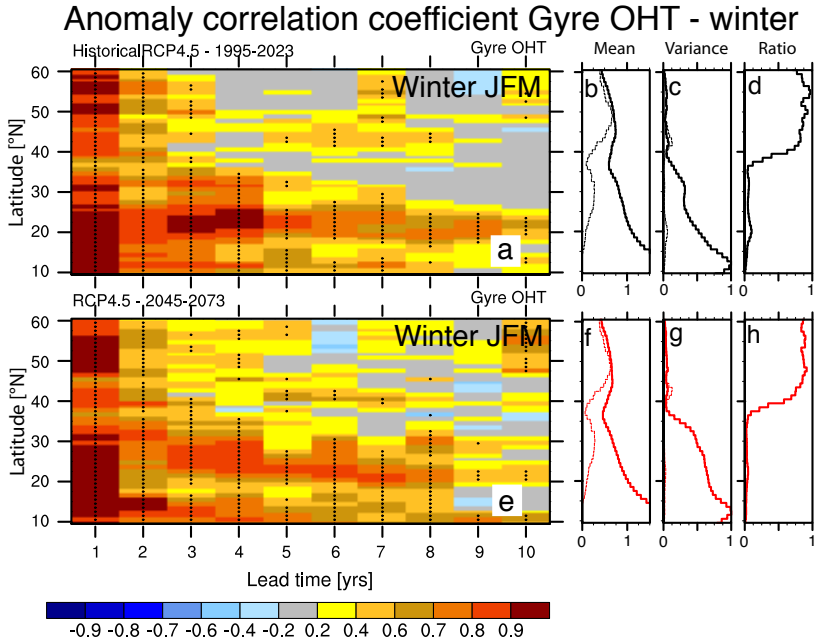

Figure 4.19: Anomaly correlation coefficient (ACC) of the gyre heat transport for winter means (JFM) for **(a)** the historical ensemble spanning 1995-2023 and **(e)** the future ensemble in RCP4.5 spanning 2045-2073. The panels show the ACC for lead times of 1 to 10 years plotted against latitude. The stippling indicates correlation coefficients significant at the 95% confidence level. **(b-d)** Historical simulation (reference run): **(b)** mean and **(c)** variance (scaled by the maximum of the total OHT variance between 10°N-60°N) of the total OHT (solid line) and the gyre heat transport (thin-dashed) and **(d)**the ratio of the gyre to the total OHT variance $(Var(H^{ov})/[Var(H^{total} - Cov(H^{gyre}, H^{ov})])$. **(f-h)** RCP4.5 (reference run): **(f)** mean and **(g)** variance (scaled by the maximum of the total OHT variance between 10°N-60°N) of the total OHT (solid line) and the gyre heat transport (thin-dashed) and **(h)** the ratio of the gyre to the total OHT variance.

(Fig.4.19) shows a similar predictability in the subtropical gyre for winter means as the ACC of yearly means (Fig.4.16). The fraction of the variance is close to zero in the subtropical gyre, suggesting a weak influence of the predictability in the gyre heat transport on the predictability of total OHT (Fig.4.19d). The subpolar gyre shows short predictable lead times in winter of only 3 years compared to yearly means, so that other seasons must contribute to the high predictability for later lead years. In RCP_{ens} the ACC does not change considerably for winter means, as the variance of the gyre heat transport (Fig.4.19e-h).

Similarly to the ACC of yearly means and winter means, high predictability is found in the subtropical gyre with predictable lead times up to 10 years in HIST_{ens} for all seasons (Fig.4.19-4.21). For the subpolar gyre predictable

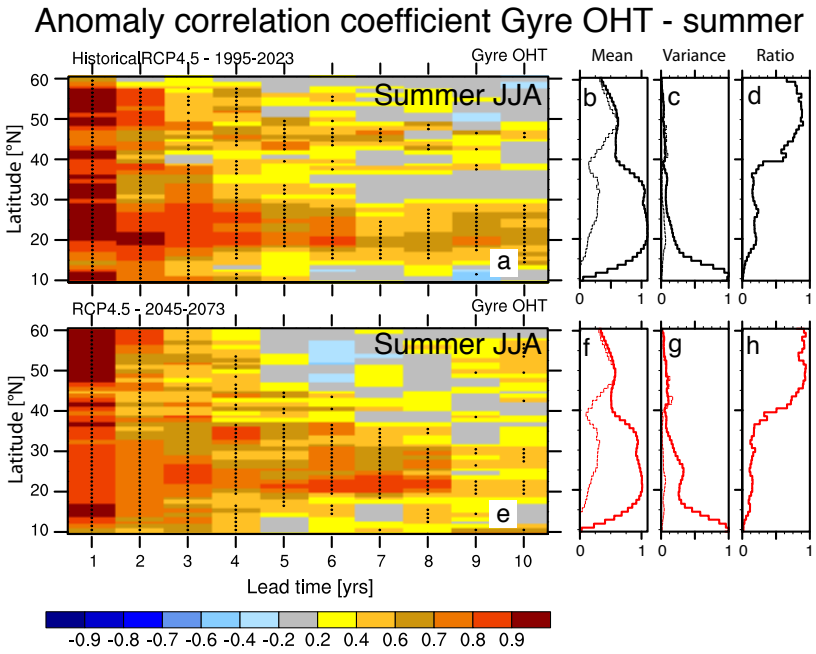

Figure 4.20: Anomaly correlation coefficient (ACC) of the gyre heat transport for summer means (JJA) for **(a)** the historical ensemble spanning 1995-2023 and **(e)** the future ensemble in RCP4.5 spanning 2045-2073. The panels show the ACC for lead times of 1 to 10 years plotted against latitude. The stippling indicates correlation coefficients significant at the 95% confidence level. **(b-d)** Historical simulation (reference run): **(b)** mean and **(c)** variance (scaled by the maximum of the total OHT variance between 10°N-60°N) of the total OHT (solid line) and the gyre heat transport (thin-dashed) and **(d)**the ratio of the gyre to the total OHT variance $(Var(H^{ov})/[Var(H^{total} - Cov(H^{gyre}, H^{ov})])$. **(f-h)** RCP4.5 (reference run): **(f)** mean and **(g)** variance (scaled by the maximum of the total OHT variance between 10°N-60°N) of the total OHT (solid line) and the gyre heat transport (thin-dashed) and **(h)** the ratio of the gyre to the total OHT variance.

lead times of summer means are longer than for winter mean ACCs, but similar to yearly mean ACCs in HIST_{ens}. In RCP_{ens}, the predictability is slightly reduced in summer, spring and autumn in the subtropical and subpolar gyre compared to HIST_{ens}. In the subtropical gyre, the ACC is lower and predictable lead times are shorter in RCP_{ens} than in HIST_{ens} in. Similarly, spring and autumn (Fig.4.21) indicate only small changes throughout the year in the gyre heat transport and little changes between HIST_{ens} and RCP_{ens}.

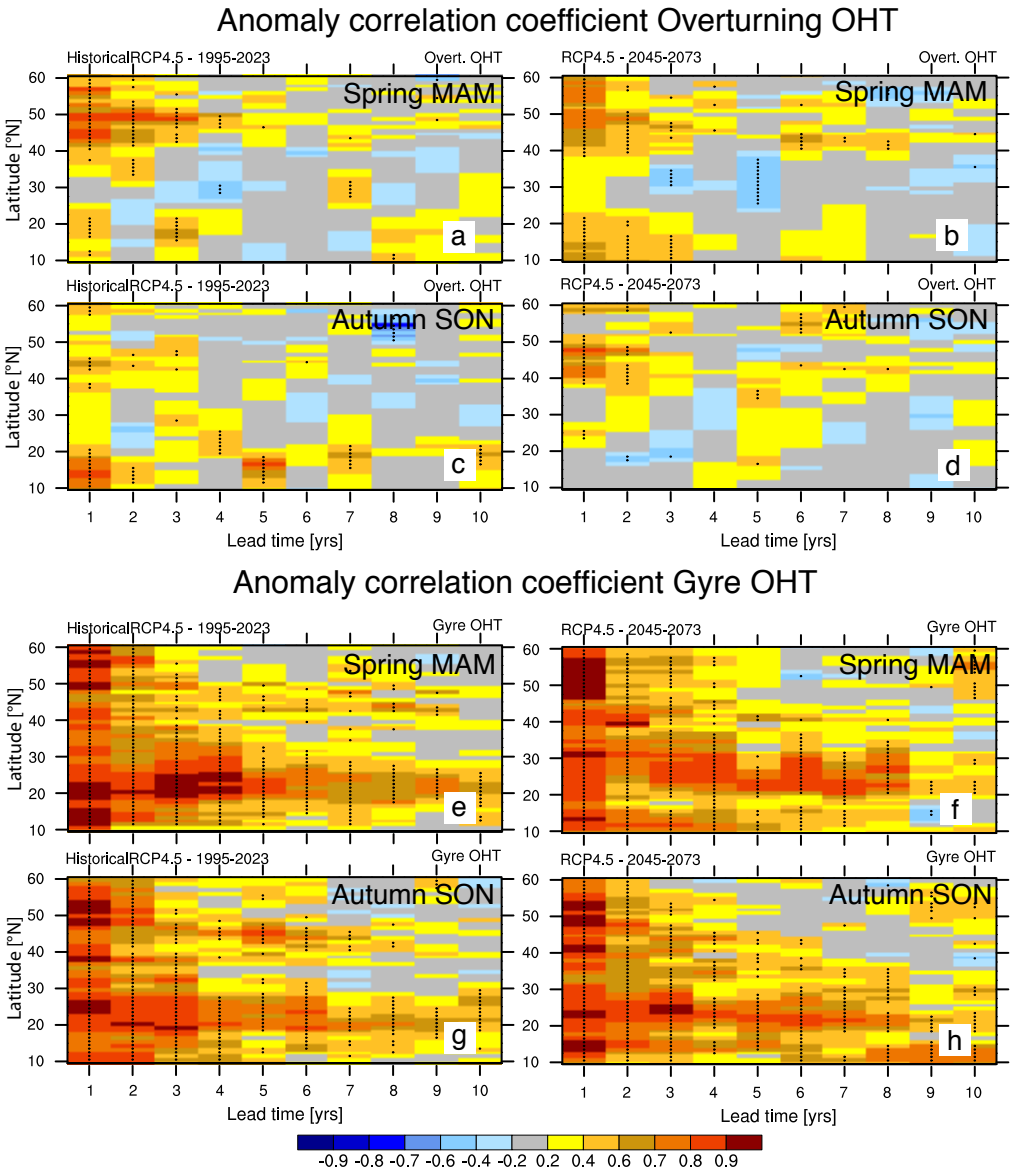

Figure 4.21: Anomaly correlation coefficient (ACC) of the overturning **(a-d)** and gyre heat transport **(e-h)** for spring (March-April-May) and autumn (September-October-November) means in the historical ensemble spanning 1995-2023 and the future ensemble in RCP4.5 spanning 2045-2073. The panels show the ACC for lead times of 1 to 10 years plotted against latitude. The stippling indicates correlation coefficients significant at the 95% confidence level.

4.5 Summary and Discussion

Summary

Two ensemble hindcast experiments for a present and a future climate state in MPI-ESM CMIP5 projections are investigated. Both, the present day ensemble HIST_{ens} and the future ensemble RCP_{ens} reveal changes in the potential predictability of the AMOC and of the OHT for the anomaly correlation coefficient (ACC) and for the reliability of the predictions until the middle of the 21st century.

(1) AMOC

For the AMOC, the predictability in the ACC and the reliability of the predictions are considerably reduced from HIST_{ens} to RCP_{ens}. The potential predictability of the AMOC in terms of the ACC in HIST_{ens} shows predictable lead times up to 10 years in the subtropical gyre and up to 4 years in the subpolar gyre. The structure of the predictability pattern is in agreement with the predictability found in other studies with higher skill in the subtropical gyre than in the subpolar gyre (Tiedje et al., 2012, Bellucci et al., 2013, Kröger et al., 2012), even if the separation of the ACCs between subtropical and subpolar gyre is relatively sharp in HIST_{ens} and the exact patterns of predictability differ between individual models (including coupled and ocean only simulations) and based on the used initialization technique.
Reliability diagrams and the Brier Skill Score reveal that predictions of the AMOC are overall more reliable in the subtropical gyre than in the subpolar gyre. Between HIST_{ens} and RCP_{ens}, the reliability is considerably reduced for yearly means and winter means. The analysis of the reliability of summer and winter means shows, that in particular summer means yield overall more reliable predictions in both HIST_{ens} and RCP_{ens}.
As also found in earlier studies (e.g., Matei et al., 2012a, Tiedje and Baehr, 2014), the AMOC's predictability is determined by the geostrophic transport

yielding long predictable lead times of up to 10 years in the subtropical gyre and up to 5 years in the subpolar gyre for the present climate state. The predictability of the AMOC and the geostrophic transport is dominated by the considerable predictability of summer means, while the geostrophic transport is additionally influenced by the predictability of spring means in the subtropical and subpolar gyre.
For the future climate state in RCP_{ens}, the long predictability of the AMOC and geostrophic transport is mostly lost and limited to about 2 years lead time at all latitudes in the North Atlantic. Considering seasonal means in RCP_{ens}, summer means reveal the strongest influence on changes in the predictability, while other seasons show an overall low predictability. The longest predictable lead times in the geostrophic transport of 4 years occur for spring means in the subpolar gyre for RCP_{ens}.

(2) OHT

The OHT shows a general increase in predictable lead times from $HIST_{ens}$ to RCP_{ens} in the ACC in both the subtropical and subpolar gyre even though the reliability is reduced from $HIST_{ens}$ to RCP_{ens}. The reliability of predictions of the OHT indicates higher skill in the subpolar gyre, with $HIST_{ens}$ showing higher predictability than RCP_{ens}. The reliability is in total higher for seasonal means of the OHT than for yearly means, with a reasonable sharpness for lead years 1 and 2-3. The ACC indicates generally higher predictability for yearly means, while amongst the multiyear seasonal means summer means dominate the predictability in the subtropical gyre and summer, winter and spring means contribute to predictability in the subpolar gyre.
The gyre heat transport shows particularly high skill in the subtropical gyre for all seasons and for both ensemble experiments $HIST_{ens}$ and RCP_{ens}. The predictability in the subpolar gyre is lower, but still all seasons exhibit significant ACCs up to 7 lead years, except of the winter means where significant ACCs are limited to 3 lead years. In the subpolar gyre, the ACC of the gyre heat transport can largely explain the predictability in the OHT

and changes from $HIST_{ens}$ to RCP_{ens}. The overturning heat transport generally indicates lower skill than the gyre heat transport, but explains the changes in the predictability in the subtropical gyre.
The variance of the overturning and gyre heat transport indicates that the variability in the total OHT is dominated by the gyre heat transport in the subpolar gyre in all seasons, while the variability in the subtropical gyre is dominated by the overturning heat transport. Transferring changes in the variance on the predictability by means of the PPP shows that regions with increased variance in RCP_{ens} compared to $HIST_{ens}$ generally indicate longer predictable lead times, while regions with decreased variance in RCP_{ens} compared to $HIST_{ens}$ indicate shorter predictable lead times in the ACC.
Similar to the AMOC, the OHT reveals comparable patterns of skill in the subtropical and subpolar gyre, although the predictive skill of the OHT in $HIST_{ens}$ is generally lower e.g. than for Tiedje et al. (2012). Likewise, the overturning heat transport indicates lower skill limited to 1 year of predictable lead time. In contrast, the gyre heat transport reveals surprisingly high skill in $HIST_{ens}$ compared to Tiedje et al. (2012).

Discussion

The changes in the potential predictability of the AMOC and the OHT between the present climate state represented by $HIST_{ens}$ and a future climate state represented by RCP_{ens} reveal changes in the overall predictability with shortened predictable lead times and at specific latitudes with a significant reduction in the predictable lead times and the anomaly correlation coefficient. The most prominent changes occur at latitudes where considerable changes in the seasonal cycle have been found in chapter 3.

The most significant changes in the predictability have been expected from chapter 3 at about 25°N, between 30°N and 40°N in the subtropical gyre and around 50°N in the subpolar gyre for the the AMOC and at 25°N, 30°N to 40°N in the subtropical gyre and between 40°N and 60°N in the subpolar

gyre for the OHT. The AMOC indicates exactly at these latitudes prominent changes in the ACCs from $HIST_{ens}$ to RCP_{ens}, with a decrease in predictable lead times around 25°N and around 50°N, as well as a decrease in significant ACCs between 35°N and 40°N for lead year 1.
Similarly, the skill in the ACC is reduced for the OHT around 25°N from $HIST_{ens}$ to RCP_{ens} and for lead year 1 between 30°N and 40°N. These changes result mostly from the overturning heat transport and are comparable to the ACC of the AMOC, suggesting a relation between AMOC and OHT predictability found in Tiedje and Baehr (2014) and similar mechanisms involved. In the subpolar gyre (40°N-60°N) where the peak-to-peak amplitude of the seasonal cycle is enhanced in the gyre heat transport in RCP4.5 and the variance of the OHT increases in RCP_{ens}, predictable lead times are extended from about 2 years to about 4 years in the OHT.
At these specific latitude bands, changes in the peak-to-peak amplitude occur, including changes in the variance of the seasonal cycle. The changes in the variance of the seasonal cycle contribute to changes in the total variance especially at these latitudes jointly with the overall changes in the variance found for the OHT, the overturning heat transport and the gyre heat transport. A more detailed analysis of the variance will be needed to clearly understand the impact of changes in the variance of the seasonal cycle on the predictability. Nevertheless, strong hints are given by the agreement of latitude bands that in particular the seasonal cycle peak-to-peak amplitude (and thus the variance) impacts the potential predictability of the AMOC and the OHT on inter-annual to decadal timescales.

For the the first time, the potential predictability of the AMOC and OHT is analyzed for yearly means together with multiyear seasonal means. The ACC of seasonal means is overall lower than the ACC of yearly means as also found for temperatures before (MacLeod et al., 2012). The predictability in the ACC for the AMOC results predominately from summer means, the predictability for the geostrophic transport results predominantly from summer and spring means. All seasons show an overall decrease in skill from $HIST_{ens}$ to RCP_{ens} in the AMOC and the geostrophic transport in concert with yearly means. The OHT similarly indicates a generally higher predictability and

longer predictable lead times for summer means, whereas high correlations are found in the first lead year for winter means. The first lead year of winter means generally indicates skillful ACCs which are thought to result from skill in the prediction of the wind for the first months after initialization.
Changes in the seasonal cycle emerge especially around 25°N, where a shift of the seasonal minimum and maximum of about 5 months is found in chapter 3. Significant predictable lead times of 4 years are found for yearly means of the total OHT in HIST_{ens}, but disappear for yearly means in RCP_{ens}. This pattern is not apparent in seasonal means in HIST_{ens}, but appears again for summer means in RCP_{ens}. A shift in the seasons of about half a year would suggest that in HIST_{ens} this pattern might appear for winter means, but could be blocked by the low skill in predicting winter, spring and autumn means. The predominance of potential predictability (in terms of the ACC) in summer and the overall lower skill for other seasons generally restricts conclusions concerning changes in the phase of the seasonal cycle on changes in the potential predictability of specific seasons.

Regarding the question whether the decadal predictions have sufficient reliability to provide useful information to users the reliability and Brier Skill Score has been analyzed for the AMOC and OHT for the first time here. Corti et al. (2012) have shown, that predictions of surface temperatures over the North Atlantic might exhibit some reliability. Here, I have shown, the HIST_{ens} indicates some reliability for the AMOC up to lead year 3 that is higher in the subtropical gyre, even after a linear trend is removed. The reliability of the AMOC in RCP_{ens} is generally low so that the predictions cannot be considered reliable. The reliability for winter and summer means of the AMOC providing reliable predictions up to lead year 5 is comparable in HIST_{ens} to yearly means. In RCP_{ens} predictions of winter means do not reveal any reliability in contrast to summer means, where predictions of the AMOC are reliable for lead year 1-3.
The OHT also exhibits some reliability in the subtropical and subpolar gyre, whereas the reliable predictions are limited to HIST_{ens} for lead years 1-3. The reliability of OHT predictions in the subpolar is generally higher and also indicates some reliability in RCP_{ens}. For individual seasons, reliable forecasts

are also found in RCP_{ens} for lead years 1-3.
Overall, the reliability analysis reveals, that the skill in the AMOC is reduced in the subtropical and subpolar gyre from $HIST_{ens}$ to RCP_{ens}. But, the applicability of the reliability analysis for real predictions of the AMOC and OHT is analogously limited as for deterministic measures (e.g, Matei et al., 2012a, Vecchi et al., 2012), since observations of the AMOC and OHT are still relatively short (Smeed et al., 2015) and need further decades and a broader ranges of latitudes to allow for a sensible evaluation of the reliability of the AMOC and the OHT.

4.6 Conclusions

Based on the analysis of the potential predictability of the AMOC and the OHT for a present climate state in the CMIP5 historical simulation extended with RCP4.5 (1995-2023) and a future climate state in RCP4.5 (2045-2073) I conclude:

- The AMOC exhibits latitude-dependent potential predictability for the present climate state in $HIST_{ens}$ with predictable lead times up to 4 years, that decrease in the future ensemble RCP_{ens} to 2 years at all latitudes. The skill in the anomaly correlation coefficient results mostly from the predictability of summer months and largely from the high skill in predicting the geostrophic transport.

- For the present climate, the ACC of the AMOC and the OHT reveals similar latitudes with high skill (around 25°N and 40°N to 60°N). In contrast to the AMOC, the OHT reveals increased predictable lead times of 4 years in the subpolar gyre in RCP_{ens}, but a consistant reduction in predictable lead times to to 2 years at 25°N in the subtropical gyre in RCP_{ens}.

- Considerable changes in the ACC are found around 25°N and in the subpolar gyre between 40°N to 60°N for the AMOC and the OHT from

HIST_{ens} to RCP_{ens} in agreement with latitudes that reveal prominent changes in the AMOC and the OHT seasonal cycle.

- The skill in the OHT cannot be explained explicitly by either the overturning heat transport or the gyre heat transport. The overturning heat transport reveals generally lower skill in the ACC, while the gyre heat transport reveals notably high skill in the ACC in both the subtropical and subpolar gyre and for HIST_{ens} and RCP_{ens}.

- From the variance of the gyre and overturning heat transport in HIST_{ens} and RCP_{ens} follows that the gyre heat transport dominates the predictability and its changes in the subpolar gyre, while the overturning heat transport dominates the predictability and its changes in the subtropical gyre.

- The reliability analysis suggests changes in concert with the ACC for the AMOC and the OHT in the subtropical and subpolar gyre. Predictions of seasonal means indicate a higher reliability than predictions of yearly means. Generally, predictions of the OHT are more reliable than predictions of the AMOC. For both, the AMOC and the OHT predictions are more reliable in HIST_{ens} than in RCP_{ens}.

5 Summary and Conclusions

To investigate the effect of global warming on the North Atlantic ocean circulation and on the potential predictability of the Atlantic meridional overturning circulation (AMOC) and the Atlantic meridional heat transport (OHT) I have first analyzed changes in the AMOC and OHT with a focus on their seasonal cycles in the Max-Planck-Institute Earth System Model (MPI-ESM). Subsequently, I have analyzed changes in the potential predictability of the AMOC and the OHT between a present climate state in the Coupled Model Intercomparison Project phase 5 (CMIP5) historical simulation (HIST_{ens}) and a projected future climate state in RCP4.5 (RCP_{ens}) that might result from changes in the seasonal cycle of the AMOC and the OHT.

All results are based on climate simulations with the Max-Planck-Institute Earth System Model. The analysis of changes in the AMOC and OHT seasonal cycle is based on the MPI-ESM CMIP5 climate projections with all limitations and uncertainties inherent in climate projections (e.g., Knutti and Sedláček, 2013). Yet, the analysis in this thesis is performed in one single ensemble member of the CMIP5 projections in MPI-ESM and thus ensures a physically consistent framework for the analysis. Even though, results might differ in other models contributing CMIP5.
For the predictability analysis, two ensemble experiments are performed in MPI-ESM. Because the decadal predictability of a future climate can only be studied in terms of potential predictability, both ensemble experiments are based on "uninitialized" simulations from CMIP5 to ensure comparability of the two experiments. Using the anomaly correlation coefficient (ACC) together with reliability diagrams and the Brier Skill Score (BSS), the ensem-

ble means are validated against the same respective CMIP5 simulation in the sense of a "perfect model" framework. Thus, the results of the predictability analysis rather give an upper limit of predictability given a "perfect model world" and near perfect knowledge of the initial conditions in the ocean and the atmosphere that will never be achieved in the real world. Nevertheless, the use of a coupled comprehensive climate model enables us to include effects from the ocean, atmosphere, sea ice and land into the analysis. Further, the analysis has the advantage of a consistent experimental setup for both (1) the analysis of changes in the seasonal variability of the AMOC and the OHT and (2) the predictability analysis with respect to initialization and consistency with the reference simulation.

In the following, I will summarize the main results and conclude this thesis by answering the questions raised in the introduction.

Changes in the seasonal variability of the Atlantic meridional overturning circulation and the meridional heat transport in a future climate

• *What changes do emerge in the mean state of the North Atlantic ocean circulation, the AMOC and the OHT due to global warming in the MPI-ESM climate projections?*

The North Atlantic Ocean reveals a considerable warming of sea surface temperatures under global warming. The strongest warming occurs in RCP8.5 until the 23rd century in polar regions and a less intense warming in the subpolar gyre. Surface salinities reveal a freshening in the subpolar gyre, and an increase of salinity in the subtropical gyre. This implies changes in the North Atlantic gyre circulation which is shifted northward by about 5 degrees in RCP8.5 in concert with a northward shift in the surface winds (chapter 2).
Changes in the ocean circulation impact the AMOC and OHT (chapter 2). Both show considerable changes between the present climate state in HIST_{ens} and a future climate state in RCP_{ens}. The AMOC shows a

weakening by about 50% in the North Atlantic in RCP8.5 until the 23rd century resulting from a weakening of the geostrophic transport (AMOC-Ekman). The OHT shows a 30 to 50% decline in the time-mean that results from a weakening of the overturning heat transport in the subtropical gyre and a weakening of both, the overturning and gyre heat transport in the subpolar gyre (section 2.1). A decomposition of the OHT in density coordinates reveals a considerable reduction in the surface and intermediate layers, and a further reduction in the OHT related to the formation of the North Atlantic Deep Water (NADW) that is almost absent in RCP8.5 in the 23rd century (section 2.1). An equivalent finding is obtained from the OHT decomposition based on a heat function in potential temperature coordinates (section 2.2).
For near-term changes until the middle of the 21st century, the RCP8.5 scenario in MPI-ESM indicates a global mean temperature increase by more than 2°C and a reduction in the OHT and AMOC by 10-20% compared to the historical simulation. Similarly, the RCP4.5 scenario indicates a global temperature increase of almost 2°C and a reduction of the OHT and AMOC by about 10% (chapter 3).

• *Do projected changes in the mean state of the North Atlantic ocean circulation imply changes in the seasonal cycle of the OHT until the end of the 23rd century in the MPI-ESM climate projections?*

In concert with the decline, the OHT seasonal cycle shows shifts in time (1 to 6 months, depending on latitude and season) and space (5° northward, of the seasonal cycle pattern) for long-term changes between the present climate state in the historical simulation and the 23rd century in RCP8.5 (chapter 2).
The OHT seasonal cycle reveals changes in both the subtropical and subpolar gyre. These changes stem from a latitude-dependent altered seasonal cycle and a northward shift by about 5 degrees in the atmospheric Hadley circulation and resulting changes in the surface winds. These lead to a temporal shift by 1 to 5 months in the seasonal cycle of the Ekman

heat transport and the overturning heat transport (section 2.1). The vertical structure of the OHT reveals that in tropical and subtropical North Atlantic, the OHT seasonal cycle is mostly driven and mostly changed in the surface and intermediate layers where the wind acts as the dominant direct driver of the seasonal variability and leads to temporal shifts from 1 to 6 months. In the subpolar North Atlantic, the process of NADW formation contributes to the seasonal cycle in the historical simulation, while this contribution is significantly reduced in RCP8.5 until the 23rd century due to a reduction in the NADW formation (section 2.1).
The vertical decomposition of the OHT seasonal cycle in potential temperature coordinates (section 2.2) indicates that the mixed (residual) circulation – that also determines the mean OHT – drives a large fraction of changes in the OHT seasonal cycle. Further changes occur in the wind-driven surface cell that indicates an intensified seasonal cycle and in a cold cell related to the NADW formation where the absent NADW formation extinguishes the seasonal cycle.

• *Are changes in the seasonal cycle already noticeable in the near future in the middle of the 21st century?*

Changes in the seasonal cycle of the AMOC and the OHT already emerge in the middle of the 21st century in RCP4.5 and RCP8.5 with latitude-dependent temporal shifts in the seasonal cycle and changes in the seasonal peak-to-peak amplitude (chapter 3). Between RCP4.5 and RCP8.5, changes in the seasonal cycle show a similar dependence on latitude with slightly larger adjustments in RCP8.5.
For the seasonal amplitude of the AMOC (chapter 3) changes occur in both the subtropical and subpolar gyre. The largest changes occur in the subtropical gyre between 25°N and 35°N with reduction in the seasonal amplitude and between 35°N and 50°N with an increase in the seasonal amplitude between the present climate state and the middle of the 21st century. The rest subpolar gyre also indicates a general reduction in the seasonal amplitude. These changes predominantly result from changes in the Ekman transport

seasonal cycle. Changes in the seasonal cycle of the geostrophic transport are weaker, but also emerge in the subtropical and subpolar gyre. The minima and maxima in the AMOC seasonal cycle are also shifted between the present climate state and the middle of the 21st century, especially between 25°N and 30°N in the subtropical gyre and between 35°N and 50°N from the subtropical to the subpolar gyre.

The seasonal cycle of the OHT (chapter 3) reveals a decreased seasonal peak-to-peak amplitude in the subtropical gyre that results from the seasonal cycle of the overturning heat transport, in particular between 20°N and about 30°N and an increase in the peak-to-peak amplitude between about 30°N and 40°N. Changes in the seasonal cycle of the gyre heat transport become important in the subpolar gyre where the seasonal peak-to-peak amplitude is increased at most latitudes between 35°N and 60°N in the subtropical and the subpolar gyre between the present climate state and the middle of the 21st century. Only around 50°N, the seasonal amplitude is considerably reduced. Overall the OHT seasonal minima and maxima are shifted at the latitudes where the amplitude reveals the largest shifts in the subtropical gyre. Temporal shifts up to 5 months occur in particular between 20°N and about 30°N and about 30°N to 40°N in the subtropical gyre, and between 45°N and 55°N in the subpolar gyre. These latitude bands with largest shifts in the seasonal phase and amplitude might lead to considerable changes in the potential predictability of the AMOC and OHT (chapter 4).

The influence of the AMOC and OHT especially on the European climate is still under discussion (e.g., Riser and Lozier, 2013). The changes in the seasonal cycle of the AMOC and the OHT imply changes in the seasonally dependent heat transports into the North Atlantic that might also affect the (seasonal) variability of the ocean heat content, surface temperatures or surface heat fluxes. Via this interaction at the surface, the AMOC and OHT (seasonal) variability is linked to the European climate, although exact mechanism are not yet clear. Thus, the changes in the AMOC and OHT seasonal cycle motivate to advance the understanding of the relation between the North Atlantic ocean circulation and the European climate. Future research might focus on the understanding of the specific role of the changes in the seasonal cycle found in this study on potential climate impacts on the

European continent.

Potential predictability of the Atlantic meridional overturning circulation and the Atlantic meridional heat transport

• *Does the potential predictability of the AMOC and the OHT change between the present climate state and a projected future climate state?*

The potential predictability of the AMOC and OHT is found to change in a future climate state in RCP4.5 (RCP_{ens}, chapter 4). The AMOC indicates a latitude-dependent potential skill in the ACC for the present climate state ($HIST_{ens}$) with up to 4 years. Predictable lead times in the ACC are reduced to 2 years at all latitudes for the AMOC under global warming in RCP_{ens}. Skillfull correlations in the AMOC are related to the geostrophic transport that also shows a considerable decrease in predictable lead times in RCP_{ens} compared to $HIST_{ens}$.
The OHT shows higher skill in the subpolar North Atlantic than in the subtropical North Atlantic. In contrast to the AMOC, the OHT shows an increase in predictable lead times in the subpolar gyre from 2-3 years to 4-5 years, but also a decrease in the subtropical gyre from up to 4 years in $HIST_{ens}$ to 2 years in RCP_{ens}. Changes in the predictability of the OHT are dominated by the gyre heat transport in the subpolar gyre and by both overturning heat transport and gyre heat transport in the subtropical gyre.
The reliability and Brier Skill Score of decadal predictions of the AMOC and OHT are considerably reduced in a future climate in RCP_{ens} compared to $HIST_{ens}$ in the subtropical and subpolar gyre. For the OHT, this is in contrast to the ACC that indicates higher skill in the subpolar gyre in RCP_{ens}. The considerable reduction in the reliability, making the prediction unreliable, questions whether the prediction is still potentially useful. Although the exact reason for the loss in reliability is not studied further in this thesis, this fact might demonstrate the need to further improve ensemble generation techniques and methods used in decadal prediction, in particular if real world predictability might weaken similarly.

• *Is there an impact of changes in the seasonal cycle on the potential predictability of the AMOC and OHT and do specific latitudes show more prominent changes than others?*

In the subtropical gyre, latitudes of high predictability agree for ACCs of the AMOC and the OHT in the present climate state ($HIST_{ens}$, chapter 4). Predictable lead times of up to 10 years in the AMOC and up to 4 years in the OHT emerge between 20°N and 30°N. In that latitude band, correlations are reduced and predictable lead times are shortened to 2 years in RCP_{ens} for both the AMOC and the OHT in accordance with latitudes where prominent changes in the seasonal cycle occur and in particular the variance of the seasonal cycle is reduced (chapter 3). This suggests that changes in the seasonal cycle can impact the potential predictability of the AMOC and the OHT.

In the AMOC the peak-to-peak amplitude is reduced suggesting a reduction in the variance of the AMOC. The reduction in the variance suggests a reduction of potential predictability. In concert, the OHT shows a decrease in the peak-to-peak amplitude between 20°N and 30°N together with a decrease in the variance. The ACC of the OHT is also reduced between 20°N and 30°N (chapter 4). Exactly here, the OHT indicates the largest temporal shift in the seasonal maxima from the present climate state to a future climate state (chapter 3), so that the reduction in ACC might be related to a considerable temporal shift and a reduction in variance in the OHT seasonal cycle.

In the subpolar gyre, the predictable lead times are uniformly reduced for the AMOC following the reduction in the seasonal amplitude in the subpolar North Atlantic. The potential predictability of the OHT is determined by the gyre heat transport. The ACC of the gyre heat transport shows an increase of predictable lead times in the subpolar gyre following the overall increase in the seasonal peak-to-peak amplitude and accordingly in the variance of the gyre heat transport at most latitudes in the subpolar gyre. Hence, the increase in predictable lead times in the ACC of gyre heat transport lead to increased predictable lead times in the ACC of the OHT in the subpolar gyre.

Overall, the AMOC and OHT indicate latitudes with prominent changes in the predictability. In particular between 20°N and 30°N in the subtropical gyre, considerable changes occur in the predictable lead times of the AMOC and the OHT between HIST_{ens} and RCP_{ens}. These latitudes refer to latitudes bands in the subtropical gyre with considerable changes in the seasonal cycle.

• *Do changes in the seasonal cycle project onto the potential predictability of multiyear seasonal means of the AMOC and the OHT?*

For multi-year seasonal means, the potential predictability is analyzed using the ACC and reliability diagram with the Brier Skill Score for winter and summer means. Overall, the potential predictability of the AMOC of winter means, spring means and autumn means is low. The potential predictability of the yearly mean AMOC is dominated by summer means. For summer means, the skill is reduced in RCP_{ens} compared to HIST_{ens} in the subtropical and subpolar gyre, as for yearly means. The predominance of skill in summer means and the low skill in the remaining seasons in ACC limit a noticeable impact of a potential shift in the seasonal cycle on the ACC of multiyear seasonal means. This applies in particular to the low ACCs in winter means, spring means and autumn means, that limit a clear detection of a potential impact of changes in the seasonal cycle.
For the OHT, the ACC of yearly means is similarly characterized by the predictability of summer means which shows an increase in predictable lead times in the future ensemble RCP_{ens}. Additionally, spring means yield some predictability in the subpolar gyre in RCP_{ens}. Only summer means show potential predictability for latitudes between 25°N and 30°N up to 5 years in RCP_{ens}. Between 25°N and 30°N, potential predictability is also found for yearly means in HIST_{ens}, but potential predictability is considerably reduced for yearly means in RCP_{ens}. This reveals, that some predictability remains between 25°N and 30°N for summer means in RCP_{ens}, although the seasonal cycle changes notably at these latitudes.

The results demonstrate the need to foster further understanding and devel-

opment of techniques used in decadal prediction. With the methodologies (ACC and reliability) used in this study and commonly used in decadal prediction, skill in predicting the AMOC and OHT is mostly lost under future climate due to changes in the variance of the yearly mean AMOC and OHT as well as changes in the variance of the seasonal cycle at specific latitudes. This is in agreement with conceptual studies of potential predictability (e.g., Boer, 2009). Whether other metrics or an improved initialization of the hindcasts can yield more reliable predictions and a better potential predictability under future climate conditions is unclear.

Whether this result can directly be transferred to "real world" predictability can – of course – be questioned. But since the perfect model predictability generally gives an upper limit of predictability, an albeit higher reduction in predictability and predictive skill could potentially result from global warming for "real world" predictions. The results motivate to conduct further research of changes in the potential predictability under global warming, e.g. for relevant climate parameters that reveal a more direct connection to the North American and European climate such as surface temperatures and heat fluxes or precipitation and their impacts in individual seasons.

6 Bibliography

Andrews, D. G. (1983). A finite-amplitude Eliassen-Palm theorem in isentropic coordinates. *Journal of the Atmospheric Sciences*, **40** (8), 1877–1883.

Baehr, J. and Piontek, R. (2013). Ensemble initialization of the oceanic component of a coupled model through bred vectors at seasonal-to-interannual time scales. *Geoscientific Model Development Discussions*, **6**, 5189–5214.

Balan Sarojini, B., Gregory, J. M., Tailleux, R., Bigg, G. R., Blaker, A. T., Cameron, D. R., Edwards, N. R., Megann, A. P., Shaffrey, L. C., and Sinha, B. (2011). High frequency variability of the Atlantic meridional overturning circulation. *Ocean Science*, **7** (4), 471–486.

Barrier, N., Cassou, C., Deshayes, J., and Treguier, A.-M. (2014). Response of North Atlantic Ocean Circulation to Atmospheric Weather Regimes. *Journal of Physical Oceanography*, **44** (1), 179–201.

Bellucci, A., Gualdi, S., Masina, S., Storto, A., Scoccimarro, E., Cagnazzo, C., Fogli, P., Manzini, E., and Navarra, A. (2013). Decadal climate predictions with a coupled OAGCM initialized with oceanic reanalyses. *Climate dynamics*, **40** (5-6), 1483–1497.

Bintanja, R. and Van der Linden, E. (2013). The changing seasonal climate in the Arctic. *Scientific reports*, **3**.

Boccaletti, G., Ferrari, R., Adcroft, A., Ferreira, D., and Marshall, J. (2005). The vertical structure of ocean heat transport. *Geophysical Research Letters*, **32** (10).

Boer, G. (2009). Changes in interannual variability and decadal potential predictability under global warming. *Journal of Climate*, **22** (11), 3098–3109.

Boer, G. J. (2004). Long time-scale potential predictability in an ensemble of coupled climate models. *Climate Dynamics*, **23** (1), 29–44.

Böning, C., Dieterich, C., Barnier, B., and Jia, Y. (2001). Seasonal cycle of meridional heat transport in the subtropical North Atlantic: A model intercomparison in relation to observations near 25°N. *Progress in Oceanography*, **48(2)**, 231–253.

Böning, C. and Hermann, P. (1994). Annual cycle of poleward heat transport in the ocean: Results from high-resolution modelling of the North and Equatorial Atlantic. *Journal of Physical Oceanography*, **24(10)**, 91–107.

Brier, G. W. (1950). Verification of forecasts expressed in terms of probability. *Monthly weather review*, **78** (1), 1–3.

Bryan, K. (1962). Measurements of meridional heat transport by ocean currents. *Journal of Geophysical Research*, **67** (9), 3403–3414.

Bryan, K. (1982a). Poleward heat transport by the ocean: observations and models. *Annual Review of Earth and Planetary Sciences*, **10**, 15.

Bryan, K. (1982b). Seasonal variation in meridional overturning and poleward heat transport in the Atlantic and Pacific Oceans: A model study. *J. Mar. Res.*, **40**, 39–53.

Bryan, K. and Sarmiento, J. L. (1985). Modeling ocean circulation. *Advances in geophysics*, **28**, 433–459.

Bryden, H. and Imawaki, S. (2001). Ocean heat transport. In G. Siedler, J. Church, and J. Gould (Eds.), *Ocean circulation and climate: observing and modelling the global ocean, volume 77 of International Geophysics Series, chapter 6.1*, volume 77 (pp. 455–474). San Francisco: Academic Press.

Bryden, H. L. (1993). Ocean heat transport across 24°N latitude. *Interactions Between Global Climate Subsystems the Legacy of Hann*, , 65–75.

Butler, A. H., Thompson, D. W., and Heikes, R. (2010). The Steady-State Atmospheric Circulation Response to Climate Changelike Thermal Forcings in a Simple General Circulation Model. *Journal of Climate*, **23** (13), 3474–3496.

Cabanes, C., Lee, T., and Fu, L. (2008). Mechanisms of Interannual Variations of the Meridional Overturning Circulation of the North Atlantic Ocean. *Journal of Physical Oceanography*, **38(2)**.

Carton, J. A., Ding, Y., and Arrigo, K. R. (2015). The seasonal cycle of the Arctic Ocean under climate change. *Geophysical Research Letters*, .

Chang, E. K., Guo, Y., and Xia, X. (2012). CMIP5 multimodel ensemble projection of storm track change under global warming. *Journal of Geophysical Research: Atmospheres (1984–2012)*, **117** (D23).

Cheng, W., Chiang, J., and Zhang, D. (2013). Atlantic Meridional Overturning Circulation (AMOC) in CMIP5 Models: RCP and Historical Simulations. *Journal of Climate*, **26(18)**.

Chidichimo, M., Kanzow, T., Cunningham, S., Johns, W., and Marotzke, J. (2010). The contribution of eastern-boundary density variations to the Atlantic meridional overturning circulation at 26.5°N. *Ocean Science*, **6** (2), 475–490.

Christensen, J., Krishna Kumar, K., Aldrian, E., An, S.-I., Cavalcanti, I., de Castro, M., Dong, W., Goswami, P., Hall, A., Kanyanga, J., Kitoh, A., Kossin, J., Lau, N.-C., Renwick, J., Stephenson, D., S.-P., X., and Zhou, T. (2013). Climate Phenomena and their Relevance for Future Regional Climate Change. In T. Stocker, D. Qin, G.-K. Plattner, M. Tignor, S. Allen, J. Boschung, A. Nauels, Y. Xia, B. V., and P. Midgley (Eds.), *Climate Change 2013: The Physical Science Basis. Contribution of Working Group I to the Fifth Assessment Report of the Intergovernmental Panel on Climate Change*. Cambridge, United Kingdom and New York, NY, USA: Cambridge University Press.

Collins, M. (2002). Climate predictability on interannual to decadal time scales: the initial value problem. *Climate Dynamics*, **19** (8), 671–692.

Collins, M. and Allen, M. R. (2002). Assessing the relative roles of initial and boundary conditions in interannual to decadal climate predictability. *Journal of Climate*, **15** (21), 3104–3109.

Collins, M., Botzet, M., Carril, A., Drange, H., Jouzeau, A., Latif, M., Masina, S., Otteraa, O., Pohlmann, H., Sorteberg, A., et al. (2006). Interannual to decadal climate predictability in the North Atlantic: a multimodel-ensemble study. *Journal of climate*, **19** (7), 1195–1203.

Collins, M. and Sinha, B. (2003). Predictability of decadal variations in the thermohaline circulation and climate. *Geophysical Research Letters*, **30** (6).

Corti, S., Weisheimer, A., Palmer, T., Doblas-Reyes, F., and Magnusson, L. (2012). Reliability of decadal predictions. *Geophysical Research Letters*, **39** (21).

Czaja, A. and Frankignoul, C. (2002). Observed impact of Atlantic SST anomalies on the North Atlantic Oscillation. *Journal of Climate*, **15** (6), 606–623.

Czaja, A., Frankignoul, C., et al. (1999). Influence of the North Atlantic SST on the atmospheric circulation. *Geophysical Research Letters*, **26** (19), 2969–2972.

Delworth, T. L. and Greatbatch, R. J. (2000). Multidecadal thermohaline circulation variability driven by atmospheric surface flux forcing. *Journal of Climate*, **13** (9), 1481–1495.

Dong, B. and Sutton, R. (2002). Variability in North Atlantic heat content and heat transport in a coupled ocean–atmosphere GCM. *Climate dynamics*, **19** (5-6), 485–497.

Dong, B. and Sutton, R. T. (2003). Variability of Atlantic Ocean heat transport and its effects on the atmosphere. *Annals of Geophysics*, .

Dong, S., Hautala, S. L., and Kelly, K. A. (2007). Interannual Variations in Upper-Ocean Heat Content and Heat Transport Convergence in the Western North Atlantic. *Journal of Physical Oceanography*, **37** (11).

Donohoe, A. and Battisti, D. S. (2013). The seasonal cycle of atmospheric heating and temperature. *Journal of Climate*, **26** (14), 4962–4980.

Drijfhout, S., Van Oldenborgh, G. J., and Cimatoribus, A. (2012). Is a decline of AMOC causing the warming hole above the North Atlantic in observed and modeled warming patterns? *Journal of Climate*, **25** (24).

Dwyer, J. G., Biasutti, M., and Sobel, A. H. (2012). Projected changes in the seasonal cycle of surface temperature. *Journal of Climate*, **25** (18), 6359–6374.

Dwyer, J. G., Biasutti, M., and Sobel, A. H. (2014). The Effect of Greenhouse-Gas-Induced Changes in SST on the Annual Cycle of Zonal Mean Tropical Precipitation. *Journal of Climate*, (2014).

Eden, C. and Jung, T. (2001). North Atlantic interdecadal variability: oceanic response to the North Atlantic Oscillation (1865-1997). *Journal of Climate*, **14** (5), 676–691.

Eden, C. and Willebrand, J. (2001). Mechanism of interannual to decadal variability of the North Atlantic circulation. *Journal of Climate*, **14** (10), 2266–2280.

Enfield, D. B., Mestas-Nunez, A. M., Trimble, P. J., et al. (2001). The Atlantic multidecadal oscillation and its relation to rainfall and river flows in the continental U. S. *Geophysical Research Letters*, **28** (10), 2077–2080.

Ferrari, R. and Ferreira, D. (2011). What processes drive the ocean heat transport? *Ocean Modelling*, **38** (3), 171–186.

Fischer, M., Domeisen, D., Müller, W. A., and Baehr, J. (2015). The Atlantic meridional heat transport seasonal cycle in a MPI-ESM climate projection. *submitted to Journal of Climate*, .

Frankignoul, C., Gastineau, G., and Kwon, Y.-O. (2013). The Influence of the AMOC Variability on the Atmosphere in CCSM3. *Journal of Climate*, **26** (24), 9774–9790.

Ganachaud, A. and Wunsch, C. (2000). Improved estimates of global ocean circulation, heat transport and mixing from hydrographic data. *Nature*, **408(6811)**, 453–457.

Ganachaud, A. and Wunsch, C. (2003). Large-scale ocean heat and freshwater transports during the World Ocean Circulation Experiment. *Journal of Climate*, **16(4)**, 696–705.

Gangstø, R., Weigel, A. P., Liniger, M. A., and Appenzeller, C. (2013). Methodological aspects of the validation of decadal predictions. *Clim. Res*, **55** (3), 181–200.

Gastineau, G., D'Andrea, F., and Frankignoul, C. (2013). Atmospheric response to the North Atlantic Ocean variability on seasonal to decadal time scales. *Climate dynamics*, **40** (9-10), 2311–2330.

Gastineau, G. and Frankignoul, C. (2015). Influence of the North Atlantic SST Variability on the Atmospheric Circulation during the Twentieth Century. *Journal of Climate*, **28** (4), 1396–1416.

Goddard, L., Hurrell, J. W., Kirtman, B. P., Murphy, J., Stockdale, T., and Vera, C. (2012). Two time scales for the price of one (almost). *Bulletin of the American Meteorological Society*, **93** (5), 621–629.

Goddard, L., Kumar, A., Solomon, A., Smith, D., Boer, G., Gonzalez, P., Kharin, V., Merryfield, W., Deser, C., Mason, S. J., et al. (2013). A verification framework for interannual-to-decadal predictions experiments. *Climate Dynamics*, **40** (1-2), 245–272.

Gregory, J., Dixon, K., Stouffer, R., Weaver, A., Driesschaert, E., Eby, M., Fichefet, T., Hasumi, H., Hu, A., Jungclaus, J., et al. (2005). A model intercomparison of changes in the Atlantic thermohaline circulation in response to increasing atmospheric CO2 concentration. *Geophysical Research Letters*, **32** (12).

Gregory, J. M. and Tailleux, R. (2011). Kinetic energy analysis of the response of the Atlantic meridional overturning circulation to CO2-forced climate change. *Climate dynamics*, **37** (5-6), 893–914.

Griffies, S. M. and Bryan, K. (1997). Predictability of North Atlantic multi-decadal climate variability. *Science*, **275** (5297), 181–184.

Grist, J. P., Josey, S. A., Marsh, R., Good, S. A., Coward, A. C., De Cuevas, B. A., Alderson, S. G., New, A. L., and Madec, G. (2010). The roles of surface heat flux and ocean heat transport convergence in determining Atlantic Ocean temperature variability. *Ocean dynamics*, **60** (4), 771–790.

Hall, M. and Bryden, H. (1982). Direct estimates and mechanisms of ocean heat transport. *Deep Sea Research Part A. Oceanographic Research Papers*, **29(3)**, 339–359.

Hand, R., Keenlyside, N., Omrani, N.-E., and Latif, M. (2014). Simulated response to inter-annual SST variations in the Gulf Stream region. *Climate Dynamics*, **42** (3-4), 715–731.

Hansen, J., Ruedy, R., Sato, M., and Lo, K. (2010). Global surface temperature change. *Reviews of Geophysics*, **48** (4).

Hobbs, W. and Willis, J. (2012). Midlatitude North Atlantic heat transport: A time series based on satellite and drifter data. *Journal of Geophysical Research: Oceans (1978-2012)*, **117(C1)**.

Hu, Y., Tao, L., and Liu, J. (2013). Poleward expansion of the hadley circulation in CMIP5 simulations. *Advances in Atmospheric Sciences*, **30** (3), 790–795.

Hwang, Y.-T. and Frierson, D. M. (2013). Link between the double-Intertropical Convergence Zone problem and cloud biases over the Southern Ocean. *Proceedings of the National Academy of Sciences*, **110** (13), 4935–4940.

IPCC (2013). *Summary for Policymakers*, book section SPM, (pp. 130). Cambridge University Press: Cambridge, United Kingdom and New York, NY, USA.

Jayne, S. and Marotzke, J. (2001). The dynamics of ocean heat transport variability. *Reviews of Geophysics*, **39(3)**, 385–411.

Johns, W., Baringer, M., Beal, L., Cunningham, S., Kanzow, T., Bryden, H., Hirschi, J., Marotzke, J., Meinen, C., Shaw, B., and Curry, R. (2011). Continuous, Array-Based Estimates of Atlantic Ocean Heat Transport at 26.5°N. *Journal of Climate*, **24(10)**, 2429–2449.

Jungclaus, J. H., Fischer, N., Haak, H., Lohmann, K., Marotzke, J., Matei, D., Mikolajewicz, U., Notz, D., and von Storch, J.-S. (2013). Characteristics of the ocean simulations in MPIOM, the ocean component of the MPI Earth System Model. *Journal of Advances in Modeling Earth Systems*, **5**, 422–446.

Kanzow, T., Cunningham, S., Johns, W., Hirschi, J. J., Marotzke, J., Baringer, M., Meinen, C., Chidichimo, M., Atkinson, C., Beal, L., et al. (2010). Seasonal variability of the Atlantic meridional overturning circulation at 26.5°N. *Journal of Climate*, **23** (21), 5678–5698.

Klinger, B. A. and Marotzke, J. (2000). Meridional heat transport by the subtropical cell. *Journal of physical oceanography*, **30** (4), 696–705.

Knight, J. R., Allan, R. J., Folland, C. K., Vellinga, M., and Mann, M. E. (2005). A signature of persistent natural thermohaline circulation cycles in observed climate. *Geophysical Research Letters*, **32** (20).

Knight, J. R., Folland, C. K., and Scaife, A. A. (2006). Climate impacts of the Atlantic multidecadal oscillation. *Geophysical Research Letters*, **33** (17).

Knutti, R. and Sedláček, J. (2013). Robustness and uncertainties in the new CMIP5 climate model projections. *Nature Climate Change*, **3** (4), 369–373.

Köhl, A. (2005). Anomalies of meridional overturning: Mechanisms in the North Atlantic. *Journal of Physical Oceanography*, **35** (8), 1455–1472.

Kröger, J., Müller, W. A., and von Storch, J.-S. (2012). Impact of different ocean reanalyses on decadal climate prediction. *Climate dynamics*, **39** (3-4), 795–810.

Latif, M., Collins, M., Pohlmann, H., and Keenlyside, N. (2006). A review of predictability studies of Atlantic sector climate on decadal time scales. *Journal of Climate*, **19** (23), 5971–5987.

Latif, M. and Keenlyside, N. S. (2011). A perspective on decadal climate variability and predictability. *Deep Sea Research Part II: Topical Studies in Oceanography*, **58** (17), 1880–1894.

Lavin, A., Bryden, H., and Parrilla, G. (1998). Meridional transport and heat flux variations in the subtropical North Atlantic. *The Global atmosphere and ocean system*, **6(3)**, 269–293.

Lee, T. and Marotzke, J. (1998). Seasonal cycles of meridional overturning and heat transport of the Indian Ocean. *Journal of Physical Oceanography*, **28(5)**, 923–943.

Lorenz, E. (1975). The physical bases of climate and climate modelling. *Climate predictability*, **16**, 132–136.

Lu, J., Chen, G., and Frierson, D. M. (2008). Response of the zonal mean atmospheric circulation to El Niño versus global warming. *Journal of Climate*, **21** (22), 5835–5851.

Lu, J., Sun, L., Wu, Y., and Chen, G. (2014). The Role of Subtropical Irreversible PV Mixing in the Zonal Mean Circulation Response to Global Warming–Like Thermal Forcing. *Journal of Climate*, **27** (6), 2297–2316.

Lumpkin, R. and Speer, K. (2007). Global ocean meridional overturning. *Journal of Physical Oceanography*, **37(10)**, 2550–2562.

Macdonald, A. and Wunsch, C. (1996). An estimate of global ocean circulation and heat fluxes. *Nature*, **382(6590)**, 436–439.

MacLeod, D., Caminade, C., and Morse, A. (2012). Useful decadal climate prediction at regional scales? A look at the ENSEMBLES stream 2 decadal hindcasts. *Environmental Research Letters*, **7** (4), 044012.

Marsland, S., Haak, H., Jungclaus, J., Latif, M., and Röske, F. (2003). The Max-Planck-Institute global ocean/sea ice model with orthogonal curvilinear coordinates. *Ocean modelling*, **5(2)**, 91–127.

Matei, D., Baehr, J., Jungclaus, J. H., Haak, H., Müller, W. A., and Marotzke, J. (2012a). Multiyear prediction of monthly mean Atlantic meridional overturning circulation at 26.5°N. *Science*, **335** (6064), 76–79.

Matei, D., Pohlmann, H., Jungclaus, J., Müller, W., Haak, H., and Marotzke, J. (2012b). Two tales of initializing decadal climate prediction experiments with the ECHAM5/MPI-OM model. *Journal of Climate*, **25** (24), 8502–8523.

Meehl, G. A., Goddard, L., Boer, G., Burgman, R., Branstator, G., Cassou, C., Corti, S., Danabasoglu, G., Doblas-Reyes, F., Hawkins, E., et al. (2014). Decadal climate prediction: an update from the trenches. *Bulletin of the American Meteorological Society*, **95** (2), 243–267.

Meehl, G. A., Goddard, L., Murphy, J., Stouffer, R. J., Boer, G., Danabasoglu, G., Dixon, K., Giorgetta, M. A., Greene, A. M., Hawkins, E., et al. (2009). Decadal prediction: Can it be skillful? *Bulletin of the American Meteorological Society*, **90** (10), 1467–1485.

Meehl, G. A., Washington, W. M., Arblaster, J. M., Hu, A., Teng, H., Tebaldi, C., Sanderson, B. N., Lamarque, J.-F., Conley, A., Strand, W. G., et al. (2012). Climate system response to external forcings and climate change projections in CCSM4. *Journal of Climate*, **25** (11), 3661–3683.

Minobe, S., Kuwano-Yoshida, A., Komori, N., Xie, S.-P., and Small, R. J. (2008). Influence of the Gulf Stream on the troposphere. *Nature*, **452** (7184), 206–209.

Minobe, S., Miyashita, M., Kuwano-Yoshida, A., Tokinaga, H., and Xie, S.-P. (2010). Atmospheric response to the Gulf Stream: seasonal variations*. *Journal of Climate*, **23** (13), 3699–3719.

Msadek, R., Dixon, K., Delworth, T., and Hurlin, W. (2010). Assessing the predictability of the Atlantic meridional overturning circulation and associated fingerprints. *Geophysical Research Letters*, **37** (19).

Msadek, R. and Frankignoul, C. (2009). Atlantic multidecadal oceanic variability and its influence on the atmosphere in a climate model. *Climate dynamics*, **33** (1), 45–62.

Msadek, R., Johns, W., Yeager, S., Danabasoglu, G., Delworth, T., and A.Rosati (2013). The Atlantic Meridional Heat Transport at 26.5°N and Its Relationship with the MOC in the RAPID Array and the GFDL and NCAR Coupled Models. *Journal of Climate*, **26(12)**, 4335–4356.

Muir, L. and Fedorov, A. (2014). How the AMOC affects ocean temperatures on decadal to centennial timescales: the North Atlantic versus an interhemispheric seesaw. *Climate Dynamics*, **45** (1-2), 151–160.

Müller, W. A., Baehr, J., Haak, H., Jungclaus, J. H., Kröger, J., Matei, D., Notz, D., Pohlmann, H., Storch, J., and Marotzke, J. (2012). Forecast skill of multi-year seasonal means in the decadal prediction system of the Max Planck Institute for Meteorology. *Geophysical Research Letters*, **39** (22).

Munoz, E., Kirtman, B., and Weijer, W. (2011). Varied representation of the Atlantic meridional overturning across multidecadal ocean reanalyses. *Deep Sea Research Part II: Topical Studies in Oceanography*, **58(17)**, 1848–1857.

Murphy, A. H. (1973). A new vector partition of the probability score. *Journal of Applied Meteorology*, **12** (4), 595–600.

Nurser, A. G. and Lee, M.-M. (2004). Isopycnal averaging at constant height. Part I: The formulation and a case study. *Journal of physical oceanography*, **34** (12), 2721–2739.

Palmer, T., Doblas-Reyes, F., Weisheimer, A., and Rodwell, M. (2008). Toward seamless prediction: Calibration of climate change projections using seasonal forecasts. *Bulletin of the American Meteorological Society*, **89** (4), 459–470.

Palmer, T. N. (2000). Predicting uncertainty in forecasts of weather and climate. *Reports on Progress in Physics*, **63** (2), 71.

Pohlmann, H., Botzet, M., Latif, M., Roesch, A., Wild, M., and Tschuck, P. (2004). Estimating the decadal predictability of a coupled AOGCM. *Journal of Climate*, **17** (22), 4463–4472.

Pohlmann, H., Jungclaus, J., Marotzke, J., Köhl, A., and Stammer, D. (2009). Improving predictability through the initialization of a coupled climate model with global oceanic reanalysis. *J. Climate*, **22**, 3926–3938.

Pohlmann, H., Müller, W. A., Kulkarni, K., Kameswarrao, M., Matei, D., Vamborg, F., Kadow, C., Illing, S., and Marotzke, J. (2013a). Improved forecast skill in the tropics in the new MiKlip decadal climate predictions. *Geophysical Research Letters*, **40** (21), 5798–5802.

Pohlmann, H., Sienz, F., and Latif, M. (2006). Influence of the multidecadal Atlantic meridional overturning circulation variability on European climate. *Journal of climate*, **19** (23), 6062–6067.

Pohlmann, H., Smith, D. M., Balmaseda, M. A., Keenlyside, N. S., Masina, S., Matei, D., Müller, W. A., and Rogel, P. (2013b). Predictability of the mid-latitude Atlantic meridional overturning circulation in a multi-model system. *Climate dynamics*, **41** (3-4), 775–785.

Rahmstorf, S., Feulner, G., Mann, M. E., Robinson, A., Rutherford, S., and Schaffernicht, E. J. (2015). Exceptional twentieth-century slowdown in Atlantic Ocean overturning circulation. *Nature Climate Change*, .

Rhines, P., Häkkinen, S., and Josey, S. A. (2008). Is oceanic heat transport significant in the climate system? In *Arctic–subarctic ocean fluxes* (pp. 87–109). Springer.

Riser, S. C. and Lozier, M. S. (2013). Rethinking the Gulf Stream. *Scientific American*, **308** (2), 50–55.

Robson, J., Sutton, R., and Smith, D. (2012). Initialized decadal predictions of the rapid warming of the North Atlantic Ocean in the mid 1990s. *Geophysical Research Letters*, **39** (19).

Rodwell, M., Drevillon, M., Frankignoul, C., Hurrell, J., Pohlmann, H., Stendel, M., and Sutton, R. (2004). North Atlantic forcing of climate and its uncertainty from a multi-model experiment. *Quarterly Journal of the Royal Meteorological Society*, **130** (601), 2013–2032.

Rodwell, M. and Folland, C. (2002). Atlantic air–sea interaction and seasonal predictability. *Quarterly Journal of the Royal Meteorological Society*, **128** (583), 1413–1443.

Rose, B. E. and Ferreira, D. (2012). Ocean heat transport and water vapor greenhouse in a warm equable climate: A new look at the low gradient paradox. *Journal of Climate*, **26** (6), 2117–2136.

Sarmiento, J. (1986). On the North and Tropical Atlantic heat balance. *Journal of Geophysical Research: Oceans (1978-2012)*, **91(C10)**, 11677–11689.

Seager, R., Battisti, D. S., Yin, J., Gordon, N., Naik, N., Clement, A. C., and Cane, M. A. (2002). Is the Gulf Stream responsible for Europe's mild winters? *Quarterly Journal of the Royal Meteorological Society*, **128** (586), 2563–2586.

Seidel, D. J., Fu, Q., Randel, W. J., and Reichler, T. J. (2008). Widening of the tropical belt in a changing climate. *Nature geoscience*, **1** (1), 21–24.

Siedler, G., Griffies, S. M., Gould, J., and Church, J. A. (2013). *Ocean Circulation and Climate: A 21st century perspective*. volume 103. Academic Press.

Smeed, D., McCarthy, G., Rayner, D., Moat, B., Johns, W., Baringer, M., and Meinen, C. (2015). Atlantic meridional overturning circulation observed by the RAPID-MOCHA-WBTS (RAPID-Meridional Overturning Circulation and Heatflux Array-Western Boundary Time Series) array at 26°N from 2004 to 2014. *British Oceanographic Data Centre - Natural Environment Research Council, UK.*, .

Smeed, D., Wood, R., Cunningham, S., McCarthy, G., Kuhlbrodt, T., and Dye, S. R. (2013). Impacts of climate change on the Atlantic Heat Conveyor. *MCCIP Science Review 2013*, , 49–59.

Sonnewald, M., Hirschi, J.-M., and Marsh, R. (2013). Oceanic dominance of interannual subtropical North Atlantic heat content variability. *Ocean Science Discussions*, **10**, 27–53.

Srokosz, M., Baringer, M., Bryden, H., Cunningham, S., Delworth, T., Lozier, S., Marotzke, J., and Sutton, R. (2012). Past, present, and future changes in the Atlantic meridional overturning circulation. *Bulletin of the American Meteorological Society*, **93** (11), 1663–1676.

Stevens, B., Giorgetta, M., Esch, M., Mauritsen, T., Crueger, T., Rast, S., Salzmann, M., Schmidt, H., Bader, J., Block, K., Brokopf, R., Fast, I., Kinne, S., Kornblueh, L., Lohmann, U., Pincus, R., Reichler, T., and Roeckner, E. (2013). Atmospheric component of the MPI-M Earth System Model: ECHAM6. *Journal of Advances in Modeling Earth Systems*, **5**, 146–172.

Sutton, R. T. and Dong, B. (2012). Atlantic Ocean influence on a shift in European climate in the 1990s. *Nature Geoscience*, **5** (11), 788–792.

Sutton, R. T. and Hodson, D. L. (2005). Atlantic Ocean forcing of North American and European summer climate. *Science*, **309** (5731), 115–118.

Talley, L. D. (2003). Shallow, intermediate, and deep overturning components of the global heat budget. *Journal of Physical Oceanography*, **33** (3), 530–560.

Taylor, K., Stouffer, R., and Meehl, G. (2012). An Overview of CMIP5 and the Experiment Design. *Bulletin of the American Meteorological Society*, **93(4)**, 485–498.

Tiedje, B. and Baehr, J. (2014). Limitations of the potential predictability of meridional mass and heat transports in the North Atlantic. *Geophysical Research Letters*, **41** (12), 4270–4276.

Tiedje, B., Köhl, A., and Baehr, J. (2012). Potential predictability of the North Atlantic heat transport based on an oceanic state estimate. *Journal of Climate*, **25** (24), 8475–8486.

Tietsche, S., Notz, D., Jungclaus, J. H., and Marotzke, J. (2013). Predictability of large interannual Arctic sea-ice anomalies. *Climate dynamics*, **41** (9-10), 2511–2526.

Toggweiler, J. (2009). Shifting westerlies. *Science*, **323** (5920), 1434–1435.

Toth, Z. and Kalnay, E. (1993). Ensemble forecasting at NMC: The generation of perturbations. *Bulletin of the American Meteorological Society*, **74** (12), 2317–2330.

Toth, Z. and Kalnay, E. (1997). Ensemble forecasting at NCEP and the breeding method. *Monthly Weather Review*, **125** (12), 3297–3319.

Vallis, G. K. and Farneti, R. (2009). Meridional energy transport in the coupled atmosphere-ocean system: scaling and numerical experiments. *Quarterly Journal of the Royal Meteorological Society*, **135** (644), 1643–1660.

van Oldenborgh, G. J., Doblas-Reyes, F. J., Wouters, B., and Hazeleger, W. (2012). Decadal prediction skill in a multi-model ensemble. *Climate dynamics*, **38** (7-8), 1263–1280.

van Vuuren, D., Edmonds, J., Kainuma, M., Riahi, K., Thomson, A., Hibbard, K., Hurtt, G., Kram, T., Krey, V., Lamarque, J.-F., Masui, T., Meinshausen, M., Nakicenovic, N., Smith, S., and Rose, S. (2011). The representative concentration pathways: an overview. *Climate Change*, **109**, 5–31.

Vecchi, G. A., Msadek, R., Delworth, T. L., Dixon, K. W., Guilyardi, E., Hawkins, E., Karspeck, A. R., Mignot, J., Robson, J., Rosati, A., et al. (2012). Comment on Multiyear prediction of monthly mean Atlantic Meridional Overturning Circulation at 26.5○N. *Science*, **338** (6107), 604–604.

Vellinga, M. and Wood, R. (2002). Global climatic impacts of a collapse of the Atlantic thermohaline circulation. *Climate Change*, **54(3)**, 251–267.

Villarini, G. and Vecchi, G. A. (2012). Twenty-first-century projections of North Atlantic tropical storms from CMIP5 models. *Nature Climate Change*, **2** (8), 604–607.

von Storch, J.-S. and Haak, H. (2008). Impact of daily fluctuations on long-term predictability of the Atlantic meridional overturning circulation. *Geophysical Research Letters*, **35** (1).

Weaver, A. J., Sedlacek, J., Eby, M., Alexander, K., Crespin, E., Fichefet, T., Philippon-Berthier, G., Joos, F., Kawamiya, M., Matsumoto, K., Steinacher, M., Tachiiri, K., Tokos, K., Yoshimori, M., and Zickfeld, K. (2012). Stability of the Atlantic meridional overturning circulation: A model intercomparison. *Geophysical Research Letters*, **39(20)**.

Weisheimer, A. and Palmer, T. (2014). On the reliability of seasonal climate forecasts. *Journal of The Royal Society Interface*, **11** (96), 20131162.

Wilks, D. S. (2011). *Statistical methods in the atmospheric sciences*. volume 100. Academic press.

Willis, J. (2010). Can in situ floats and satellite altimeters detect long-term changes in Atlantic Ocean overturning? *Geophysical Research Letters*, **37, L06602, doi:10.1029/2010GL042372**.

Yeager, S., Karspeck, A., Danabasoglu, G., Tribbia, J., and Teng, H. (2012). A decadal prediction case study: Late twentieth-century North Atlantic Ocean heat content. *Journal of Climate*, **25** (15), 5173–5189.

Zhang, L. and Wang, C. (2013). Multidecadal North Atlantic sea surface temperature and Atlantic meridional overturning circulation variability in CMIP5 historical simulations. *Journal of Geophysical Research: Oceans*, **118** (10), 5772–5791.

Zhang, R. and Delworth, T. L. (2006). Impact of Atlantic multidecadal oscillations on India/Sahel rainfall and Atlantic hurricanes. *Geophysical Research Letters*, **33** (17).

Acknowledgements

I am thankful to many people who have supported, encouraged, helped me during my PhD.

First of all, lots of thanks to my supervisor Johanna Baehr. Not only for your guidance, advice and invaluable feedback during the last 3 years, but also for your support in guiding my as young student through the university jungle. I could not have imagined having a better advisor and mentor during the last years.

Thanks also to Wolfgang Müller being my co-advisor and the evaluation of the thesis, to Hermann Held for chairing my advisory panel, and off course to the entire team of the SICSS graduate school.

I am also grateful to the BMBF project "RACE" for the financial support of my PhD project.

Thanks also to all my working group colleagues, both permanent and temporary. I thank Sebastian Brune, André Düsterhus, and Leonard Borchert for proofreading parts of this thesis.

I would like to thank Kameswarrao Modali for his help and advice concerning the MPI-ESM model simulations and CMORization.

Thanks to many people and fellow PhD students of the SICSS who made the 3 years of my PhD to more than just work.

Thanks also to my summer intern, Megan Baker, for her help with the analysis of the first model results and for letting me slip into the role of a supervisor.

Last but not least, lots of thanks to my family and my friends for all their support, and to my wife Carina your support outside of the office and making my life complete.

Eidesstattliche Versicherung

Hiermit erkläre ich an Eides statt, dass ich die vorliegende Dissertationsschrift selbst verfasst und keine anderen als die angegebenen Quellen und Hilfsmittel benutzt habe.

Hamburg, den 02.11.2015

Matthias Fischer